UNIVERSITY OF CALIFORNIA

Los Angeles

Design of Highly Dynamic Robot Platforms

A dissertation submitted in partial satisfaction
of the requirements for the degree
Doctor of Philosophy in Mechanical & Aerospace Engineering

by

Yeting Liu

2024

ABSTRACT OF THE DISSERTATION

Design of Highly Dynamic Robot Platforms

by

Yeting Liu
Doctor of Philosophy in Mechanical & Aerospace Engineering
University of California, Los Angeles, 2024
Professor Dennis W. Hong, Chair

The vision of seamlessly integrating robots into daily life, where they assist people across diverse tasks, has driven research in humanoid robotics. For robots to function effectively in human-centered environments, a humanoid form with highly dynamic capabilities—such as running, jumping, and adapting to unpredictable situations—is essential. However, replicating human-like agility and versatility remains challenging due to current limitations in actuation, sensing, and control. To meet these demands, dedicated research platforms for dynamic lower-body locomotion and versatile robotic manipulation are crucial. By making these platforms accessible and reliable, we can accelerate innovation in dynamic robotics, enabling researchers to explore advancements that will eventually bring humanoid robots into real-world, daily applications.

This dissertation aims to address the problem by presenting two highly dynamic robotic platforms: **BRUCE** – Bipedal Robot Unit with Compliance Enhanced, and **YORI** – Yummy Operations Robot IniDtiative.

BRUCE is a proprioceptive actuated miniature bipedal robot designed for dynamic motion capabilities and robust interaction with unstructured environments. With 5 degrees of freedom (DoF) per leg, including a spherical hip joint, knee, and ankle, BRUCE achieves a human-like range of lower body motion. Its design in-

corporates a novel cable-driven differential pulley system and a linkage mechanism to minimize leg inertia, enhancing stability and control. Tests of dynamic bipedal locomotion and jumping demonstrate BRUCE's high dynamic performance.

In parallel, YORI represents a major breakthrough in culinary automation as an autonomous robotic cooking system. Featuring a dual-arm manipulator equipped with proprioceptive actuators, YORI performs a wide variety of cooking tasks with speed, precision, and force control. Its modular kitchen design allows for seamless integration of custom tools and appliances, enhancing adaptability for diverse culinary activities.

Together, BRUCE and YORI showcase the potential of robotic platforms in dynamic and adaptive tasks, from the physical robustness and stability of BRUCE to YORI's efficiency and versatility in food preparation. Guidelines for Highly Dynamic Robot Platforms Design is provided in the end. By adhering to these guidelines, future robotic platforms can achieve high dynamic performance, ensuring versatility, scalability, and reliability across a broad spectrum of applications.

The dissertation of Yeting Liu is approved.

Xiaochun Li

Veronica Santos

Jonathan Hopkins

Dennis W. Hong, Committee Chair

University of California, Los Angeles

2024

TABLE OF CONTENT

LIST OF SYMBOLS

Greek symbols

Symbols	definition
θ	Robot joint angle
q	Robot actuator angle
τ	Robot joint torque
κ	Robot actuator torque
l	Robot link length
m	Robot link mass

LIST OF FIGURES

LIST OF TABLES

ACKNOWLEDGMENTS

First of all, I would like to present my deepest gratitude to my advisor, Dr. Dennis Hong, for his invaluable guidance and unconditional support throughout my Ph.D. research journey. Dr. Hong's insights, expertise, enthusiasm, and optimism in both academics and daily life have been instrumental in helping me grow both as a researcher and as an individual. I am sincerely thankful for the unlimited freedom he gave me to explore new ideas, and for his constant motivation during challenging times.

I would also like to extend my heartfelt thanks to my committee members, Prof. Xiaochun Li, Prof. Veronica Santos, and Prof. Jonathan Hopkins, for their clear and straightforward instructions during the class, and the constructive guidance they provided during the oral qualifying examination. I am deeply grateful for the time and effort you devoted to reviewing my work, as well as for your valuable insights that helped me improve and refine my research.

Furthermore, my research work would not have been successful without generous help from all other RoMeLa members. Especially team **BRUCE**: Junjie Shen, Jingwen Zhang and Xiaoguang Zhang. Also team **YORI**: Donghun Noh, Hyunwoo Nam, Kyle Gillespie and Fadi Rafidi. As well as team **LIMMS** and **Robocup**: Gabriel Fernandez, Colin Togashi, Justin Quan, Aditya Navghare, Mingzhang Zhu, Quanyou Wang, Ruochen Hou, Yicheng Wang, Shiqi Wang, Arturo Flores Alvarez and Alvin Zhu. Working alongside such talented and passionate individuals has been an incredible experience. Of course I will not forget the all-nighters we powered through together.

Finally, to my family and friends, especially my significant other, Alice Gao – thank you for being by my side every step of the way. Your patience, understanding, and unwavering love have been my greatest source of strength.

This work is as much yours as it is mine. Thank you all.

VITA

2013–2017	B.S. in Mechanical Engineering, University of California, Los Angeles (UCLA), United States
2017–2019	M.S. in Mechanical Engineering, University of California, Los Angeles (UCLA), United States
2019–Present	Ph.D. Candidate in Mechanical Engineering, University of California, Los Angeles (UCLA), United States

PUBLICATIONS

Zhang, J., Shen, J., **Liu, Y.** and Hong, D., 2023, October. Design of a jumping control framework with heuristic landing for bipedal robots. In *2023 IEEE/RSJ International Conference on Intelligent Robots and Systems (IROS)* (pp. 8502-8509). IEEE.

Liu, Y., Shen, J., Zhang, J., Zhang, X., Zhu, T. and Hong, D., 2022, May. Design and control of a miniature bipedal robot with proprioceptive actuation for dynamic behaviors. In *2022 International Conference on Robotics and Automation (ICRA)* (pp. 8547-8553). IEEE.

Zhu, T., Fernandez, G.I., Togashi, C., **Liu, Y.** and Hong, D., 2022, July. Feasibility study of limms, a multi-agent modular robotic delivery system with various locomotion and manipulation modes. In *2022 19th International Conference on Ubiquitous Robots (UR)* (pp. 30-37). IEEE.

Lin, X., Fernandez, G.I., **Liu, Y.**, Zhu, T., Shirai, Y. and Hong, D., 2022, October. Multi-modal multi-agent optimization for limms, a modular robotics approach to delivery automation. In *2022 IEEE/RSJ International Conference on Intelligent Robots and Systems (IROS)* (pp. 12674-12681). IEEE.

Shen, J., Zhang, J., **Liu, Y.** and Hong, D., 2022, November. Implementation of a robust dynamic walking controller on a miniature bipedal robot with proprioceptive actuation. In *2022 IEEE-RAS 21st International Conference on Humanoid Robots (Humanoids)* (pp. 39-46). IEEE.

Shen, J., **Liu, Y.**, Zhang, X. and Hong, D., 2020, June. Optimized jumping of an articulated robotic leg. In *2020 17th International Conference on Ubiquitous Robots (UR)* (pp. 205-212). IEEE.

Noh, D., **Liu, Y.**, Rafeedi, F., Nam, H., Gillespie, K., Yi, J.S., Zhu, T., Xu, Q. and Hong, D., 2020, June. Minimal degree of freedom dual-arm manipulation platform with coupling body joint for diverse cooking tasks. In *2020 17th International Conference on Ubiquitous Robots (UR)* (pp. 225-232). IEEE.

CHAPTER 1

Introduction

1.1 Motivation

The aspiration to seamlessly integrate robots into everyday life and enable them to assist human beings with a wide range of functions has been a long-standing goal in the field of robotics. For robots to achieve such a role, numerous studies have demonstrated that a humanoid form is ideal [10–12]. A human-like configuration enables robots to operate in human-centric environments and interact naturally with the world around them. To be effective and useful in daily life, humanoid robots must be capable of highly dynamic behaviors—such as running, jumping, and quickly adapting to unpredictable situations, while maintaining stability and precision [9, 13]. Achieving these capabilities requires significant advancements in robot design and control.

Despite notable progress, current humanoid robot technology remains limited, with substantial challenges in replicating human-like agility and adaptability. The majority of humanoid robots are constrained by heavy-weight designs, slow movements, and limited adaptability, primarily due to the reliance on the traditional locomotion control strategies and high gear ratio actuators, which restrict dynamic performance and impact mitigation [14–16]. Designing robots capable of dynamic and versatile movements is a complex task, with many obstacles such as actuation, sensing, and control. Research on humanoid robots is still in its early stages in terms of achieving the required level of robustness, dynamic abilities, and reliability for widespread, real-world applications. Thus, there is an immense amount of research needed to make highly dynamic humanoid robots a practical

reality in daily environments.

To address these challenges, the development of highly dynamic humanoid robots can be divided into two main areas of focus: lower-body locomotion and robotic manipulation. Firstly, a dedicated platform for highly dynamic lower-body locomotion is essential to explore and optimize legged movement, stability, and impact mitigation. At the same time, an adaptable and precise robotic manipulator platform is needed to perform various tasks that require dexterity, speed, and force control. For these platforms to facilitate research effectively, they must be affordable, accessible, and reliable, allowing researchers from diverse backgrounds to experiment and innovate without expensive costs or technical limitations.

In conclusion, to accelerate the progress of robots assisting human beings in our environment, the field urgently needs affordable and dependable robotic platforms designed for high dynamic performance. Making these platforms accessible will create more opportunities in research, foster innovation, and bring us closer to the vision of robots as an integral part of everyday life.

1.2 Background

1.2.1 Actuation

Actuators are the core components driving robotic motion, directly impacting a robot's responsiveness, force control, and adaptability to different tasks. Traditional high-gear-ratio actuators, series elastic actuators (SEAs), and proprioceptive actuators each offer unique strengths and limitations, influencing the design and functionality of robots across applications—from industrial automation to highly dynamic humanoid robotics.

Traditional High-Gear-Ratio Actuators

Traditional high-gear-ratio actuators, such as harmonic drives and cycloidal drives

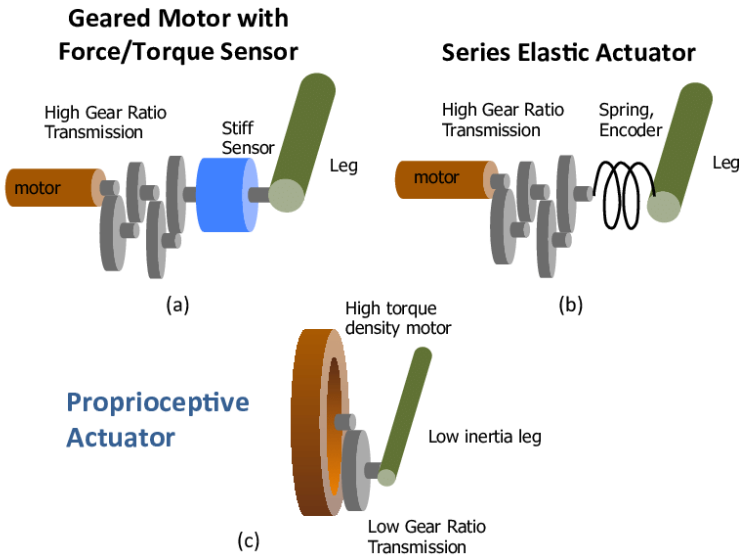

Figure 1.1: Three different electromagnetic actuator concepts. (a) High-gear-ratio actuator with torque sensor, (b) Series elastic actuator, (c) Proprioceptive actuator. [1]

actuators, are commonly used in robotics for applications requiring high torque and precise positioning [17]. These actuators achieve high torque outputs through high reduction ratios, allowing a relatively small motor to produce significant output force. Harmonic drives achieve this by using a flexible gear and elliptical wave generator, resulting in a highly efficient and backlash-free transmission. In parallel, cycloidal drives use rolling elements and a cam mechanism to achieve similar results, providing smooth and precise motion control with minimal backlash [17].

The primary advantage of these actuators is their ability to deliver high torque density and precise position control, making them ideal for tasks requiring stable and rigid positioning, such as in industrial robots or cobots. However, their high reduction ratios also lead to issues like low torque transparency and limited control bandwidth, which makes them hard to back drive, and less suitable for applications requiring dynamic movements or impact mitigation. Additionally, their rigid transmission design makes them less capable of handling unexpected forces, limiting their effectiveness in tasks that require compliance or adaptability.

Series Elastic Actuator (SEA)

A Series Elastic Actuator (SEA) is a type of actuator that incorporates an elastic element, typically a spring, between the motor and the output load [18]. This design allows the actuator to mitigate impacts and reduce reflected inertia, making it ideal for applications that require compliance, such as robots interacting with unpredictable environments or performing dynamic and high-impact movements. SEAs offer stable force control, as the elastic element can store and release energy, smoothing out force delivery and making it easier to regulate output forces [18]. This compliance also enhances safety when operating near humans, as the actuator can yield to unexpected forces instead of resisting them rigidly. As a trade-off, the added elasticity can reduce force bandwidth, meaning the actuator may not respond as quickly to control inputs compared to other rigid actuators. Additionally, SEAs can be less effective in applications that demand high precision or fast responses, as the spring's inherent flexibility can introduce delays and slightly diminish accuracy.

(a) Cycloidal Drive[19] (b) Harmonic Drive[20] (c) SEA[21]

Figure 1.2: Traditional high-gear-ratio actuators and serial elastic actuators

Proprioceptive Actuator (QDD)

Proprioceptive actuators typically consist of a high-torque brushless DC motor paired with a gearbox featuring a reduction ratio of less than 10:1, providing sufficient output torque while maintaining high torque transparency [1, 22]. These features enable proprioceptive actuators to do simple and precise force and torque

control by directly sensing the current, making proprioceptive actuators ideal for applications that require dynamic responsiveness and compliance, such as in legged robots or robotic manipulators performing dynamic tasks.

One of the key advantages of proprioceptive actuators is their high bandwidth, allowing them to respond swiftly to external forces and adjust their behavior accordingly [23]. Moreover, the back-drivability due to the low gear ratio improves impact mitigation and makes them well-suited for tasks involving high-speed and dynamic interactions. On the other hand, while they offer excellent force control and back-drivability, they may have lower torque density compared to traditional high-gear-ratio actuators, which can limit their effectiveness in heavy-duty applications and higher potential for overheating problems [22]. Despite these challenges, proprioceptive actuators are increasingly valued in robotics for their perks of force/torque control, back-drivability, and compliance in unstructured environments.

Table 1.1: Comparison of Different Types of Actuators [9]

	High Reduction + F/T Sensor	**SEA Low Stiffness**	**SEA High Stiffness**	**Proprioceptive Actuator**
Torque density	+++	++	++	+
Impact mitigation	-	+++	++	+++
Bandwidth	++	+	++	+++
Torque control	+++	+++	+++	++

1.2.2 Humanoid Robot

Ever since the development of the first humanoid robot, Honda's P series [24], the field of humanoid robotics has advanced significantly in areas such as joint design, sensor integration, computer vision, and control algorithms. Despite these

advancements, achieving highly dynamic behaviors like running and jumping remains a challenge for humanoid robots. One of the primary limiting factors is the usage of traditional high-gear-ratio actuators, which prioritize torque amplification and precision while compromising speed, agility, and the ability to manage contact impacts [1]. Consequently, most current humanoid robots are optimized for tasks in controlled, predictable environments where they can execute repetitive motions without encountering unexpected disturbances.

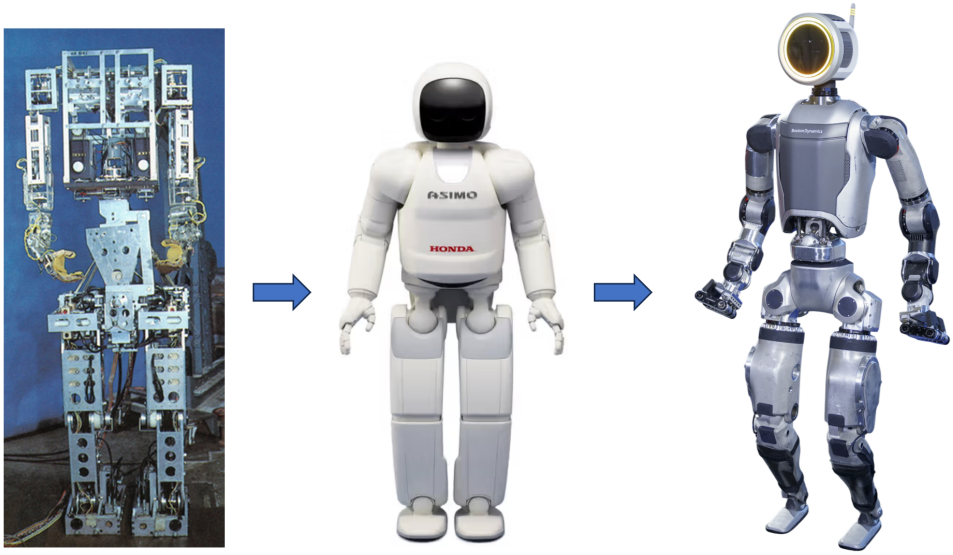

(a) WABOT, 1973 (b) Asimo, 2000 (c) Electric Atlas, 2024

Figure 1.3: The evolution of humanoid robots from 1973 to 2024

A common approach in these robots for maintaining balance and stability during movement is the Zero Moment Point (ZMP) control method. While effective, ZMP-based locomotion typically leads to constrained and cautious steps, with a gait that can appear unnatural [25]. This approach allows robots to handle basic lower-body locomotion but restricts them from performing highly dynamic actions like running or jumping. Therefore, these robots lack the adaptability required for unstructured, human-centered environments.

Emerging technologies like series elastic actuators (SEA) and proprioceptive actuators have shown promise in addressing these limitations. SEAs offer im-

proved impact mitigation, but they still suffer from the low force control bandwidth [26,27]. Proprioceptive actuators, on the other hand, enable impact mitigation and high-bandwidth force control due to their excellent torque transparency [1]. With proprioceptive actuators, highly dynamic motions became feasible for systems such as quadruped robots [28, 29]. However, translating this success to humanoid robots has been slower, constrained by the complexity of control algorithms and the limited accessibility of advanced hardware.

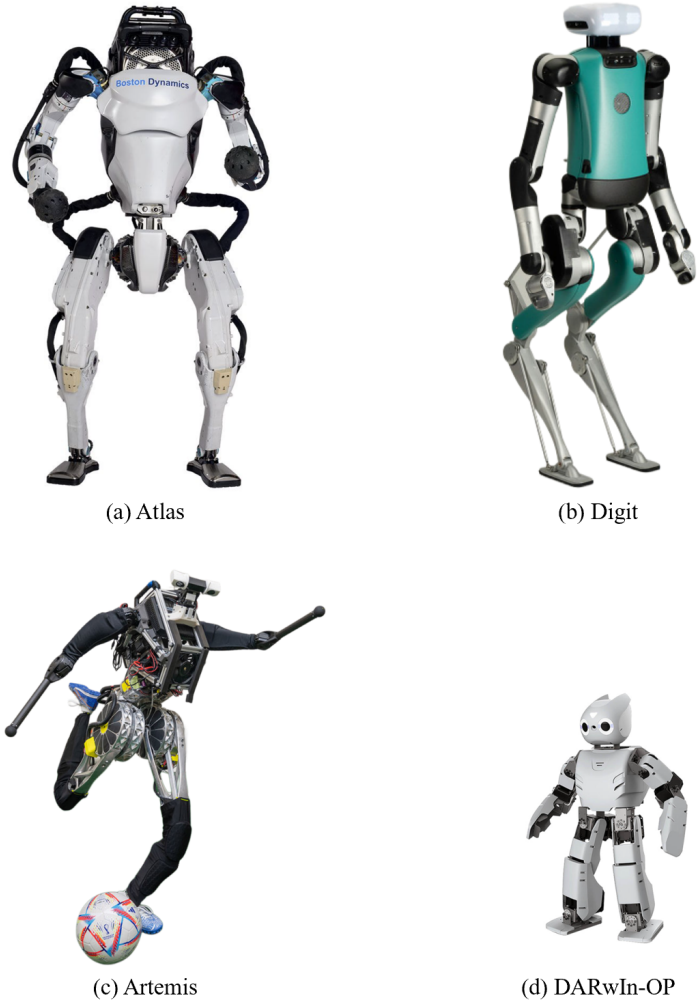

(a) Atlas (b) Digit

(c) Artemis (d) DARwIn-OP

Figure 1.4: Humanoid robot platforms with different actuation solutions and sizes

Atlas from Boston Dynamics [30] has demonstrated itself as the most dynamic full-size humanoid robot, featuring advanced control algorithms and state-of-the-

art hardware. The latest fully electric version of Atlas shows significant improvements in joint range of motion and holds great potential for assisting humans in a variety of tasks. However, its accessibility is highly restricted to Boston Dynamics, leaving external researchers without access to the Atlas platform. Digit from Agility Robotics [31] is also a great humanoid robot platform that addresses the mobility limitations of conventional humanoids. However, the company focuses exclusively on large-scale industrial applications and does not offer individual units of Digit for sale.

ARTEMIS from RoMeLa at UCLA [9] is one of the most advanced proprioceptive actuated full-size humanoid robots. While it features state-of-the-art hardware and demonstrates exceptional capabilities for performing highly dynamic behaviors, its powerful joints pose safety risks for researchers handling the robot without protection. Additionally, the repair and maintenance of such a highly integrated platform can be complex and costly.

For research purposes, small-sized humanoid robots offer a more accessible and practical alternative. DARwIn-OP [32], also developed by RoMeLa, has been a reliable open-platform humanoid robot due to its high performance and affordable price. Despite utilizing traditional servo motors for actuation, DARwIn-OP achieves good dynamic performance compared to full-size humanoid robots, largely due to its smaller size and reduced moment of inertia.

As the field advances, the vision for next-generation humanoid robots emphasizes agility, adaptability, and human-like dynamic behavior. Future robots must achieve seamless integration into human societies and be able to handle dynamic motions in unstructured environments. To realize this vision, innovations in hardware, including low-gear-ratio and proprioceptive actuators, must be paired with advanced control strategies to realize adaptive and resilient motions. These developments are essential for enabling humanoid robots to serve as versatile and natural partners in everyday life.

1.2.3 Manipulator Platform

In recent years, robotic manipulator platforms have seen remarkable advancements, including the ability to safely and efficiently move heavy payloads and the development of highly precise and dexterous end-effectors. These robotic manipulators are widely used in industrial settings, where their high accuracy is critical for tasks such as assembly, welding, and handling delicate components. With robust construction and high-precision control systems, these industrial robotic manipulators are highly effective in well-structured environments where predictable and repetitive tasks are the main focus [33].

The development of collaborative robots (cobots) has brought a significant influence to the field, aiming to enable safe human-robot interaction in shared spaces. Cobots are typically equipped with state-of-art force/torque sensors, vision systems, and proximity detectors to allow them to navigate paths, detect obstacles, and respond to human inputs in real time [34]. This sensor-driven approach has expanded its applications to healthcare, retail, and personal assistance. However, the reliance on external sensors usually results in high costs and more computational demands, limiting their accessibility to individual researchers and smaller-scale applications.

(a) UR Cobot [35] (b) Ambidex (c) Prpject Blue

Figure 1.5: Robotic manipulator platforms with different actuation solutions and purposes

To address these challenges, researchers are focusing on lighter manipulator

arm designs with low inertia but high stiffness and strength, combining proprioceptive-actuated joints with low-gear-ratio actuators to achieve compliance and torque transparency. For example, LIMS2-AMBIDEX [**?**] is a low-inertia and high-stiffness manipulator platform developed at KoreaTech. It utilizes tendon-driven systems to smartly relocate most of the actuators closer to the torso, minimizing distal mass to enable high dynamic motions. However, the tendon-driven system requires frequent maintenance, and its high cost makes it inaccessible for many academic researchers.

On the other hand, Project Blue [36] developed at UC Berkeley proposed a quasi-direct drive robotic manipulator platform with low cost to fulfill the need for accessible manipulators in academia. While it features fast speeds and a lightweight design, its performance is constrained by insufficient joint stiffness due to the belt transmission, particularly when handling heavy payloads.

Future robotic manipulator platforms must prioritize robust designs with high stiffness and low inertia, and proprioceptive actuation for dynamic motions. Moreover, affordability and ease of maintenance are essential to ensure accessibility for research and smaller-scale use. These advancements will enable robotic manipulators to transition from industrial tools to versatile, human-centric solutions in diverse environments.

1.3 Research Objectives

To streamline the complexity of this research, the development of highly dynamic humanoid robots can be divided into two main areas of focus: lower-body locomotion and robotic manipulation.

For the lower-body locomotion platform, the objective is to develop a low-cost miniature humanoid robot capable of dynamic locomotion such as walking and jumping. Achieving this requires a proprioceptive actuated lower body to ensure high torque transparency and effective impact mitigation. Additionally, minimizing the leg's inertia is crucial, which can be accomplished by employing innovative mechanisms to relocate actuators and reduce distal mass. The structural components must also be optimized for a high strength-to-weight ratio, ensuring the robot is both lightweight and strong enough to handle the demands of dynamic bipedal locomotion.

Similarly, the same principles guide the design of the robotic manipulator platform. The goal is to develop a dual-arm manipulator with a minimal degree of freedom to lower costs and system mass, enabling highly dynamic movements. Proprioceptive actuators will drive the manipulator platform, combining with intelligent mechanisms to reduce inertia and maximize the workspace efficiently.

By the end of this research, experimental data should validate the high dynamic performance of the proposed robotic platforms. The design choices and innovations introduced in these robotic platforms are intended to be transferable to other humanoid and manipulator systems to promote dynamic robotic motions. Moreover, the insights gained from designing these platforms will provide a solid foundation for understanding and developing highly dynamic and proprioceptively actuated robotic systems.

1.4 Organization

Chapter 2 introduces BRUCE, a next-generation miniature humanoid robot platform designed for research on high-dynamic behaviors. This chapter details the design process of BRUCE and presents testing results, including dynamic bipedal locomotion and jumping.

Chapter 3 builds on Chapter 2, focusing on a revised version of BRUCE. This chapter covers hardware updates aimed at enhancing BRUCE's stability and energy efficiency, along with efforts to transition BRUCE into an open-source platform.

Chapter 4 discusses YORI, the proprioceptively actuated dual-arm manipulator platform used in an autonomous cooking system. This chapter outlines YORI's design decisions and provides insights into designing highly dynamic robotic platforms, synthesizing lessons learned from the development of BRUCE and YORI.

Finally, Chapter 5 concludes the dissertation, summarizing key findings and outlining directions for future research.

CHAPTER 2

BRUCE – Bipedal Robot Unit with Compliance Enhanced

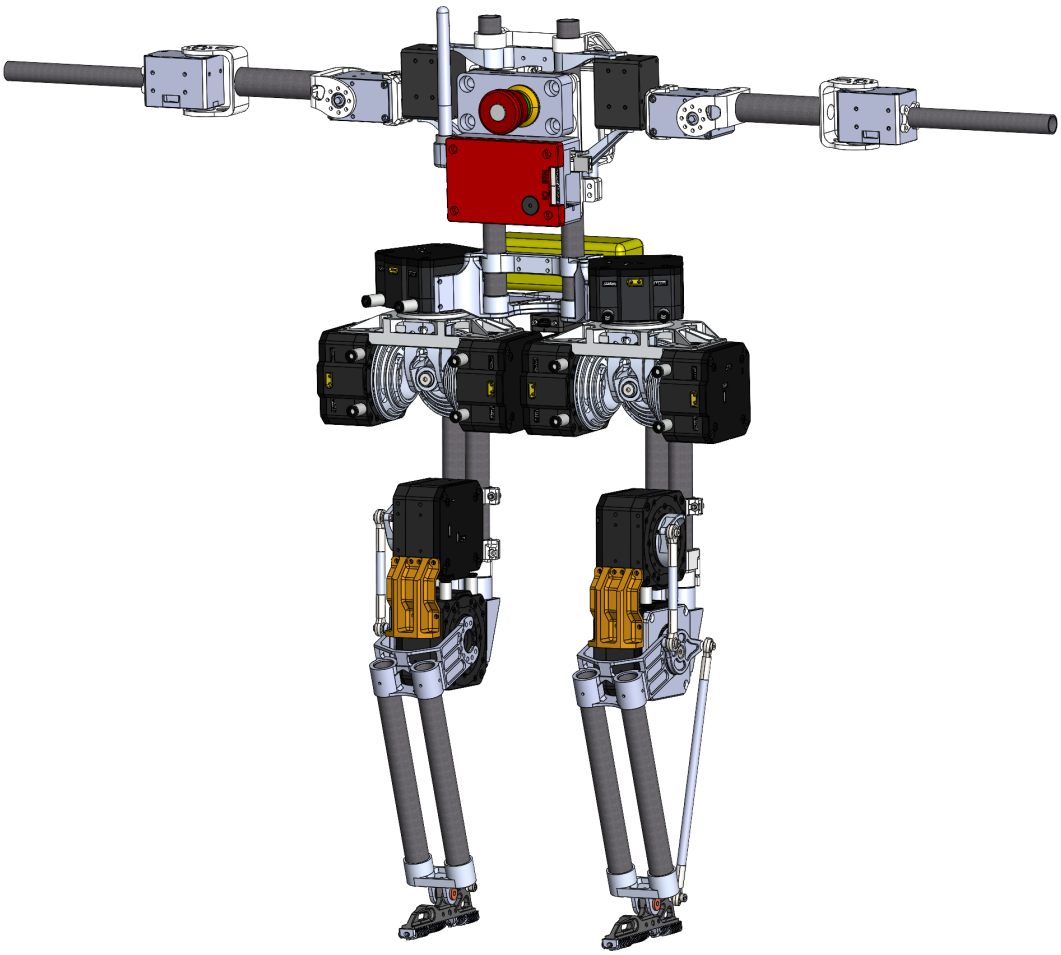

Figure 2.1: BRUCE CAD

2.1 Introduction

Humanoid robots have made significant advancements in hardware design, sensor reliabilities, and control systems, yet dynamic behaviors like running and jumping remain a challenge due to limitations in handling impact with traditional high-gear-ratio motors. While technologies like series elastic actuators and proprioceptive actuators show promise for improving dynamic performance, their adoption in humanoid robots has been limited. Progress in full-sized humanoid robots is limited by complex control requirements and restricted hardware accessibility. These challenges highlight the need for accessible and robust humanoid robot platforms for broader research on lower-body dynamic locomotion.

Conversely, smaller humanoid platforms like RoMeLa's DarwIn-OP [32] offer a more practical option for research through their reduced size and inertia. Building on the accessibility and reliability of existing small-sized humanoid robot platforms and advancements in proprioceptive actuators, we developed the next-generation miniature humanoid platform – Bipedal Robot Unit with Compliance Enhanced (BRUCE) [3], illustrated in Fig. 2.2. To enable human-like dynamic movements, BRUCE's joint configuration and range of motion closely mimic those of a human. Unlike traditional humanoid robots with actuators directly placed at each joint, BRUCE employs a 2-DoF cable-driven differential pulley system for the hip and a 4-bar linkage mechanism for the ankle. This design significantly reduces the leg's moment of inertia and enhances its capacity for dynamic motion. Additionally, the simplified upper body design of BRUCE notably reduces the overall cost and lowers the system weight to improve energy efficiency.

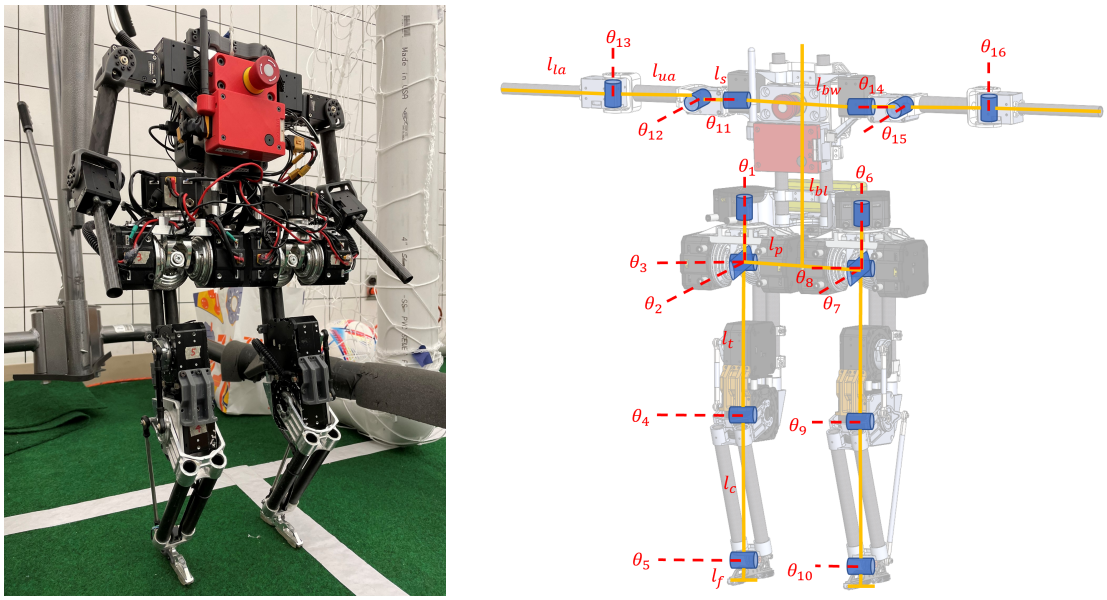

(a) BRUCE Hardware

(b) BRUCE Joint Distribution

Figure 2.2: Bipedal Robot Unit with Compliance Enhanced (BRUCE)

2.2 Mechanical Design

2.2.1 Mechanical Configuration

Joint Configuration To achieve human-like dynamic motions, BRUCE must maintain an adequate range of motion while prioritizing simplicity and a lightweight structure. The upper body features a torso equipped with two 3-DoF arms designed for basic arm gestures, keeping the system functional yet minimalistic. In the lower body, each leg comprises a 5-DoF configuration, including a spherical hip joint, a single DoF knee joint, and a single DoF ankle joint, as depicted in Fig. 2.2. The feet are designed to have a line contact with the ground, eliminating the need for actuation in the foot roll direction and further simplifying the system. While this single DoF ankle design sacrifices some of the foot functionality of maintaining static balance, the benefit of a lighter leg design outweighs this drawback. With the minimum distal mass in the legs, BRUCE has a greater po-

tential to perform highly dynamic locomotion more effectively, despite the minor compromise in foot articulation.

Table 2.1: BRUCE Mechanical Parameters

Parameter	**Symbol**	**Value**	**Parameter**	**Symbol**	**Value**
Body mass	m_b	1551 [g]	Body width	l_{bw}	178 [mm]
Hip mass	m_h	667 [g]	Body length	l_{bl}	185.5 [mm]
Thigh mass	m_t	839 [g]	Pelvis length	l_p	150 [mm]
Calf mass	m_c	96 [g]	Thigh length	l_t	175 [mm]
Foot mass	m_f	24 [g]	Calf length	l_c	169.5 [mm]
Upper arm mass	m_{ua}	75 [g]	Foot length	l_f	24 [mm]
Lower arm mass	m_{la}	53 [g]	Shoulder length	l_s	43 [mm]
Total mass	m	5059 [g]	Upper arm length	l_{ua}	114.5 [mm]
Total height	l	660 [mm]	Lower arm length	l_{la}	143 [mm]

Link Length BRUCE is designed as a miniature bipedal robot with a range of motion closely resembling that of a human's lower body. To achieve this, its dimensions are proportionally scaled down from a full-sized human while maintaining link length ratios consistent with human anatomy. Based on anthropometric data [37], the average length ratios for the upper body, thigh, calf, and foot of an adult male are 28:16.8:16.3:2.3. Using these proportions, BRUCE's total height is set at 660 mm, which is approximately one-third of an average adult male's height. Consequently, the link lengths for BRUCE's upper body, thigh, calf, and foot are determined as 291.5 mm, 175 mm, 169.5 mm, and 24 mm, respectively. Additionally, the distance between the two legs is designed to be 150 mm. This spacing prevents potential collisions between the hip actuators when rotating in the yaw

direction, ensuring smoother and more reliable motion. The detailed summary of BRUCE's key mechanical parameters is provided in Table 2.1, highlighting the thoughtful scaling and minimum weight in each link.

2.2.2 Actuation Selection

To achieve enhanced actuation transparency and compliance when operating in unstructured environments, BRUCE utilizes proprioceptive actuators. These actuators are specifically chosen for their ability to deliver precise and responsive force control, which is essential for dynamic motions and adapting to varying loads. By integrating proprioceptive actuators, BRUCE can mitigate impacts effectively and achieve high torque transparency, allowing for higher bandwidth force control and smoother locomotion.

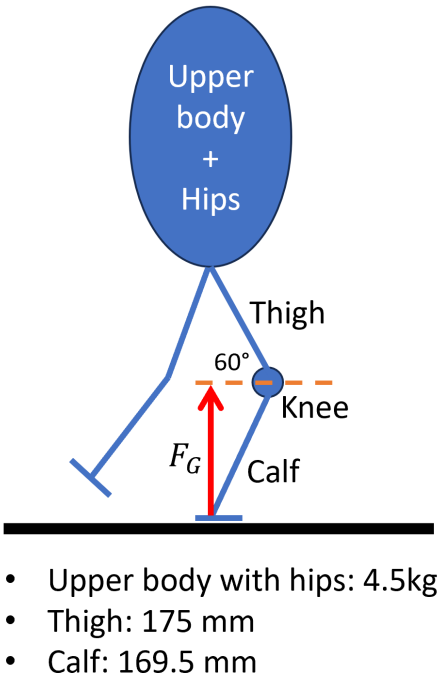

Figure 2.3: Knee actuator static loading case when BRUCE is walking.

The selection of BRUCE's actuators is guided by performance requirements derived from its motion and load conditions. Based on the simplified loading case

as shown in Fig. 2.3, the requirement for the knee actuator, which is usually the actuator that outputs the most torque, can be calculated as below:

$$T_k = F_G \cdot l_t \cdot \cos(60°) = (m_b + 2m_h + 2m_t)g \cdot l_t \cdot \cos(60°) \tag{2.1}$$

We can get T_k = 3.86 Nm for static loading of walking when there is only one foot having contact with the ground. The knee torque requirement for standing can be as low as 1.93 Nm, simply because two feet have contact with the ground.

The Koala BEAR module from Westwood Robotics [38], which is a commercial actuator product based on our previous BEAR module [22], is selected as the actuator for the lower body of BRUCE. This compact proprioceptive actuator is well-suited for BRUCE's requirements, offering real-time feedback on joint states such as position, velocity, and torque. It operates with an embedded microcontroller running an internal control loop at a frequency of 2 kHz, ensuring precise and responsive actuation. More actuator specifications can be found in Table 2.2. The arms on the upper body are powered by DYNAMIXEL XL430-W250-T servo motors from ROBOTIS [39] since they do not require much compliance, which also reduces the overall weight.

Table 2.2: Koala BEAR (Left) and DYNAMIXEL XL430 (Right) specifications

Parameter	**Value**	**Unit**	**Parameter**	**Value**	**Unit**
Weight	250	g	Weight	57	g
Speed Constant	27.3	RPM/V	No Load Speed	61	RPM
Torque Constant	0.035	Nm/A	Voltage	12	V
Gear Ratio	9	/	Gear Ratio	258.5	/
Stall Torque (15 sec)	3.5	Nm	Stall Torque	1.5	Nm
Stall Torque (1.5 sec)	10.5	Nm	Stall Current	1.4	A

2.2.3 Actuation Scheme

With proprioceptive actuators equipped in the lower body, BRUCE's legs are desired to have low inertia to better support dynamic behaviors. Unlike traditional humanoid robots, where actuators are placed directly at each joint, BRUCE's actuators are strategically positioned near the torso to minimize the distal mass of the legs. This requires reconsidering the actuator placement. Previous research has introduced effective methods for reducing leg inertia, including cable-driven systems [40, 41] and linkage mechanisms [42, 43]. Building upon these advancements, BRUCE incorporates a 2-DoF cable-driven differential pulley system for hip pitch and roll motions. Additionally, the ankle joints are actuated using two pairs of 4-bar linkage mechanisms, further decreasing the distal mass and improving overall efficiency in dynamic movements.

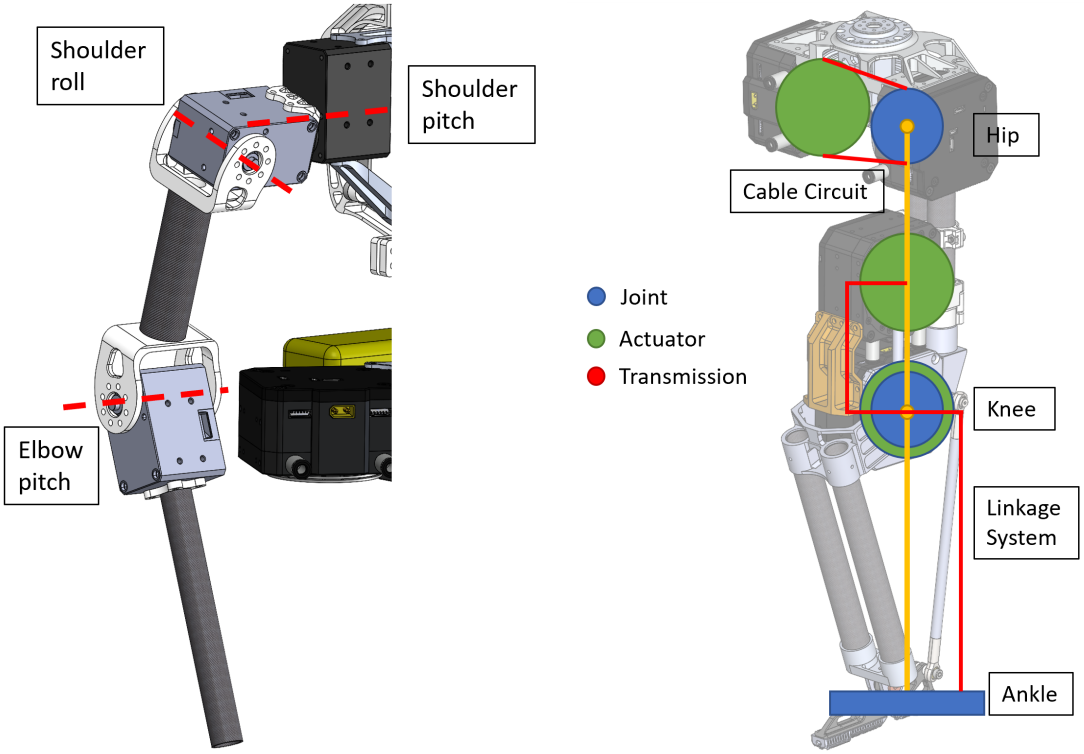

(a) BRUCE upper body joint location

(b) BRUCE lower body joint actuation

Figure 2.4: Actuation scheme of BRUCE

For the upper body, the arm servo motors are mounted directly at the joints. This straightforward approach prioritizes simplicity in the upper body design while maintaining sufficient functionality for BRUCE's intended applications.

2.2.4 Hip Design

Rather than arranging two actuators in a serial configuration for the hip's pitch and roll joints, BRUCE employs a 2-DoF parallel actuation setup inspired by automotive differential gearing. This design allows both actuators to be mounted directly at the hip, significantly lowering the mass and inertia of the femur link. Additionally, the parallel configuration doubles the available torque at the hip pitch and roll joints since both actuators work together to power the same joint. This increased torque capacity is advantageous for BRUCE during dynamic sagittal plane motions, which are common in activities like walking and jumping.

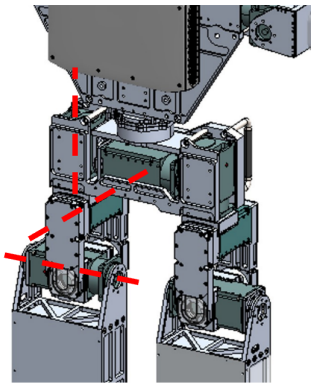

(a) Thor RD hip [44]

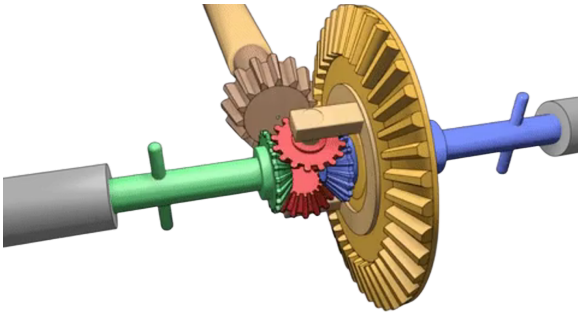

(b) Car differential gearing

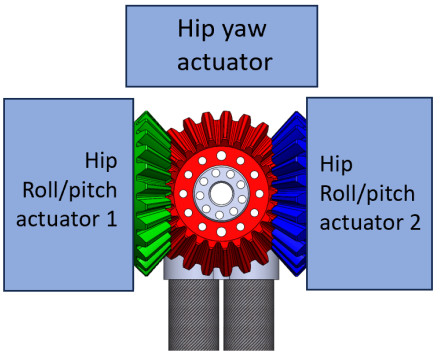

(c) Differential gearing hip

Figure 2.5: Inspiration of the differential gearing hip design

Hip Design, Rev. 1

The initial prototype of BRUCE [45] utilized bevel gears to implement the parallel actuation scheme for the hip due to their straightforward installation. However, this design presented several significant issues. Firstly, the legs experienced noticeable wobbling, and the accuracy of the hip joint was compromised due to backlash in the gears. Additionally, the bevel gears were both costly and heavy, making them unsuitable for an affordable and lightweight dynamic humanoid robot platform. Furthermore, the grease applied to the gear teeth often created a mess, complicating the maintenance of the hardware.

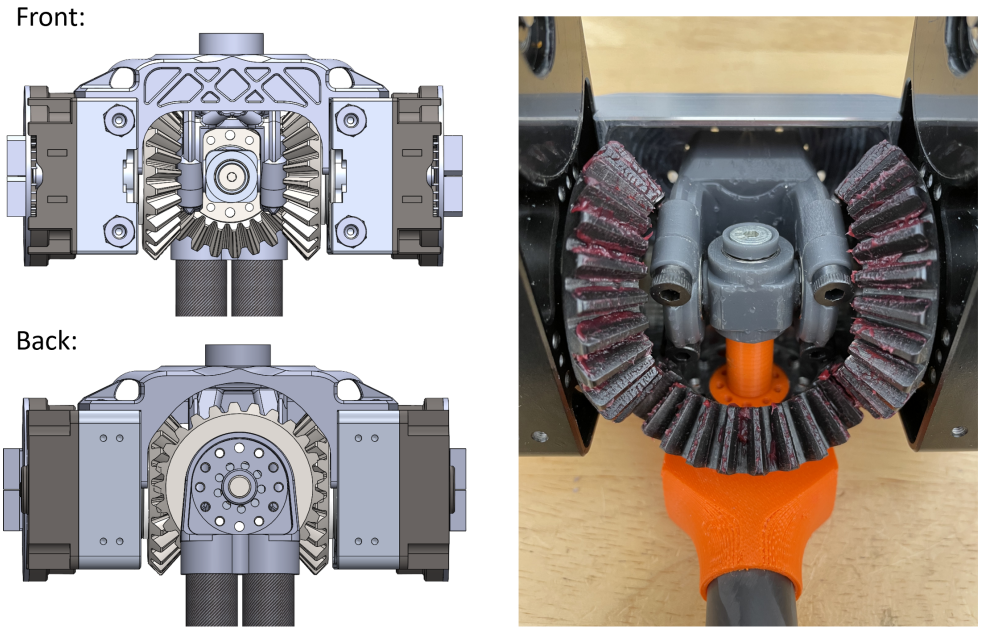

Figure 2.6: The previous hip design utilizing bevel gears

Hip Design, Rev. 2

To enhance joint accuracy and stability, a compact cable transmission system featuring a cable-driven differential pulley [46] has been innovatively adopted for the hip joint. This approach has been utilized successfully in other robotic joints such as the torso [47] and shoulder [48], offering a promising alternative to traditional bevel gears. Although it adds complexity to the installation process,

the cable-driven differential pulley system provides a significant advantage with its zero-backlash performance. Additionally, unlike gears that require lubrication with grease, the cable and pulley system operates without lubrication, contributing to a cleaner and more maintenance-friendly hip assembly.

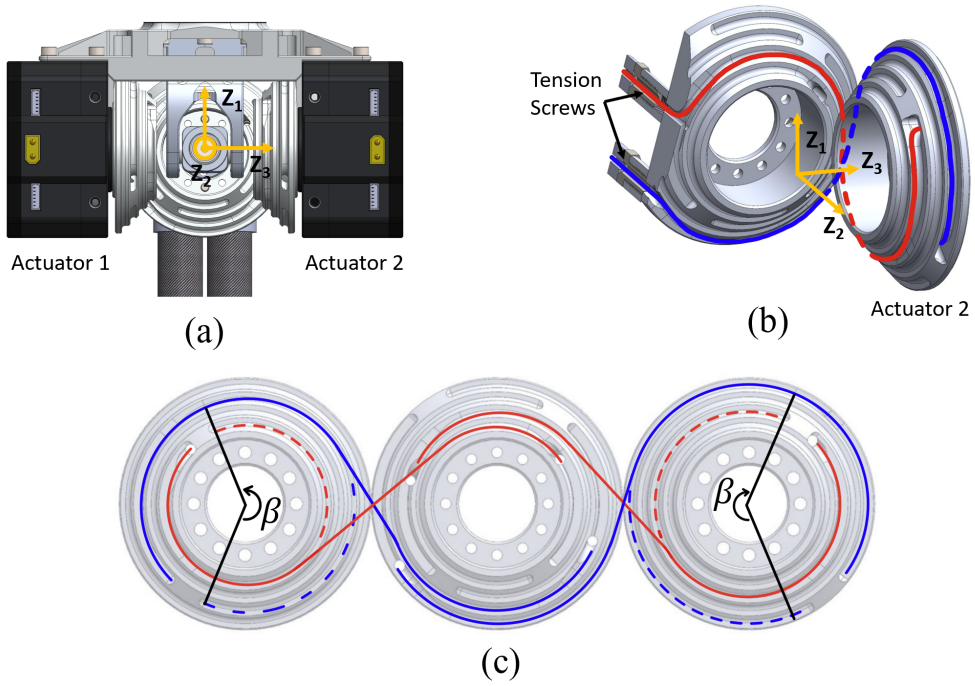

Figure 2.7: The modified hip design with cable-driven system: (a) Spherical hip joint. (b) Assembly of pulleys and cables, where the cables are pre-tensioned by screws. (c) Wiring diagram of the 2-DoF cable-driven differential pulley system, where β denotes the effective rotational range of the pulley, corresponding to the hip roll motion's range.

The 2-DoF cable-driven differential pulley system is depicted in Fig. 2.7. To enable effective actuation of the hip joint in both pitch and roll directions without slippage, each pulley linked to the hip actuators requires a minimum of two cables. Consequently, the pulley connected to the femur link utilizes a total of four cables. As illustrated in Fig. 2.7 (b), the blue cable becomes active when Actuator 2 rotates in the positive z_3 direction, while the red cable engages during reverse rotation.

Cable-driven transmission systems typically require cable pretension to ensure a rigid and reliable connection. To minimize the need for frequent cable tension

adjustments, the minimum wrapping radius, R_{min}, around the pulley must be carefully determined to prevent the cable from being subjected to excessive load. Taking into account the actuator's maximum torque, T_{max}, and the material properties of the cable, the minimum wrapping radius is calculated as follows.

$$R_{\min} = \frac{T}{F_y} \leq \frac{T_{\max}}{F_y} = \frac{T_{\max}}{(\sigma_y \cdot \pi r_c^2)}, \tag{2.2}$$

where σ_y is the yield stress of the cable material, and r_c is the radius of the cable. Moreover, there is a safety factor n to make sure there is a margin for safety. For BRUCE, $T_{\max}$ = 10.5 Nm for the actuator, σ_y = 215 MPa and r_c = 2.4 mm for a 304 stainless steel cable, the value of $R_{\min}$ is calculated to be 16.2 mm for a safety factor of 1.5. On the real hardware application, it is adjusted to 19 mm to properly fit into the assembly, as well as for a larger safety factor.

As shown in Fig. Fig. 2.7(c), the angle β defines the effective rotation region of the pulley, while the remaining area outside this region is primarily used for cable retention. To ensure proper functionality, the value of β must exceed the anticipated range of motion for the hip roll joint.

The parallel configuration of the hip joint for pitch and roll directions results in coupling between the two actuators. As shown in Fig. 2.7(b) and Fig. 2.7(c), pure pitch motion is achieved when the two side pulleys rotate by the same angle but in opposite directions. Conversely, synchronous rotation in the same direction results in pure roll motion. Any other combination of rotations leads to simultaneous pitch and roll movements.

To demonstrate that the cable-driven differential pulley system exhibits significantly less backlash compared to the traditional bevel gear differential system, a comparative experiment was conducted. In this test, two hip assemblies with different designs were mounted in a fixed position, with a background reference sheet

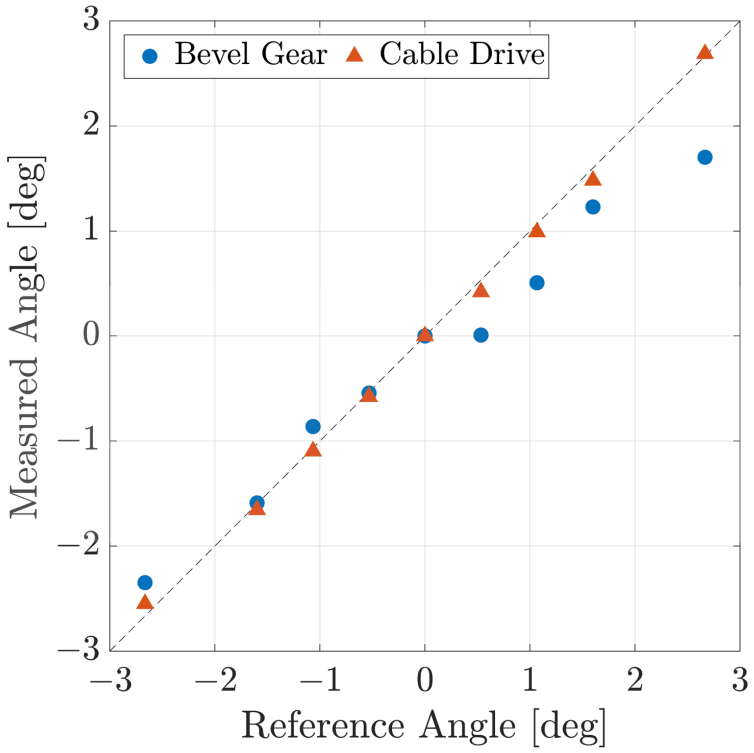

Figure 2.8: Comparison of the joint backlash between the cable-driven hip design and the bevel gear hip design

containing marked points placed behind them. For data collection, the thigh link of each assembly was manually aligned to the reference points, and the angular readings from the two hip actuators were recorded. The results are presented in Fig. 2.8, revealing that the angles measured from the cable-driven hip joint closely match the reference points, whereas the bevel gear-based hip joint exhibited lower accuracy.

Additionally, since the cable-driven transmission is utilized in the hip joint, it is essential to analyze joint stiffness, as it may be influenced by the elongation of the cable. The axial stiffness of the cable denoted as k_c, is determined as follows.

$$k_c = \frac{AE_c}{L_c} = \frac{\pi r_c^2 \cdot E_c}{2\pi R} = \frac{r_c^2 E_c}{2R}. \tag{2.3}$$

where A and L_c are the cross-sectional area and the length of the cable, and E_c is Young's Modulus for the cable material.

By knowing k_c, the joint stiffness k_j can then be determined to be

$$k_j = \frac{T}{\Delta\theta} = \frac{FR}{\delta/R} = (F/\delta)R^2 = k_c R^2 = \frac{1}{2} r_c^2 E_c R, \tag{2.4}$$

where $\delta = F/k_c$ is the cable elongation and $\Delta\theta$ is the resultant joint rotation angle.

$$\delta = \frac{FL_c}{AE} = \frac{(T_{\max}/R_{\min})(2\pi R_{\min})}{(\pi r_c^2)E} = R_{\min}\Delta\theta, \tag{2.5}$$

With the pulley radius R = 19 mm, cable radius r_c = 2.4 mm and Young's modulus $E_c = 1.9 \times 10^{11}$ N/m^2 for the 304 stainless steel, the calculated hip joint stiffness k_j is 10,397 Nm/rad. This value is sufficiently high, as the actuator's maximum torque is only 10.5 Nm. The resultant joint rotation due to cable elongation is 0.058° at worst, making it negligible. This confirms that the chosen cable-driven transmission provides adequate joint stiffness. Furthermore, each cable is carefully pre-tensioned using the adjustment screws shown in Fig. 2.7(b) to ensure consistent and reliable power transmission.

2.2.5 Leg Design

The femur and tibia components of BRUCE are constructed using carbon fiber tubes, valued for their exceptional strength-to-weight ratio, combined with precision-machined aluminum parts. This strategic use of lightweight yet robust materials ensures structural durability without compromising the robot's mobility. To minimize the tibia's weight, the actuators for the knee and ankle joints are positioned

within the femur. However, relocating the ankle actuator to the femur required a mechanism to transfer torque effectively to the ankle joint. While timing belts are often used for their simplicity and ability to transmit continuous rotations, their low stiffness introduces compliance between the belt teeth and the pulley. This reduces the resonant frequency of the system, limiting the joint's torque control bandwidth [49]. To address this issue, BRUCE employs a stiffer and more reliable torque transmission solution: the 4-bar linkage mechanism.

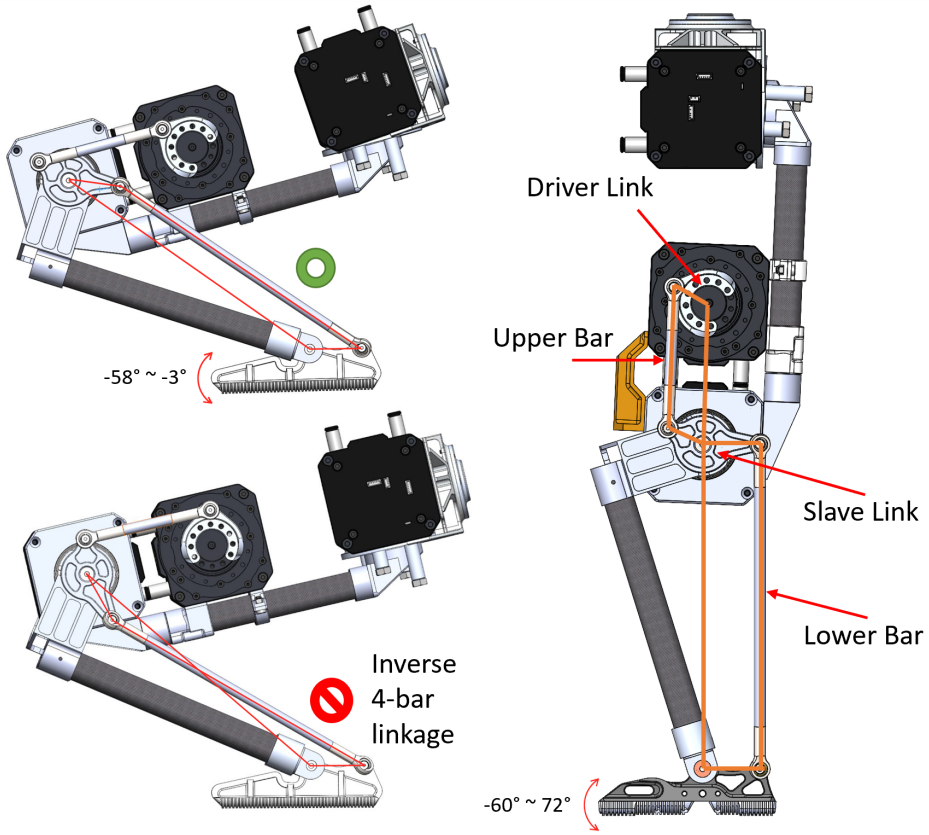

Figure 2.9: Bruce leg linkage mechanism design

As illustrated in Fig. 2.9, BRUCE uses two pairs of parallelogram-configured 4-bar linkages to transmit torque from the actuator to the ankle joint with a 1:1 transmission ratio. Since the lower bar in this torque transmission configuration is a thin, elongated component, it is essential to verify its buckling resistance. The buckling load F_{buckling} determines the minimum radius r_l required to ensure the

lower bar does not fail under extreme loads, calculated using:

$$F_{\text{buckling}} = \frac{\pi^2 E_l I}{L_l^2} \geq \frac{T_{\max}}{l}, \tag{2.6}$$

where E_l, I, L_l, l are the Young's Modulus for the lower bar material, the moment of inertia of its cross-section, its length, and the moment arm of the slave link, respectively. To match with the tibia link length, we need to use a 169.5 mm long aluminum rod with $E_l = 6.9 \times 10^{10}$ N/m^2 and $I = \pi r_l^2/4$. With $T_{\max} = 10.5$ Nm for the actuator and $l = 30$ mm, the calculation of (2.6) shows that a minimum radius of 3 mm is required for the lower bar, incorporating a safety factor of 1.5. Moreover, due to the coupling of the knee and ankle joints, the ankle joint motion depends on the knee configuration. Table 2.4 details the ankle joint's range of motion across various knee angles. Although the ankle's range is somewhat restricted when the knee is highly flexed, such as during squatting, it still fulfills the requirements of the intended locomotion applications.

2.2.6 Foot Design

To enable BRUCE to detect foot-ground contact for state estimation in unstructured environments, a lightweight and reliable contact sensing module was developed, as shown in Fig. 2.10. This sensor operates on the principle of an electronic switch. In its assembly, two copper foils are adhered to a plastic contact layer, which is then secured to an aluminum base with screws. When the foot touches the ground and the contact force exceeds a specific threshold, the plastic layer bends, causing the copper foil to meet the aluminum base and close the circuit. To determine the trigger force, a simple experiment was conducted using a custom 2-DoF testbed and a precise scale. The foot module was gradually pressed downward, and the contact force at which the sensor detected ground contact was

recorded. Results showed consistent trigger forces of 1.18 N for the toe and 2.45 N for the heel, regardless of contact angle, ensuring reliable sensing for ground-touching events.

Figure 2.10: BRUCE contact sensing foot V1 design (left) and the actual hardware (right)

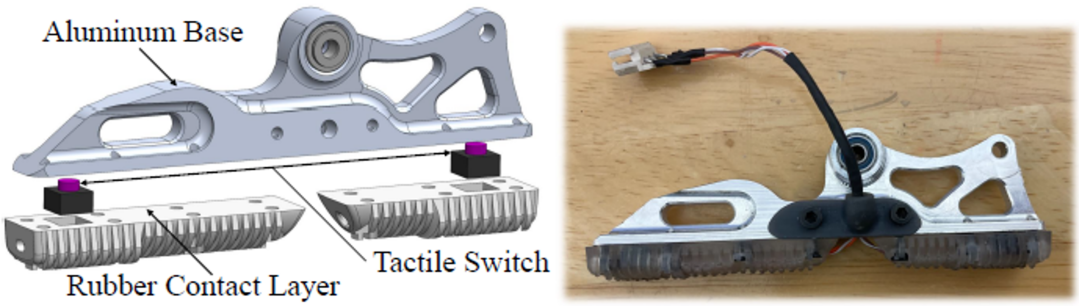

Figure 2.11: BRUCE contact sensing foot V2 design (left) and the actual hardware (right)

However, potential false positive detections could occur when the leg swings with high acceleration, as the plastic layer might bend due to inertia. Despite this, the lightweight plastic contact layer (weighing only 1.5 g) would require accelerations of approximately 80 g and 166 g for the toe and heel respectively to trigger false detections, which is well beyond BRUCE's operational conditions.

During hardware trials, modifications were made to enhance the reliability of the sensing foot. The original plastic layer occasionally failed under impact forces during touchdown, and dust accumulation on the copper foils degraded contact quality. In the improved design, off-the-shelf tactile switches are embedded directly into a rubber contact layer to serve as contact sensors, as shown

in Fig. 2.11. This modification makes the foot touchdown more compliant while isolating the contact detection mechanism from external elements, significantly enhancing performance and durability.

2.2.7 Lower Body Range of Motion

The design objective of BRUCE's lower body is to replicate the dynamic locomotion of humans, requiring a range of motion comparable to that of the human lower body. As illustrated in Fig. 2.12, the comparison reveals that BRUCE's lower body achieves an even greater range of motion than that of a human.

Table 2.3: BRUCE lower body range of motion (expect ankle)

Joint	**Min. Angle**	**Max. Angle**
Hip Yaw	−180°	180°
Hip Roll	−55°	55°
Hip Pitch	−140°	25°
Knee	−45°	140°

Table 2.4: BRUCE Ankle Joint Range of Motion

Knee Angle*	−30°	0°	30°	60°	90°	120°
Min. Ankle Angle†	−25°	−60°	−58°	−58°	−58°	−58°
Max. Ankle Angle†	77°	72°	50°	28°	−3°	−32°

*The positive direction is when the knee flexes.
†The ankle joint is measured as 0° when the foot is positioned perpendicular to the tibia, with the positive direction defined as the foot bending upward.

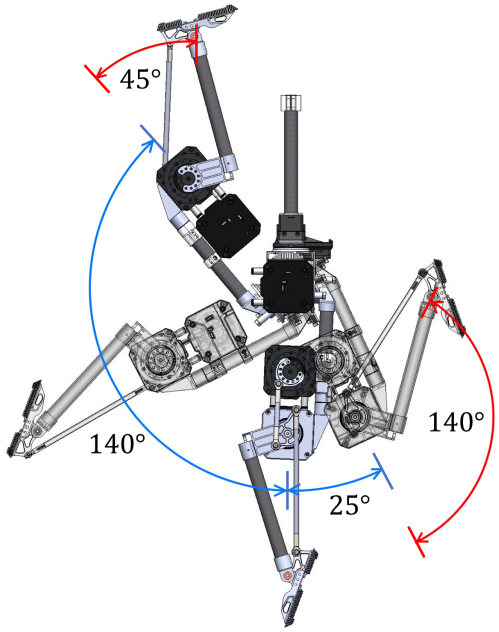

(a) BRUCE Flexion / Extension

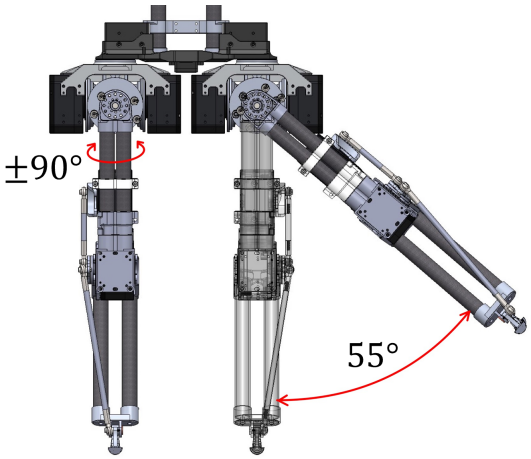

(b) BRUCE Abduction

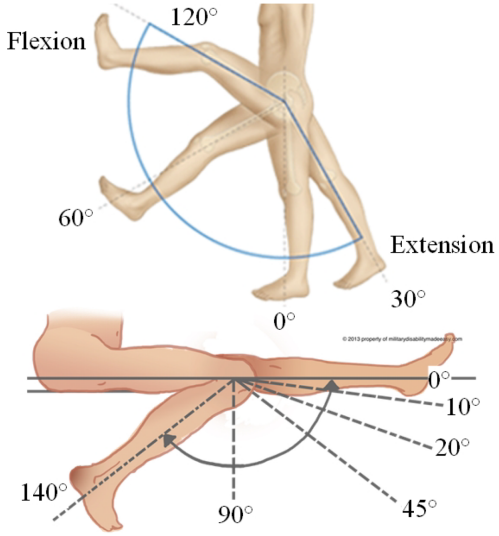

(c) Human Flexion / Extension

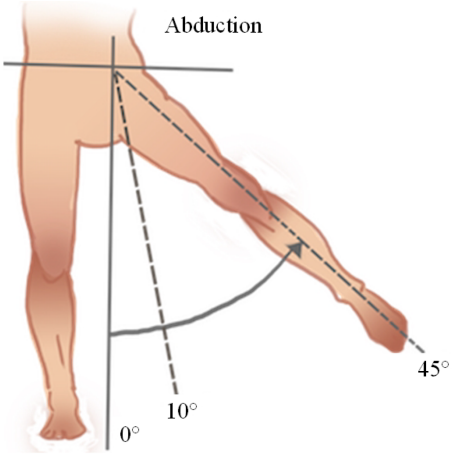

(d) Human Abduction

Figure 2.12: Comparison of the lower body range of motion between BRUCE and humans

2.2.8 Upper Body Design

The upper body of BRUCE has been carefully designed with a focus on simplicity and minimizing weight. This design choice ensures that the robot remains agile

and capable of performing dynamic movements with ease. As a result, only the most essential components are included in the upper body, with a total mass of 1.5 kg. These components consist of two functional arms and a torso structure that houses all necessary electronics, allowing for efficient power distribution and control while keeping the upper body compact and lightweight.

At present, the upper body does not include a head or camera system. However, this design allows for potential future upgrades, making it feasible to add a head or camera module later on to enable vision-based functionalities if needed.

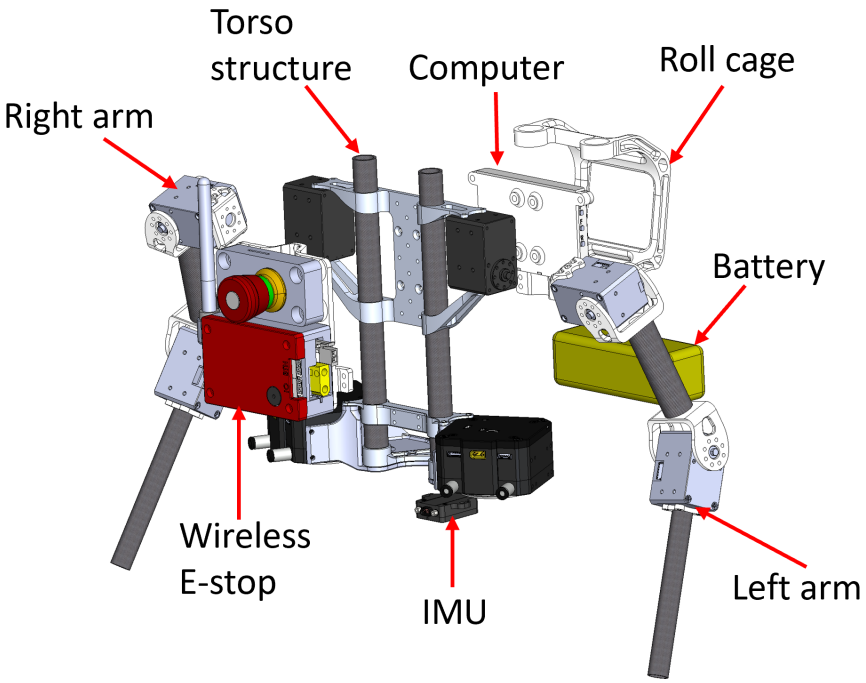

Figure 2.13: BRUCE upper body components exploded view

Torso Design

In order to not bring extra weight to the whole platform, the torsos structure is made of carbon fiber tubes and topology-optimized aluminum machined parts. The two legs and two arms are directly connected to this central torso structure, allowing for a compact and streamlined design that supports the robot's dynamic movement capabilities while minimizing additional load.

To prevent BRUCE from doing undesired movement as well as for safety purposes, there is a set of in-house developed wireless E-stop [9] equipped in front of BRUCE's chest. The computer installed at the back of BRUCE is Khadas Edge 2, an ultraslim, credit-card-sized ARM PC powered by RK3588S. The 2000 mAh 4S 50C 14.8V Lipo battery from Liperior is selected as the main battery for BRUCE, which can last about 25 minutes while BRUCE is walking. In addition, the IMU used to keep track of the orientation, position, speed and acceleration is Adafruit ISM330DHCX 6-DOF IMU, which is highly accessible and easy to use.

Arm Design

There are two 3-DoF arms for the minimum hand gestures. Each of the arms has a shoulder pitch, shoulder roll and elbow pitch joints powered by DYNAMIXEL XM430-W210 actuators, as shown in Fig. 2.4. To avoid adding unnecessary weight to the entire platform, carbon fiber tubes and 3D-printed Nylon parts are used as links and brackets in the arm.

2.3 Design Optimization

2.3.1 Design Optimization Methods

To make sure BRUCE is able to perform highly dynamic behaviors, one of the design innovations applied to BRUCE hardware is the design optimizations to pursue a lightweight yet strong overall hardware system design. There are two main trends to optimize the part design and strength-to-weight ratio: Topology Optimization [50, 51] and Generative design [52]. Based on different part applications and desired manufacturing methods, topology optimization and generative design bring different optimization approaches to the part to achieve the optimized strength-to-weight ratio.

Topology optimization usually applies to the mature design phase of the part,

where the initial part geometry already exists or there are specific requirements on the part geometry. By knowing all the loading cases and the desired part strength, the software will run the simulation repeatedly to remove unnecessary materials in the part to minimize the mass. Thus, topology optimization is usually applicable to subtractive manufacturing, such as CNC machining.

(a) Topology Optimization

(b) Generative Design

Figure 2.14: Examples of topology optimization and generative design

On the other hand, generative design happens in the initial design phase, where we do not have the part geometry or there are no limitations on how the part should look like. Based on the loading cases, the generative design will grow the part like organic systems, such as plants and bones. By the end of the optimization, the generative design will provide the final part with different shapes,

densities, and orientations of structures. Because of the complexity of the part geometry after generative design, it usually only works for additive manufacturing like 3D printing.

Since all the structural parts of BRUCE are planned to be manufactured as machined aluminum parts, topology optimization is applied to the parts to reduce the weight while maintaining the required part strength.

2.3.2 Topology Optimization

Thanks to modern CAD software like SolidWorks and Fusion 360, topology optimization is accessible to us and easy to use, by just running the topology simulations in the software. The entire topology optimization process has 6 steps, as shown in Fig. 2.15.

The part shown in the Fig. 2.15 is the knee bracket of BRUCE, which is one of the most important parts of the lower body structure. As BRUCE performs highly dynamic bipedal locomotion like running and jumping, there will be multiple loadings acting on the knee joint, including compression, torque, and moments. To make sure BRUCE performs well under different loading conditions, it is necessary to apply topology optimization to improve the strength-to-weight ratio of the knee bracket.

The original CAD of the knee bracket is designed based on the insight of how the part geometry should look alike. In order to let the computer run topology optimization to enhance the part design, we have to maximize the part envelope and intentionally make the part look beefier, so there is more room for the topology optimizer to play and the result could be much better. The 3rd step is to throw the part to a topology study and define all the fixtures and loading conditions so that the software knows what to do in the simulation. After the topology study is completed, the result would show the designer which materials in the part can be

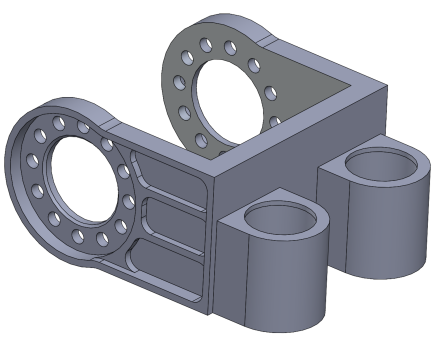

(a) Step 1: Original CAD

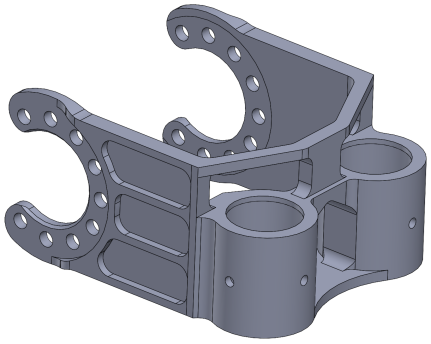

(b) Step 4: Re-designed CAD

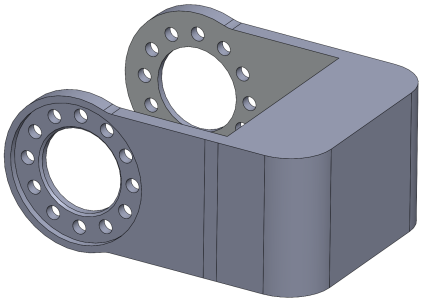

(c) Step 2: Maximum part envelop

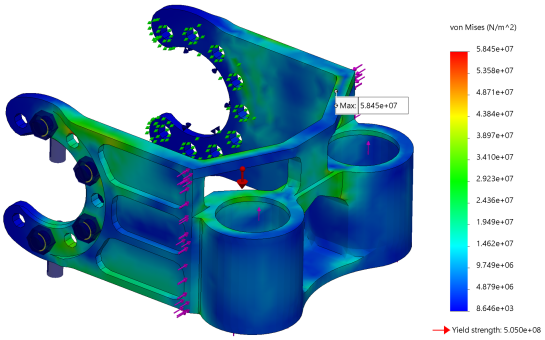

(d) Step 5: Repeated FEA analysis

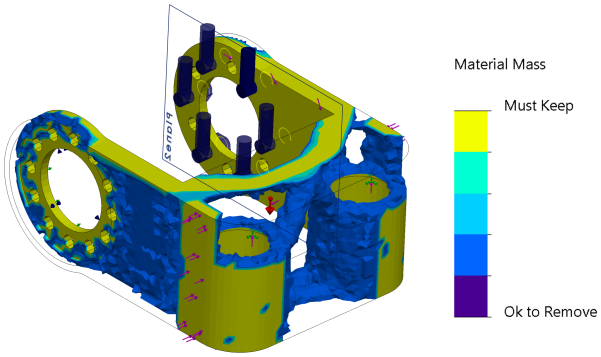

(e) Step 3: Topology Optimization

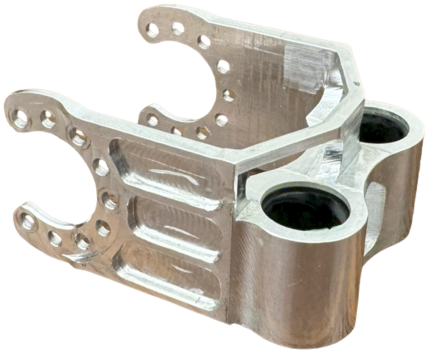

(f) Step 6: Final CNC manufacturing

Figure 2.15: The topology optimization process

taken off, and in which region there has to be enough material to keep the part with the desired strength. Based on the meshed geometry, we can redesign the knee bracket so it follows the topology-optimized geometry. At the same time, we should also keep in mind that the part will be later manufactured using the CNC machine, so we need to consider the machinability of the re-designed knee bracket.

The re-designed knee bracket only has a mass of 28.45 g, which is 20% less

weight compared to the original part of 35.72 g. Moreover, it is necessary to run the repeated FEA analysis to the new part, to make sure the part will not have mechanical failure under all the loading conditions. The FEA analysis result of both the original design and the topology-optimized design under the same loading conditions is attached below in Fig. 2.16.

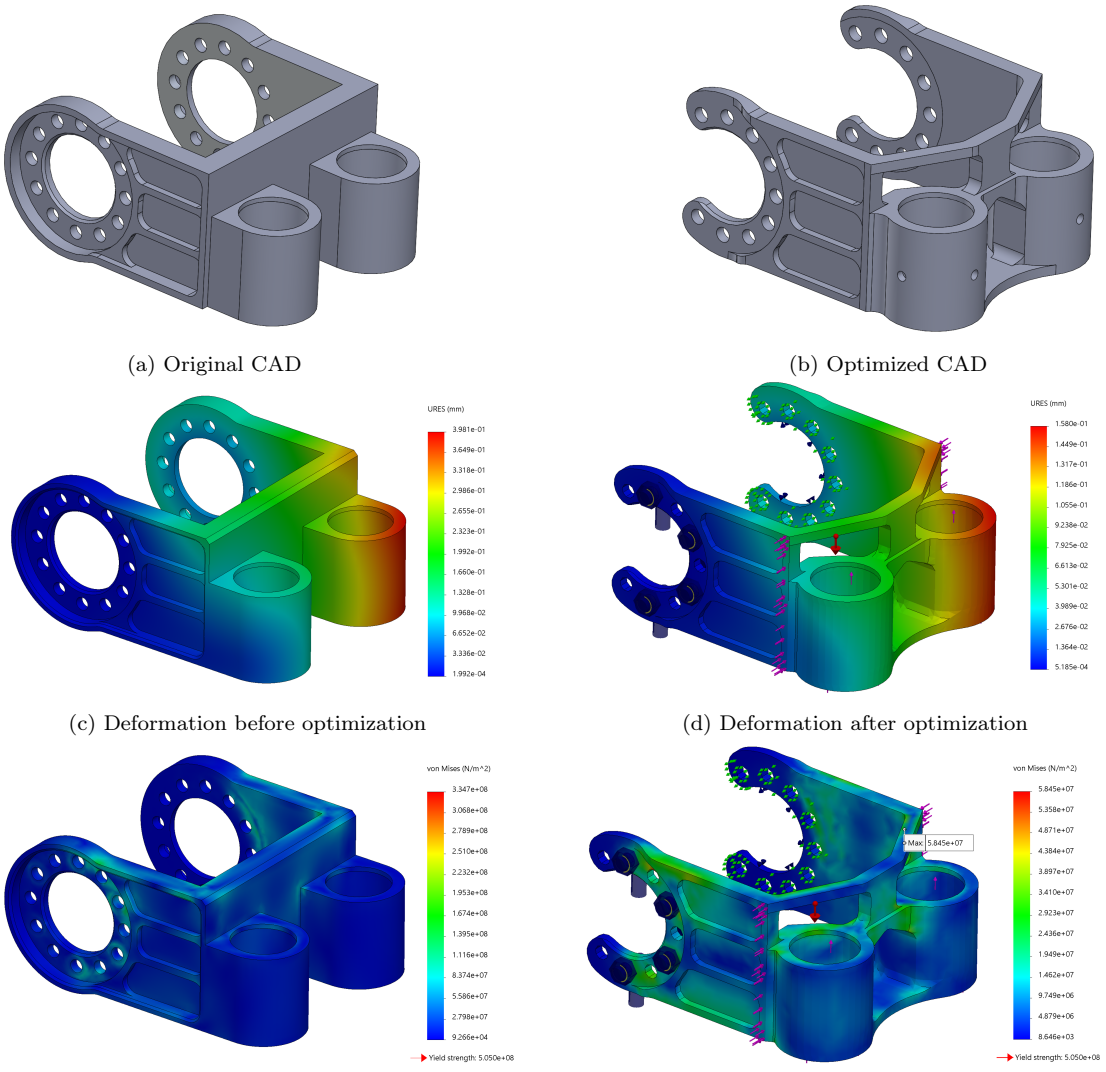

(a) Original CAD

(b) Optimized CAD

(c) Deformation before optimization

(d) Deformation after optimization

(e) Stress before optimization

(f) Stress after optimization

Figure 2.16: The comparison of the FEA results between the original design and topology optimized design

As we can see from the figure above, the maximum deflection of the knee bracket reduced from 0.398 mm to 0.158 mm, which is 60% less deformation

compared to the original part. Moreover, the maximum stress of the part reduced dramatically from 335 MPa to 58.5 MPa, which means the stress will be more evenly distributed in the topology-optimized knee bracket under the same loading conditions. By applying topology optimization, the knee bracket not only got mass reduced, but also increased the part strength and stiffness, which is the ideal case of topology optimization. After all the analysis is complete, the final step is to manufacture the knee bracket part using a CNC machine. And the machined part will be assembled to BRUCE lower body hardware.

The topology optimization is later applied to the other structural parts in BRUCE's lower body to minimize the weight of the lower body while maintaining the desired structural reliability. However, the optimized part will not always reduce the mass and at the same time gain more stiffness after the topology optimization. For most cases, the part usually reduces $20\% - 30\%$ of the mass, and the stiffness is also reduced to a safety margin for all possible loading conditions.

2.4 Kinematics

BRUCE's leg kinematics are analyzed by approaching it as a manipulator problem and applying the modified Denavit-Hartenberg (DH) method, referring to my colleague Junjie Shen's work [2]. The frame assignments are shown in Fig. 2.17, while the corresponding DH parameters are listed in Table 2.5. For clarity, some intermediate frames have been omitted, which means that not all spatial relationships are fully captured by the DH parameters.

The kinematics for BRUCE's left and right legs are almost identical, with only two key differences. Firstly, the parameter h_y has opposite signs: it is positive for the left leg and negative for the right. Secondly, there is a variation in how the DH joint angle θ relates to the actuator angle q. Although the joint directions are consistent, the legs are symmetric, and the actuators face inward toward each

other. These distinctions will be elaborated on in subsequent sections.

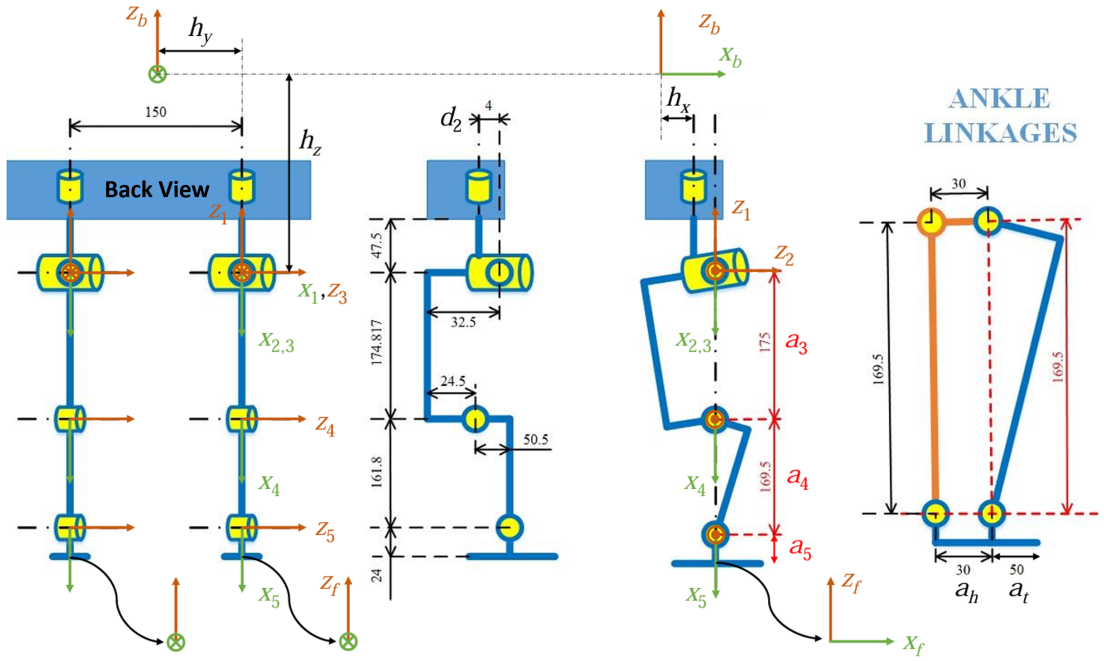

Figure 2.17: BRUCE frame Schematics [2]

Table 2.5: Modified Denavit-Hartenberg Parameters [2]

i	α_{i-1}	a_{i-1}	d_i	θ_i
2	$-\pi/2$	0	0	θ_2
3	$\pi/2$	0	0	θ_3
4	0	a_3	0	θ_4
5	0	a_4	0	θ_5

2.4.1 Forward Kinematics

Forward Kinematics focuses on determining the position and orientation of a target frame using specified joint variables. This is achieved by first deriving the homogeneous transformation matrices that describe the relationship between adjacent link frames. These matrices are then sequentially multiplied to compute the

overall position and orientation of the target frame relative to the base frame. For the right leg, the corresponding individual transformation matrices are calculated as follows:

$$ {}^{b}_{1}\boldsymbol{T} = \begin{bmatrix} \cos\theta_1 & -\sin\theta_1 & 0 & h_x \\ \sin\theta_1 & \cos\theta_1 & 0 & -h_y \\ 0 & 0 & 1 & -h_z \\ 0 & 0 & 0 & 1 \end{bmatrix}, \quad {}^{1}_{2}\boldsymbol{T} = \begin{bmatrix} \cos\theta_2 & -\sin\theta_2 & 0 & 0 \\ 0 & 0 & 1 & 0 \\ -\sin\theta_2 & -\cos\theta_2 & 0 & 0 \\ 0 & 0 & 0 & 1 \end{bmatrix}, \tag{2.7} $$

$$ {}^{2}_{3}\boldsymbol{T} = \begin{bmatrix} \cos\theta_3 & -\sin\theta_3 & 0 & 0 \\ 0 & 0 & -1 & 0 \\ \sin\theta_3 & \cos\theta_3 & 0 & 0 \\ 0 & 0 & 0 & 1 \end{bmatrix}, \quad {}^{3}_{4}\boldsymbol{T} = \begin{bmatrix} \cos\theta_4 & -\sin\theta_4 & 0 & a_3 \\ \sin\theta_4 & \cos\theta_4 & 0 & 0 \\ 0 & 0 & 1 & 0 \\ 0 & 0 & 0 & 1 \end{bmatrix}, \tag{2.8} $$

$$ {}^{4}_{5}\boldsymbol{T} = \begin{bmatrix} \cos\theta_5 & -\sin\theta_5 & 0 & a_4 \\ \sin\theta_5 & \cos\theta_5 & 0 & 0 \\ 0 & 0 & 1 & 0 \\ 0 & 0 & 0 & 1 \end{bmatrix}, \quad {}^{5}_{6}\boldsymbol{T} = \begin{bmatrix} 0 & 0 & -1 & a_5 \\ 1 & 0 & 0 & a_6 = a_t/a_m/a_h \\ 0 & -1 & 0 & 0 \\ 0 & 0 & 0 & 1 \end{bmatrix}, \tag{2.9} $$

Where $a_6 = a_t > 0$ to the toe, $a_m = 0$ for the middle, $a_h < 0$ to the heel, and the overall transformation matrix is determined to be

$$ {}^{b}_{6}\boldsymbol{T} = {}^{b}_{1}\boldsymbol{T}\,{}^{1}_{2}\boldsymbol{T}\,{}^{2}_{3}\boldsymbol{T}\,{}^{3}_{4}\boldsymbol{T}\,{}^{4}_{5}\boldsymbol{T}\,{}^{5}_{6}\boldsymbol{T} = \begin{bmatrix} r_{11} & r_{12} & r_{13} & p_x \\ r_{21} & r_{22} & r_{23} & p_y \\ r_{31} & r_{32} & r_{33} & p_z \\ 0 & 0 & 0 & 1 \end{bmatrix}, \tag{2.10} $$

where the variables

$$r_{11} = -c_1c_2s_{345} - s_1c_{345}, \tag{2.11}$$

$$r_{21} = -s_1c_2s_{345} + c_1c_{345}, \tag{2.12}$$

$$r_{31} = s_2s_{345}, \tag{2.13}$$

$$r_{12} = -c_1s_2, \tag{2.14}$$

$$r_{22} = -s_1s_2, \tag{2.15}$$

$$r_{32} = -c_2, \tag{2.16}$$

$$r_{13} = -c_1c_2c_{345} + s_1s_{345}, \tag{2.17}$$

$$r_{23} = -s_1c_2c_{345} - c_1s_{345}, \tag{2.18}$$

$$r_{33} = s_2c_{345}, \tag{2.19}$$

$$p_x = h_x + c_1c_2\left(a_3c_3 + a_4c_{34} + a_5c_{345} - a_6s_{345}\right) - s_1\left(a_3s_3 + a_4s_{34} + a_5s_{345} + a_6c_{345}\right), \tag{2.20}$$

$$p_y = -h_y + s_1c_2\left(a_3c_3 + a_4c_{34} + a_5c_{345} - a_6s_{345}\right) + c_1\left(a_3s_3 + a_4s_{34} + a_5s_{345} + a_6c_{345}\right), \tag{2.21}$$

$$p_z = -h_z - s_2\left(a_3c_3 + a_4c_{34} + a_5c_{345} - a_6s_{345}\right). \tag{2.22}$$

Note that we denote $c_{ijk} = \cos(\theta_i + \theta_j + \theta_k)$ and $s_{ijk} = \sin(\theta_i + \theta_j + \theta_k)$ for simplicity.

2.4.2 Inverse Kinematics

The derivation of the inverse kinematics for BRUCE refers to Junjie Shen's work [2]. To simplify the process, the Inverse Kinematics is currently developed considering $a_6 = a_m = 0$ and adding nonzero a_6 will only affect θ_3, θ_4, and θ_5.

It is important to note that each leg has only 5 degrees of freedom (DoFs), which is one less than the 6 DoFs required for full spatial manipulation. Consequently, arbitrary configurations of both position and orientation cannot be achieved. However, for our purposes, the focus is primarily on achieving a 3-DoF

positional configuration, along with 2 DoFs for controlling the direction of the x_6−axis in the ground frame $\{g\}$, such as ensuring the foot remains parallel to the ground.

Given the goal ${}^{w}_{b}\boldsymbol{T}$, ${}^{g}_{6}\boldsymbol{T}$, where $\{w\}$ is the world/inertia frame, we have

$$
{}^{b}_{6}\boldsymbol{T} = {}^{w}_{b}\boldsymbol{T}^{-1}\,{}^{w}_{g}\boldsymbol{T}\,{}^{g}_{6}\boldsymbol{T} = \begin{bmatrix} {}^{b}_{w}\boldsymbol{R} & {}^{b}\boldsymbol{p}_{w} \\ \mathbf{0} & 1 \end{bmatrix}\begin{bmatrix} {}^{w}_{g}\boldsymbol{R} & \mathbf{0} \\ \mathbf{0} & 1 \end{bmatrix}\begin{bmatrix} {}^{g}\boldsymbol{x}_6 & {}^{g}\boldsymbol{y}_6 & {}^{g}\boldsymbol{z}_6 & {}^{g}\boldsymbol{p}_6 \\ 0 & 0 & 0 & 1 \end{bmatrix} \tag{2.23}
$$

$$
= \begin{bmatrix} {}^{b}_{w}\boldsymbol{R}\,{}^{w}_{g}\boldsymbol{R}\begin{bmatrix} {}^{g}\boldsymbol{x}_6 & {}^{g}\boldsymbol{y}_6 & {}^{g}\boldsymbol{z}_6 \end{bmatrix} & {}^{b}\boldsymbol{p}_{w} + {}^{b}_{w}\boldsymbol{R}\,{}^{w}_{g}\boldsymbol{R}\,{}^{g}\boldsymbol{p}_6 \\ \mathbf{0} & 1 \end{bmatrix}. \tag{2.24}
$$

Therefore, for the rotation matrix of ${}^{b}_{6}\boldsymbol{T}$, we only know the first column. Note that we assume the ground frame and the world frame coincide at the same location with only orientation difference and ${}^{w}_{g}\boldsymbol{R} = \mathbb{I}$ if the ground is horizontal.

By observation, we can obtain

$$
\left(\left(p_x - h_x\right)c_1 + \left(p_y + h_y\right)s_1\right)s_2 + \left(p_z + h_z\right)c_2 = 0, \tag{2.25}
$$

$$
\left(r_{11}c_1 + r_{21}s_1\right)s_2 + r_{31}c_2 = 0, \tag{2.26}
$$

and further eliminating θ_2 yields

$$
\underbrace{\left(\left(p_x - h_x\right)r_{31} - \left(p_z + h_z\right)r_{11}\right)}_{k_1}c_1 + \underbrace{\left(\left(p_y + h_y\right)r_{31} - \left(p_z + h_z\right)r_{21}\right)}_{k_2}s_1 = 0 \tag{2.27}
$$

$$
\Rightarrow \theta_1 = \operatorname{atan2}\left(-k_1, k_2\right) \tag{2.28}
$$

Note that θ_1 is nominally around −90 degrees and thus $s_1 < 0$ for our case. With θ_1 solved, θ_2 can be determined to be

$$
\theta_2 = \operatorname{atan2}\left(-p_z - h_z, \left(p_x - h_x\right)c_1 + \left(p_y + h_y\right)s_1\right). \tag{2.29}
$$

Note that θ_2 is nominally around 90 degrees and thus $s_2 > 0$ for our case. Substituting θ_1 and θ_2 into (2.11) and (2.12) we get

$$c_{345} = r_{21}c_1 - r_{11}s_1, \tag{2.30}$$

$$s_{345} = \frac{r_{31}}{s_2}. \tag{2.31}$$

Substituting c_{345} and s_{345} into (2.20) and (2.22) we get

$$a_3c_3 + a_4c_{34} = \frac{p_z + h_z}{-s_2} - a_5c_{345} = k_3, \tag{2.32}$$

$$a_3s_3 + a_4s_{34} = \frac{p_x - h_x - c_1c_2\left(k_3 + a_5c_{345}\right)}{-s_1} - a_5s_{345} - d_2 = k_4. \tag{2.33}$$

Sum of squares yields

$$a_3^2 + a_4^2 + 2a_3a_4c_4 = k_3^2 + k_4^2 \Rightarrow c_4 = \frac{k_3^2 + k_4^2 - a_3^2 - a_4^2}{2a_3a_4} \tag{2.34}$$

$$\Rightarrow \theta_4 = \operatorname{atan2}\left(-\sqrt{1 - c_4^2}, c_4\right). \tag{2.35}$$

Note that θ_4 is nominally non-positive and thus $s_4 \leq 0$ for our case. Substituting θ_4 into (2.32) and (2.33) we obtain

$$\begin{cases} \left(a_3 + a_4c_4\right)c_3 - a_4s_4s_3 = k_3 \\ a_4s_4c_3 + \left(a_3 + a_4c_4\right)s_3 = k_4 \end{cases} \Rightarrow \tag{2.36}$$

$$\theta_3 = \operatorname{atan2}\left(\left(a_3 + a_4c_4\right)k_4 - a_4s_4k_3, \left(a_3 + a_4c_4\right)k_3 + a_4s_4k_4\right), \tag{2.37}$$

since the determinant $\left(a_3 + a_4c_4\right)^2 + \left(a_4s_4\right)^2 = k_3^2 + k_4^2 > 0$. Finally, substituting θ_3 and θ_4 into (2.30) and (2.31) and we can solve for

$$\theta_5 = \operatorname{atan2}\left(s_{345}, c_{345}\right) - \theta_3 - \theta_4. \tag{2.38}$$

To sum up, the inverse kinematics of the right leg is given by

$$\theta_1 = \text{atan2}\left(-k_1, k_2\right), \tag{2.39}$$

$$\theta_2 = \text{atan2}\left(-p_z - h_z, \left(p_x - h_x\right) c_1 + \left(p_y + h_y\right) s_1\right), \tag{2.40}$$

$$\theta_4 = \text{atan2}\left(-\sqrt{1 - c_4^2}, c_4\right), \tag{2.41}$$

$$\theta_3 = \text{atan2}\left(\left(a_3 + a_4 c_4\right) k_4 - a_4 s_4 k_3, \left(a_3 + a_4 c_4\right) k_3 + a_4 s_4 k_4\right), \tag{2.42}$$

$$\theta_5 = \text{atan2}\left(s_{345}, c_{345}\right) - \theta_3 - \theta_4, \tag{2.43}$$

where the variables

$$k_1 = \left(p_x - h_x\right) r_{31} - \left(p_z + h_z\right) r_{11}, \tag{2.44}$$

$$k_2 = \left(p_y + h_y\right) r_{31} - \left(p_z + h_z\right) r_{21}, \tag{2.45}$$

$$c_{345} = r_{21} c_1 - r_{11} s_1, \tag{2.46}$$

$$s_{345} = \frac{r_{31}}{s_2}, \tag{2.47}$$

$$k_3 = \frac{p_z + h_z}{-s_2} - a_5 c_{345}, \tag{2.48}$$

$$k_4 = \frac{p_x - h_x - c_1 c_2 \left(k_3 + a_5 c_{345}\right)}{-s_1} - a_5 s_{345} - d_2, \tag{2.49}$$

$$c_4 = \frac{k_3^2 + k_4^2 - a_3^2 - a_4^2}{2 a_3 a_4}, \tag{2.50}$$

Note that $\theta_1 \sim -\pi/2$, $\theta_2 \sim \pi/2$, $\theta_3 \sim 0$, $\theta_4 \leq 0$, and $\theta_5 \sim 0$.

2.4.3 Kinematic Transformation Between DH Joint Space and Actuator Space

From the previous sections, we know that the two hip actuators are in parallel because of the cable-driven differential pulley system. Also, the knee and ankle actuators are coupled because of two pairs of 4-bar linkage mechanisms. Therefore, to have the correct commands sent to the actuators, we need to find the conversion

of the position, velocity, and torque information between the DH joint space and the actuator space.

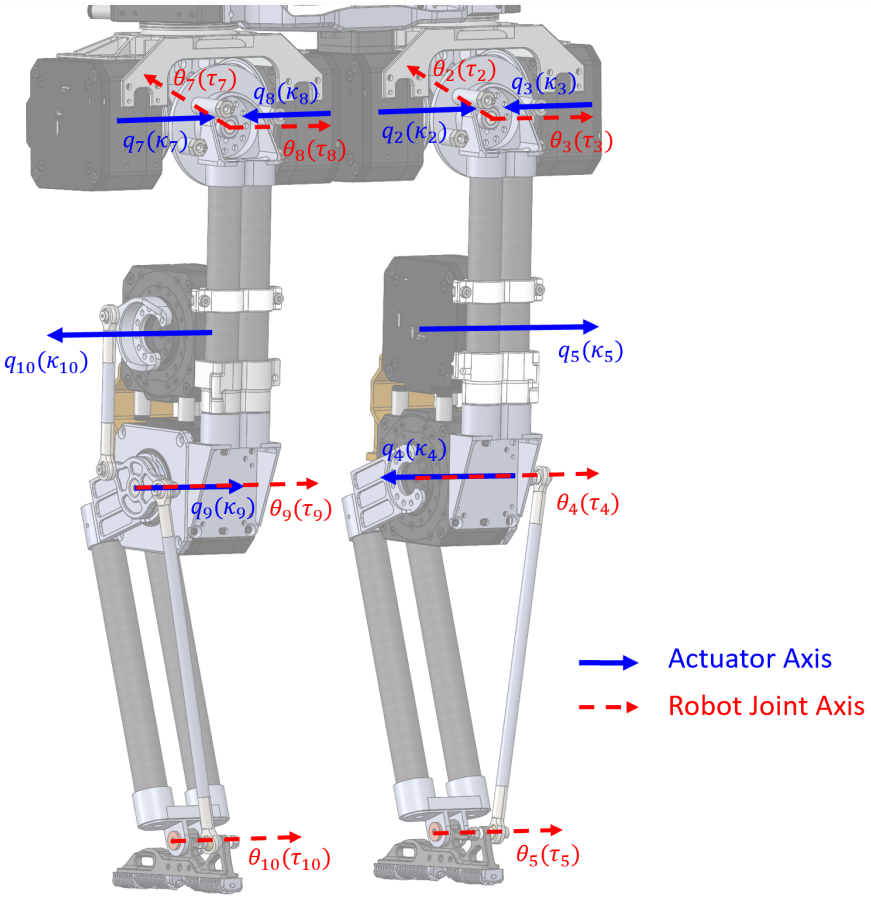

Figure 2.18: Robot joint axis and actuator axis on BRUCE lower body

The robot joint axis and actuator axis distribution are shown in Fig. 2.18. For the right leg, we simply have

$$\begin{cases} \theta_1 = -q_1, \\ \theta_2 = -\dfrac{1}{2}(q_2 + q_3) + \dfrac{\pi}{2}, \\ \theta_3 = \dfrac{1}{2}(q_2 - q_3), \\ \theta_4 = -q_4, \\ \theta_5 = q_4 + q_5. \end{cases} \Rightarrow \begin{cases} q_1 = -\theta_1, \\ q_2 = -\theta_2 + \theta_3 + \dfrac{\pi}{2}, \\ q_3 = -\theta_2 - \theta_3 + \dfrac{\pi}{2}, \\ q_4 = -\theta_4, \\ q_5 = \theta_4 + \theta_5. \end{cases} , \tag{2.51}$$

where θ_i represents BRUCE joint angles, and q_i denotes BEAR actuator with ID

i. Similarly, for the left leg:

$$\begin{cases} \theta_6 = -q_6 \\ \theta_7 = -\dfrac{1}{2}\left(q_7 + q_8\right) + \dfrac{\pi}{2}, \\ \theta_8 = \dfrac{1}{2}\left(q_7 - q_8\right), \\ \theta_9 = q_9, \\ \theta_{10} = -q_9 - q_{10}. \end{cases} \Rightarrow \begin{cases} q_6 = -\theta_6, \\ q_7 = -\theta_7 + \theta_8 + \dfrac{\pi}{2}, \\ q_8 = -\theta_7 - \theta_8 + \dfrac{\pi}{2}, \\ q_9 = \theta_9, \\ q_{10} = -\theta_9 - \theta_{10}. \end{cases} \tag{2.52}$$

The hip configurations for both legs are identical, while the knee and ankle configurations differ. This distinction is due to the actuators being positioned to face each other in the left and right legs, resulting in reversed rotation directions for their rotors. Moreover, the hip roll and pitch joints are coupled due to the cable-driven differential pulley system, as well as the ankle joints because of the 4-bar linkage mechanisms. So their joint angles depend on the output angles of two actuators, as shown in the Eq. (2.51) and Eq. (2.52).

By taking the time derivatives, we can derive the Jacobian matrix.

$$\begin{bmatrix} \dot{\theta}_1 \\ \dot{\theta}_2 \\ \dot{\theta}_3 \\ \dot{\theta}_4 \\ \dot{\theta}_5 \end{bmatrix} = \underbrace{\begin{bmatrix} -1 & 0 & 0 & 0 & 0 \\ 0 & -0.5 & -0.5 & 0 & 0 \\ 0 & 0.5 & -0.5 & 0 & 0 \\ 0 & 0 & 0 & -1 & 0 \\ 0 & 0 & 0 & 1 & 1 \end{bmatrix}}_{\boldsymbol{J}_r} \begin{bmatrix} \dot{q}_1 \\ \dot{q}_2 \\ \dot{q}_3 \\ \dot{q}_4 \\ \dot{q}_5 \end{bmatrix}, \tag{2.53}$$

$$\begin{bmatrix} \dot{\theta}_6 \\ \dot{\theta}_7 \\ \dot{\theta}_8 \\ \dot{\theta}_9 \\ \dot{\theta}_{10} \end{bmatrix} = \underbrace{\begin{bmatrix} -1 & 0 & 0 & 0 & 0 \\ 0 & -0.5 & -0.5 & 0 & 0 \\ 0 & 0.5 & -0.5 & 0 & 0 \\ 0 & 0 & 0 & 1 & 0 \\ 0 & 0 & 0 & -1 & -1 \end{bmatrix}}_{\boldsymbol{J}_l} \begin{bmatrix} \dot{q}_6 \\ \dot{q}_7 \\ \dot{q}_8 \\ \dot{q}_9 \\ \dot{q}_{10} \end{bmatrix}. \tag{2.54}$$

We can easily verify that these two Jacobians are invertible. Finally, taking the transpose of these Jacobians provides the static torque mapping.

$$\begin{bmatrix} \kappa_1 \\ \kappa_2 \\ \kappa_3 \\ \kappa_4 \\ \kappa_5 \end{bmatrix} = \underbrace{\begin{bmatrix} -1 & 0 & 0 & 0 & 0 \\ 0 & -0.5 & 0.5 & 0 & 0 \\ 0 & -0.5 & -0.5 & 0 & 0 \\ 0 & 0 & 0 & -1 & 1 \\ 0 & 0 & 0 & 0 & 1 \end{bmatrix}}_{\boldsymbol{J}_r^\top} \begin{bmatrix} \tau_1 \\ \tau_2 \\ \tau_3 \\ \tau_4 \\ \tau_5 \end{bmatrix}, \tag{2.55}$$

$$\begin{bmatrix} \kappa_6 \\ \kappa_7 \\ \kappa_8 \\ \kappa_9 \\ \kappa_{10} \end{bmatrix} = \underbrace{\begin{bmatrix} -1 & 0 & 0 & 0 & 0 \\ 0 & -0.5 & 0.5 & 0 & 0 \\ 0 & -0.5 & -0.5 & 0 & 0 \\ 0 & 0 & 0 & 1 & -1 \\ 0 & 0 & 0 & 0 & -1 \end{bmatrix}}_{\boldsymbol{J}_l^\top} \begin{bmatrix} \tau_6 \\ \tau_7 \\ \tau_8 \\ \tau_9 \\ \tau_{10} \end{bmatrix}. \tag{2.56}$$

Where κ_i denotes the actuator output torque and τ_i represents the robot joint torque. By knowing the conversion from the robot joints to robot actuators, we can send correct joint velocity, position, and torque commands to the corresponding actuators from the robot joint space commands.

2.4.4 Discussion in Torque Conversion

In the previous section, we obtained the torque mapping relationship from the BRUCE joint torque τ_i to the actuator output torque κ_i. Now it becomes trivial to get torque mapping from the actuators to the BRUCE joints.

$$\begin{bmatrix} \tau_1 \\ \tau_2 \\ \tau_3 \\ \tau_4 \\ \tau_5 \end{bmatrix} = \begin{bmatrix} -1 & 0 & 0 & 0 & 0 \\ 0 & -1 & -1 & 0 & 0 \\ 0 & 1 & -1 & 0 & 0 \\ 0 & 0 & 0 & -1 & 1 \\ 0 & 0 & 0 & 0 & 1 \end{bmatrix} \begin{bmatrix} \kappa_1 \\ \kappa_2 \\ \kappa_3 \\ \kappa_4 \\ \kappa_5 \end{bmatrix}, \tag{2.57}$$

$$\begin{bmatrix} \tau_6 \\ \tau_7 \\ \tau_8 \\ \tau_9 \\ \tau_{10} \end{bmatrix} = \begin{bmatrix} -1 & 0 & 0 & 0 & 0 \\ 0 & -1 & -1 & 0 & 0 \\ 0 & 1 & -1 & 0 & 0 \\ 0 & 0 & 0 & 1 & -1 \\ 0 & 0 & 0 & 0 & -1 \end{bmatrix} \begin{bmatrix} \kappa_6 \\ \kappa_7 \\ \kappa_8 \\ \kappa_9 \\ \kappa_{10} \end{bmatrix}. \tag{2.58}$$

From the torque mapping matrix above, we can see that actuators 2 and 3 work together for the right hip roll and pitch. Similarly, actuators 7 and 8 work together to power the left hip roll and pitch.

$$\begin{cases} \tau_2 = -\kappa_2 - \kappa_3, \\ \tau_3 = \kappa_2 - \kappa_3. \end{cases} \tag{2.59}$$

$$\begin{cases} \tau_7 = -\kappa_7 - \kappa_8, \\ \tau_8 = \kappa_7 - \kappa_8. \end{cases} \tag{2.60}$$

As we can see from Eq. (2.59) and Eq. (2.60), when κ_2 and κ_3 have the same magnitude and direction, τ_3 becomes zero and τ_2 is the summation of the two actuator outputs, which results in the pure hip roll motion of the right leg. Conversely, when κ_2 and κ_3 have the same magnitude but opposite directions, pure hip pitch motion of the right leg is achieved. Thus, the two hip actuators collaborate to enable both hip roll and pitch motions, effectively doubling the available torque for these joints.

In parallel, the torque in the knee joint is coupled due to the 4-bar linkage mechanisms, depending on actuators 4/5, and 9/10.

$$\tau_4 = -\kappa_4 + \kappa_5 \tag{2.61}$$

$$\tau_9 = \kappa_9 - \kappa_{10} \tag{2.62}$$

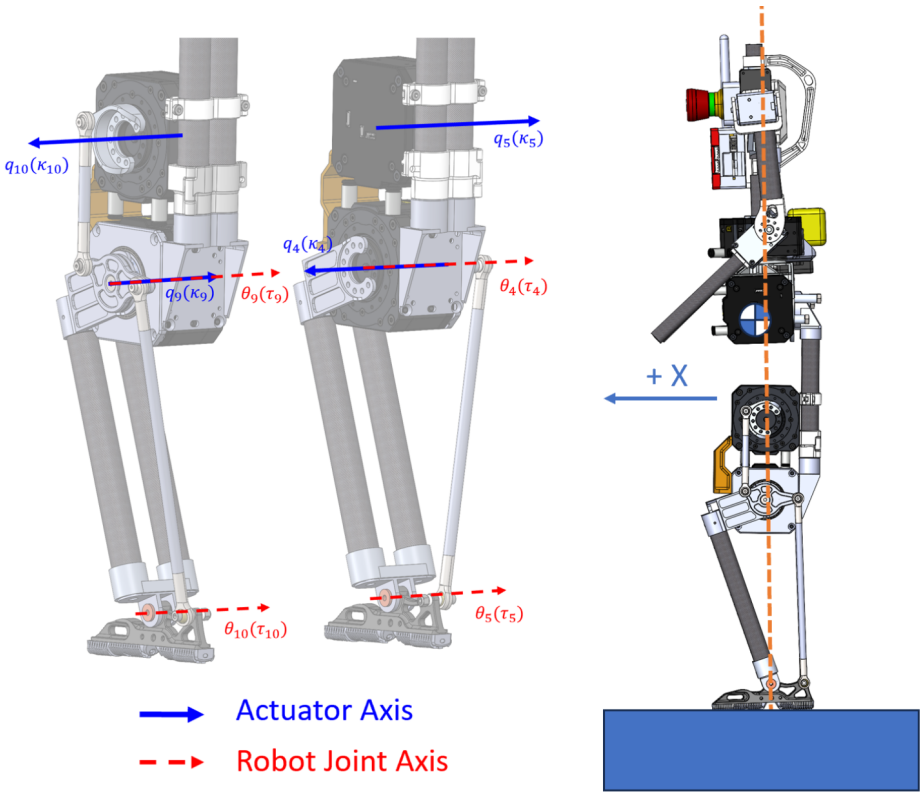

Figure 2.19: BRUCE joint and actuator axis on the knee and ankle joints (left) and the center of mass when BRUCE standing/walking (right)

As we can see from Fig. 2.19, the torque direction of actuators 4, 5, 9, 10 to power the robot knee joint when standing and walking depends on the position of BRUCE's center of mass in the x direction:

$$CoM_x \geq 0 : \begin{cases} \kappa_4 : - \\ \kappa_5 : - \\ \kappa_9 : + \\ \kappa_{10} : + \end{cases}, \qquad CoM_x < 0 : \begin{cases} \kappa_4 : - \\ \kappa_5 : + \\ \kappa_9 : + \\ \kappa_{10} : - \end{cases} \tag{2.63}$$

In most cases, $CoM_x \geq 0$ due to the nature of the robot hardware weight distribution and the fact that the robot is by default to walk in the positive x direction. Thus, referring to Eqs. (2.61) and (2.62), the total coupled torque at the robot's knee joint results from both the knee actuators and the ankle actuators acting with opposite signs. This setup, where the knee and ankle actuators counteract each other, is far from optimal for efficient torque distribution. Since the knee joint is crucial for walking and demands the highest torque of all the joints, this opposing torque setup results in unnecessary torque being wasted to counteract the effect of the ankle actuator.

This is inefficient in terms of both torque distribution and energy use, as a portion of the torque generated by each actuator is effectively wasted in counteracting the other. This internal conflict can cause the knee actuator to overheat, as it must expend additional energy to resist the torque generated by the ankle actuator. Consequently, this not only reduces the robot's payload capacity and limits its operational runtime but also raises the risk of thermal issues that could impact long-term reliability and performance.

Although the coupled knee and ankle actuators in the current configuration does not optimize knee joint torque when $CoM_x \geq 0$, it is noteworthy that when

$CoM_x < 0$, both actuators work together for the knee joint torque. This means to improve the knee torque range and energy efficiency, BRUCE needs to keep its center of mass behind its ankle, which is quite unnatural.

Is there a way to address this issue so that both actuators can work together to enhance the torque at the knee? From Eqs. (2.61) and (2.62), we see that to achieve this cooperation, we need to reverse the torque direction of one actuator. In other words, one of the actuators should rotate in the opposite direction to effectively actuate the joint. This can be achieved through one of two potential approaches: either reversing the rotation direction of the knee actuator or altering the rotation direction of the ankle actuator.

Reversing the rotation direction of the knee actuator while maintaining the same knee movement is physically impossible unless an additional layer of transmission mechanism is introduced, which would significantly increase the complexity of the leg design. Alternatively, we can change the rotation direction of the ankle actuator by implementing a reversed 4-bar linkage mechanism. This approach alters the ankle actuator's rotation direction without requiring further mechanical modifications.

The detailed implementation of the reversed 4-bar linkage mechanism for the ankle joint will be discussed in the next chapter.

2.5 Testing and Results

In this section, we assess the overall performance of BRUCE through various tests, including basic control verification with push recovery and center of mass (CoM) tracking. Additionally, we conduct dynamic bipedal locomotion tests [4] and dynamic jumping tests [5] to further validate BRUCE's dynamic capabilities.

2.5.1 Control Verification

To control BRUCE, the convex MHPC framework was implemented and the performance was evaluated in different scenarios including push recovery and CoM tracking. Note that for all the experiments, the desired torque commands solved by MHPC at the first time step were directly sent to the robot [3].

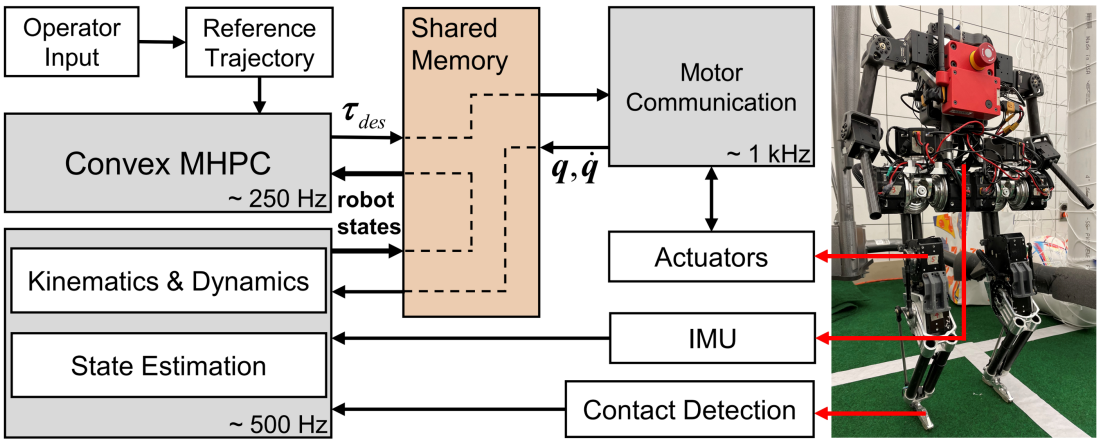

Figure 2.20: BRUCE software architecture block diagram [3]

The computation time of MHPC is influenced by the robot's degrees of freedom, the number of contact vertices N_c, and the number of time steps into the future N_s. For BRUCE, which has 10 DoFs, 2-point contacts per foot ($N_c = 4$), and 5 time steps for a simplified model ($N_s = 5$ with $\Delta_t = 0.1$ s), the processing time including problem formulation allows a frequency of 250 Hz when using the off-the-shelf QP solver OSQP [53] on a laptop equipped with an AMD Ryzen 5 4500U CPU at 2.1 GHz. This frequency is sufficient for real-time feedback control.

To begin, we evaluated the balancing capability of MHPC, given the inherent instability of bipedal systems. In this test, BRUCE was tasked with maintaining its nominal standing posture, with all references set to constant nominal values. As illustrated in Fig. 2.21, an impulsive force was applied in the positive x-direction, followed by another in the opposite direction. The pushes were strong enough to accelerate the robot's center of mass (CoM) to approximately 0.1 m/s. Neverthe-

less, the robot successfully recovered within two seconds. However, we observed a steady-state error, likely due to model inaccuracies. Additionally, the implementation of MHPC on BRUCE enabled very compliant responses, facilitated by its proprioceptive actuation.

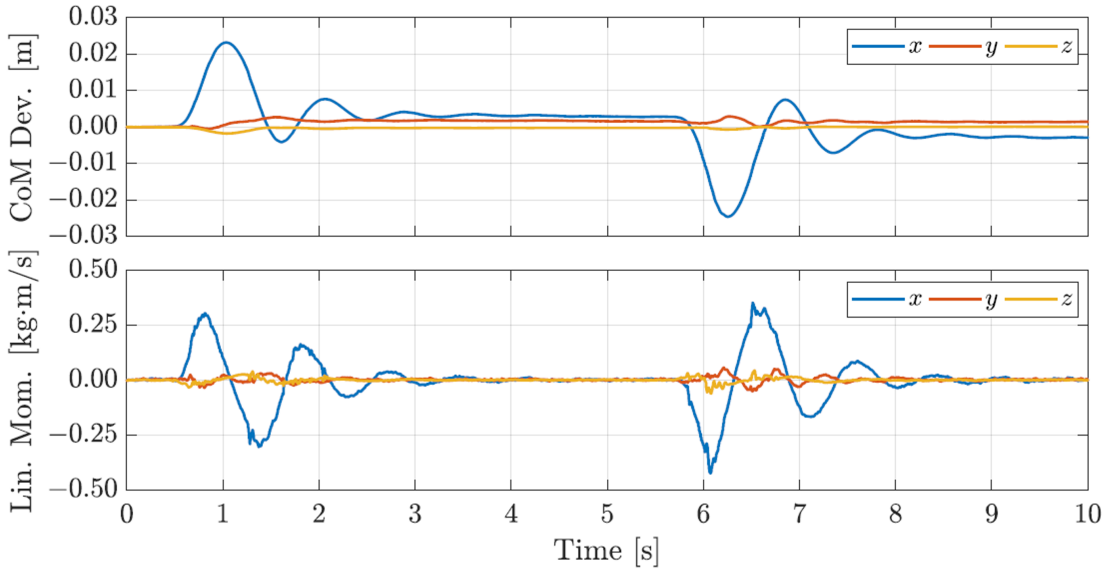

Figure 2.21: Experimental results of CoM deviation and linear momentum in the x direction for the push recovery test [3]

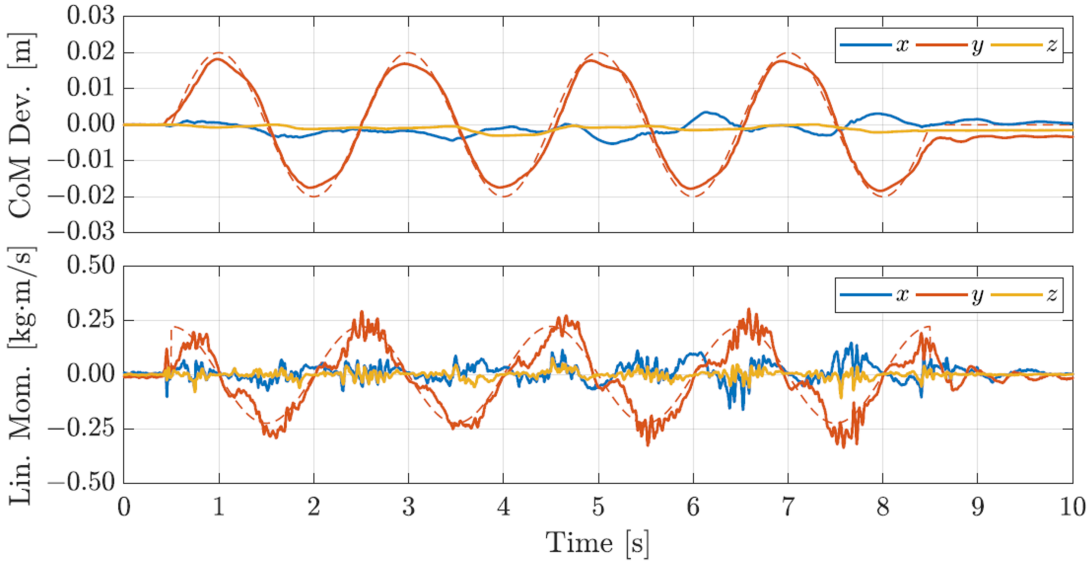

Figure 2.22: Experimental results of CoM deviation and linear momentum in the y direction for the CoM tracking test (the dashed lines are the references) [3]

In a subsequent experiment, BRUCE was commanded to perform a left-to-right shifting motion. All reference values were kept consistent with the push recovery test, except for the CoM, which tracked a sinusoidal trajectory at 0.5 Hz in the y-direction, as depicted in Fig. 2.22. The robot demonstrated anticipatory actions, minimizing overall tracking error by planning for the present while considering future time slots.

2.5.2 Dynamic Bipedal Locomotion

Designing a dynamic walking controller for bipedal robots is a challenging task due to the hybrid, nonlinear, and highly constrained nature of these systems. A widely used solution is a two-layer approach combining high-level footstep planning with low-level whole-body control. While effective, this method often lacks comprehensive implementation details. Leveraging the BRUCE platform, an in-depth application of this framework has been developed to enable robust dynamic walking, marking the first successful implementation of its kind.

The high-level planner is based on the Divergent Component of Motion (DCM), and optimizes footstep placement and timing to enhance stability and robustness. Meanwhile, the low-level controller incorporates full-body dynamics to ensure planned foot contact while managing additional objectives like maintaining the center of mass height and stabilizing torso orientation. Both levels are structured as compact quadratic programs, allowing for efficient, real-time optimal control solutions. Experiments in simulation and on hardware demonstrate the system's ability to handle disturbances such as external pushes and uneven terrain effectively. [4].

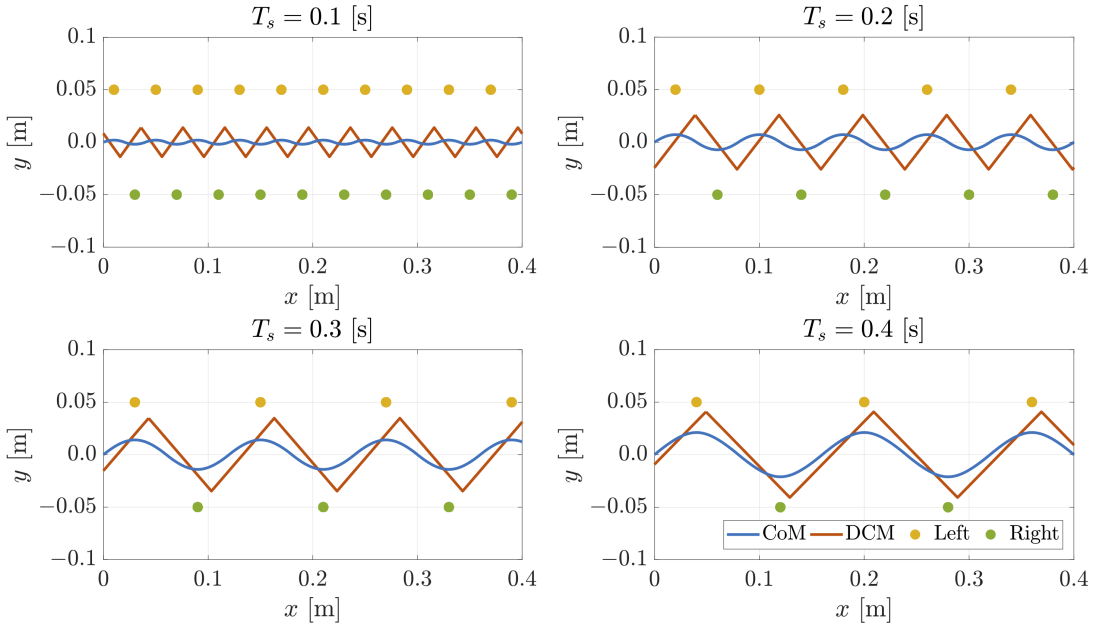

Figure 2.23: Nominal gait patterns with different step durations when BRUCE moves forward in the positive x direction while maintaining a constant CoM speed of 0.1 m/s, a consistent CoM height of 0.3 m, and a fixed step width of 0.1 m. [4].

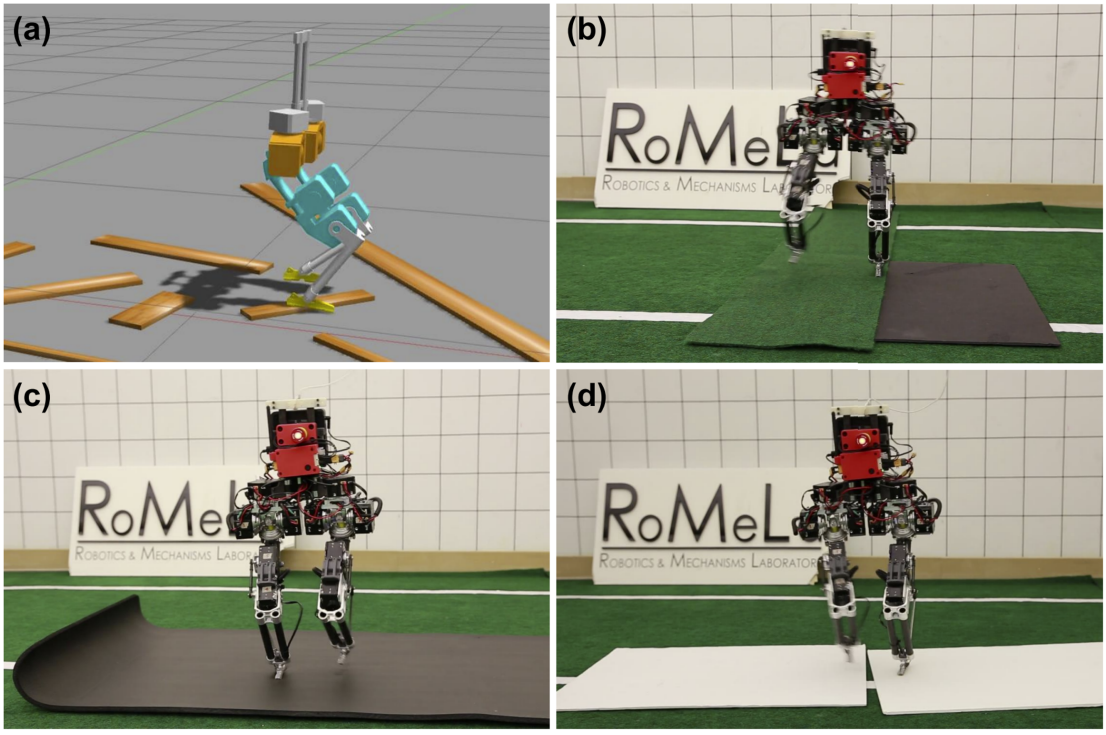

Figure 2.24: BRUCE walking on irregular terrains. (a) Uneven terrain in simulation. (b) Height variation. (c) Soft terrain. (d) Sliding terrain [4].

2.5.3 Dynamic Jumping

Developing dynamic jumping motions for bipedal robots is particularly challenging due to the need to manage both the flight phase and the high-impact landings. Unlike quadrupedal or multi-legged robots, bipedal systems require more precise control strategies because of their smaller support polygon. To facilitate research on bipedal jumping and evaluate BRUCE's dynamic capabilities and robustness, we introduced a novel heuristic landing planner. This planner uses real-time momentum feedback during the flight phase to adjust landing positions, minimizing the effects of tracking errors and external disturbances during landings.

By combining this landing planner with a modified kino-dynamic motion planner that incorporates centroidal momentum and a low-level controller leveraging whole-body dynamics for hierarchical task prioritization, we developed a robust jumping control framework. This framework has been successfully implemented on BRUCE, showcasing its suitability for exploring the dynamic motions critical in humanoid robotics research [5].

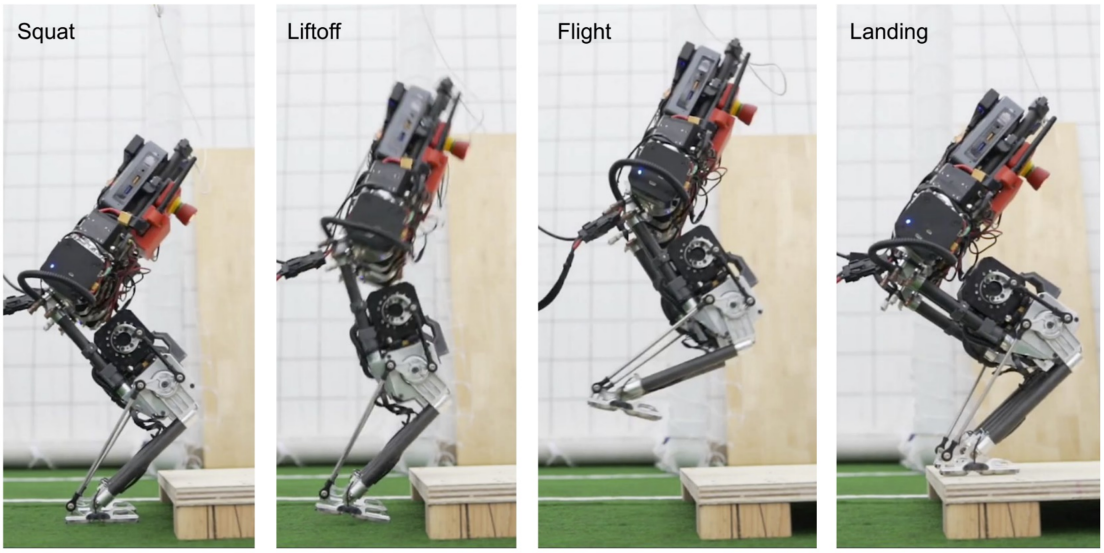

Figure 2.25: BRUCE performing a step jump onto a 5 cm platform [5].

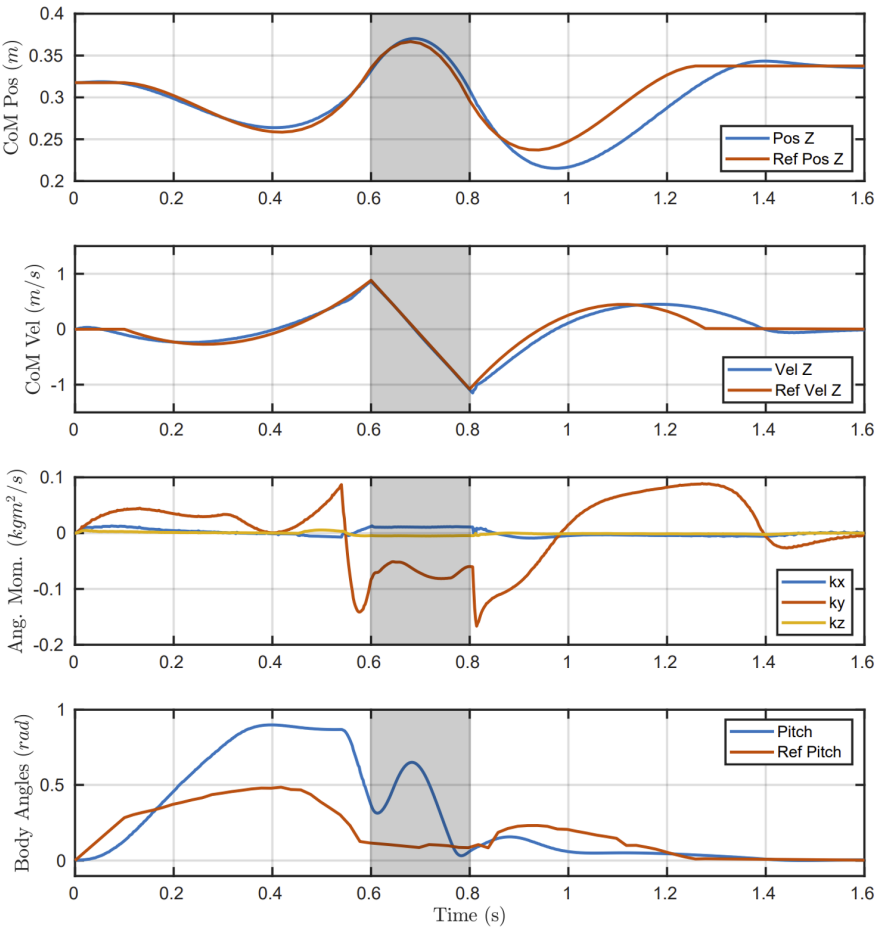

Figure 2.26: In-situ jumping trajectory for BRUCE. Shaded areas represent the flight phase [5].

CHAPTER 3

BRUCE Refresh

Figure 3.1: BRUCE Refresh CAD

3.1 Introduction

The initial development of BRUCE was finalized in early 2021, setting the stage for extensive testing to evaluate the platform's performance in executing highly dynamic tasks such as walking and jumping. Over nearly three years of continuous experimentation, BRUCE's hardware has faced substantial wear and tear, emphasizing the necessity for a redesigned and upgraded version. This refresh build aims not only to address durability concerns but also to prepare BRUCE for its envisioned role as an open-source platform available to the wider humanoid robotics research community. Achieving this goal requires improvements to both the hardware's stability and its ease of use, ensuring that researchers can reliably operate and experiment with BRUCE.

The upgraded design focuses on reorganizing and streamlining hardware components to create a more intuitive setup that enhances user experience while maintaining reliability. Feedback from daily testing sessions has been instrumental in guiding these updates, including modifications on the tibia and foot to improve the robustness of BRUCE, as well as incorporating mechanical advantages to prioritize torque at the knee joint for better supporting dynamic movements. These modifications aim to extend BRUCE's operational lifespan and efficiency, enabling longer walking sessions and more robust performance in demanding scenarios. By prioritizing these enhancements, BRUCE is being refined to better serve the needs of researchers as a dynamic locomotion platform, and contribute to the advancement of humanoid robotics.

3.2 Tibia Modification

During BRUCE's walking tests, we observed that the ankle joints of the two legs often collided when the foot placement was close. These collisions introduced disturbances to the system and compromised locomotion stability, even though BRUCE's proprioceptive actuators mitigated some of the effects in unstructured environments.

To address this issue, the tibia width of BRUCE was reduced from 46.5 mm to 31.5 mm. Corresponding modifications were made to the aluminum components in the tibia to accommodate this narrower design. The new tibia with a narrower form factor significantly increases the range of motion for foot placement, reducing the likelihood of ankle collisions during stepping. As a result, the walking stability of BRUCE has been notably improved, allowing for more reliable performance during close-step scenarios.

(a) Tibia Ver. 1 (b) Tibia Ver. 2

Figure 3.2: Comparison of the tibia designs

3.3 Ankle Modification

As discussed in Section 2.4.4, when BRUCE is standing or walking with $CoM_x \geq 0$, the knee and ankle actuators often oppose each other when generating knee torque. This not only reduces energy efficiency but also leads to knee actuator overheating, making it necessary to modify the ankle transmission to address this issue.

3.3.1 Inspiration

Research on joint torque analysis from various studies [9, 54, 55] highlights the critical role of the knee joint in enabling humans and humanoid robots to stand and walk effectively. To enhance BRUCE's dynamic locomotion performance, it is essential to prioritize the torque capacity of the knee joint rather than allowing the knee and ankle actuators to work against each other, which wastes energy.

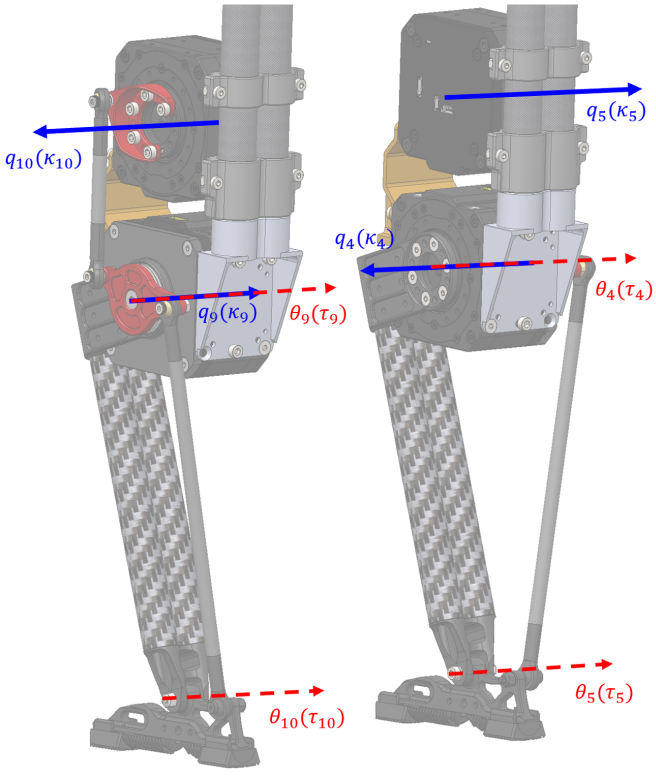

Figure 3.3: BRUCE joint and actuator axis on the knee and ankle joints

From the conclusion of Section 2.4.4 and referring to the axis distribution shown in Fig. 3.3 , in order to make the knee and ankle actuators work together on the robot knee torque, we need to change the rotation of the ankle actuator so that the torque output from the ankle actuators are in the opposite direction of the knee actuator torque output. Consequently, the total knee torque becomes the sum of the torque outputs from both actuators:

$$\begin{cases} \tau_4 = -\kappa_4 + \kappa_5, \\ \tau_5 = \kappa_5, \\ \tau_9 = \kappa_9 - \kappa_{10}, \\ \tau_{10} = -\kappa_{10}. \end{cases} \Rightarrow \begin{cases} \tau_4 = -\kappa_4 + \kappa_5, \\ \tau_5 = -\kappa_5, \\ \tau_9 = \kappa_9 - \kappa_{10}, \\ \tau_{10} = +\kappa_{10}. \end{cases} \tag{3.1}$$

$$\begin{cases} \theta_4 = -q_4, \\ \theta_5 = q_4 + q_5, \\ \theta_9 = q_9, \\ \theta_{10} = -q_9 - q_{10}. \end{cases} \Rightarrow \begin{cases} \theta_4 = -q_4, \\ \theta_5 = -q_4 - q_5, \\ \theta_9 = q_9, \\ \theta_{10} = +q_9 + q_{10}. \end{cases} \tag{3.2}$$

When BRUCE is standing or walking with $CoM_x \geq 0$:

$$\begin{aligned} \kappa_4 &: -, & \kappa_5 &: +, \\ \kappa_9 &: +, & \kappa_{10} &: -. \end{aligned} \tag{3.3}$$

By implementing the modified ankle torque transmission mechanism, the torque range of BRUCE's knee joint can potentially be doubled. This improvement leverages joint coupling to allow the knee and ankle actuators to work together, which significantly enhances the robot's dynamic locomotion capabilities.

3.3.2 Reversed Ankle

To alternate the ankle actuator's rotation direction and achieve the desired change in the robot joint torque and angles illustrated in Eq. (3.2) and Eq. (3.1), a reversed 4-bar mechanism is used to replace the original parallelogram 4-bar linkage mechanism, as shown in Fig. 3.4.

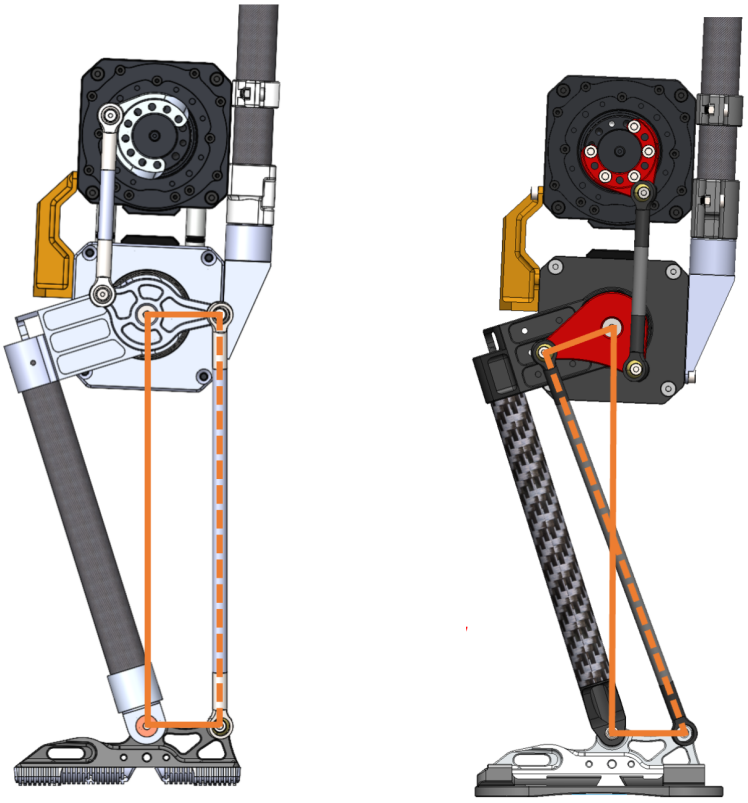

(a) Parallel 4-bar ankle (b) Reversed 4-bar ankle

Figure 3.4: Comparison of the ankle mechanism designs

This modified 4-bar mechanism successfully reverses the ankle actuator's torque and rotation direction while preserving the intended mechanical functionality.

$$\begin{aligned} \kappa_5 &\Rightarrow -\kappa_5, \\ -\kappa_{10} &\Rightarrow +\kappa_{10}, \\ q_5 &\Rightarrow -q_5, \\ -q_{10} &\Rightarrow +q_{10}. \end{aligned} \tag{3.4}$$

Also, the knee and ankle rotation coupling changes due to the usage of the reversed 4-bar mechanism:

$$\begin{aligned} q_4 &\Rightarrow -q_4, \\ -q_9 &\Rightarrow +q_9. \end{aligned} \tag{3.5}$$

However, this design change introduces a drawback: transmission nonlinearity. As shown in Fig. 3.5, there is now a nonlinear relationship between the actuator input and the resulting robot ankle joint output. To address this, a polynomial fitting curve Eq. (3.6) is employed to convert the position commands sent to the actuator, ensuring they accurately produce the desired ankle joint positions.

$$\theta = -0.000008q^3 + 0.0049q^2 - 1.6292q + 181.65 \tag{3.6}$$

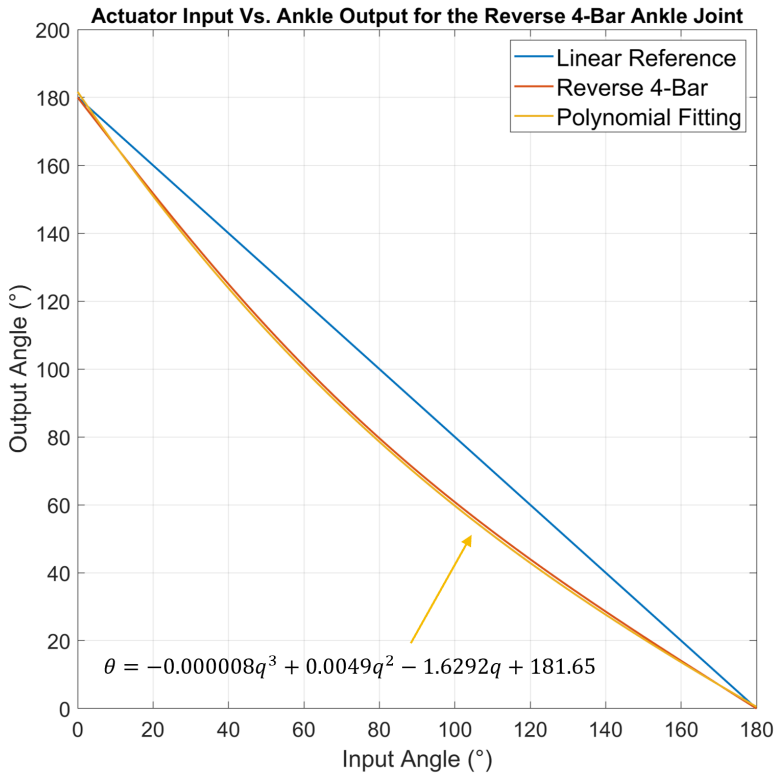

Figure 3.5: Ankle joint nonlinearity and the polynomial fitting

3.4 Foot Modification

The transition from the first version to the second version of BRUCE's foot design introduces several critical improvements aiming at addressing performance limitations and enhancing the robot's stability during dynamic locomotion. The original foot design suffers from low reliability and insufficient friction, which reduces its effectiveness in maintaining steady footsteps, particularly on low-traction surfaces. These shortcomings pose challenges to BRUCE's locomotion stability, making it necessary to refine the design for more reliable performance.

In the second version of the foot design, several upgrades are implemented to overcome these limitations. An extra foot pad is introduced, designed to be flexible in the sagittal plane while providing better adaptability during foot contact and push-off phases. This modification also increases the overall support area, enhancing stability during walking. Furthermore, the additional layer of table tennis rubber to the foot pad significantly improves friction, ensuring better grip across a variety of surfaces. These changes not only resolve the issues observed in the previous design but also improve BRUCE's overall durability and robustness in unstructured environments, ensuring more stable locomotion.

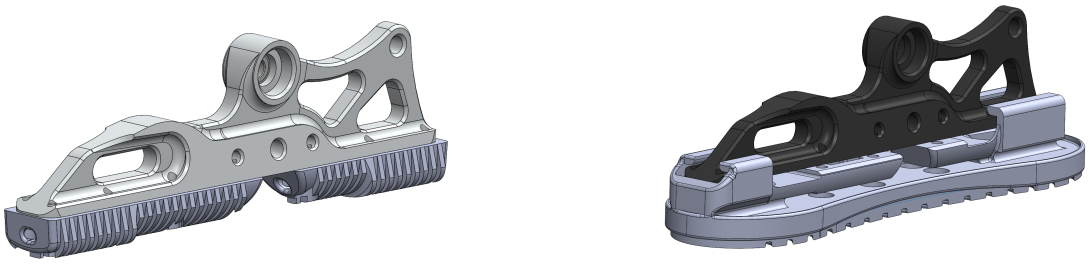

(a) Foot design Ver. 1

(b) Foot design Ver. 2

Figure 3.6: Comparison of the foot designs

3.5 Upper Body Modification

The primary goal of the upper body modifications for BRUCE was to create a clean, robust, and well-organized hardware setup in preparation for its transition to an open-platform system. In the updated BRUCE Refresh design, a durable plastic cover has been introduced to enclose all upper body components, offering improved protection against external damage. By reducing the exposure of electrical components, the likelihood of malfunctions or breakdowns is significantly minimized.

Additionally, a redesigned wire management system has been implemented, providing a major improvement in both functionality and appearance. This new solution not only enhances the overall aesthetics of the robot but also reduces the risk of wiring-related issues, ensuring a more reliable and user-friendly platform for research and development.

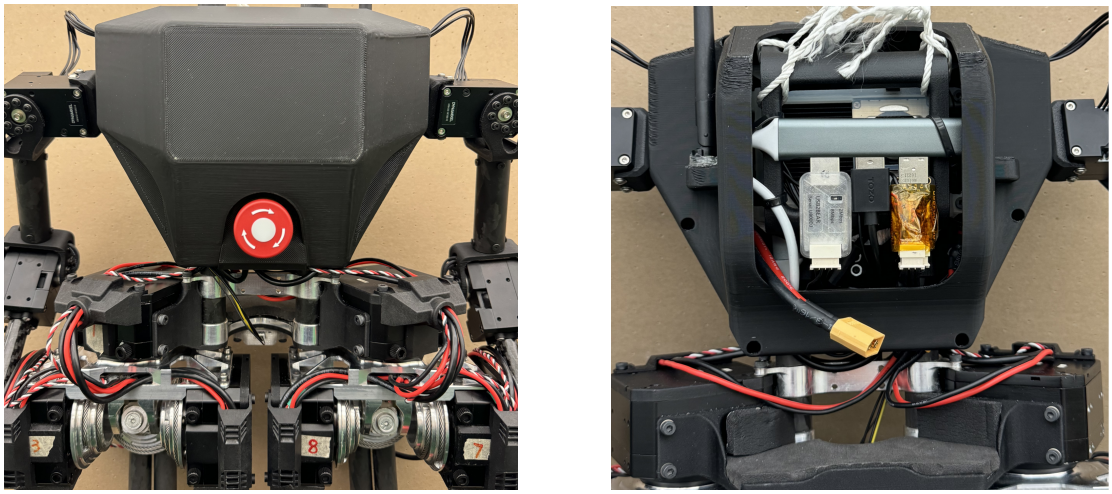

(a) Front view (b) back view

Figure 3.7: BRUCE refresh upper body hardware

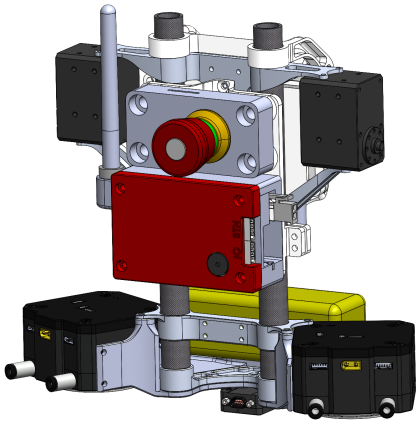

(a) BRUCE upper body

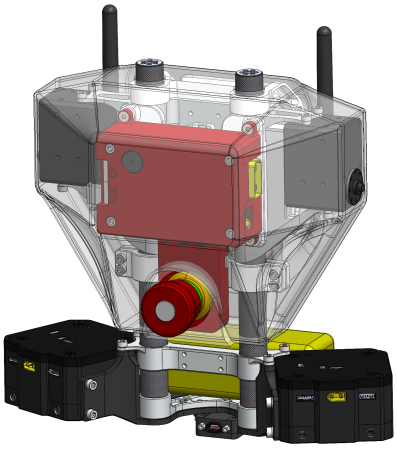

(b) BRUCE Refresh upper body

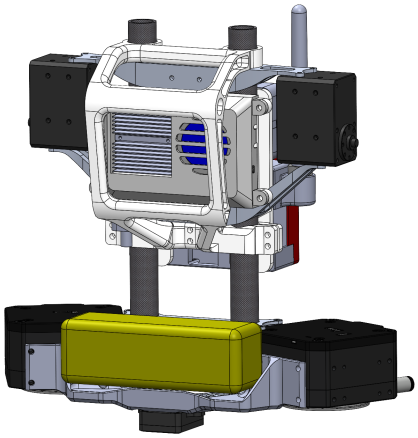

(c) BRUCE upper body

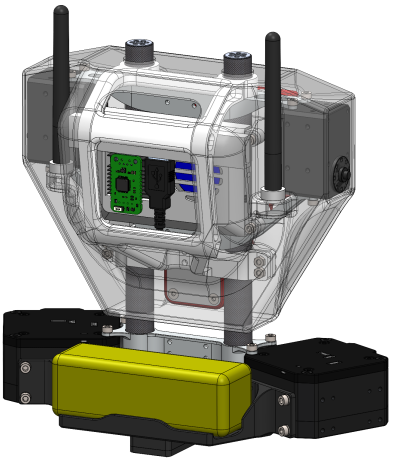

(d) BRUCE Refresh upper body

Figure 3.8: Comparison of the upper body CAD designs

3.6 BRUCE Refresh

The BRUCE Refresh miniature humanoid platform designed for dynamic locomotion is showcased in Fig. 3.9 and Fig. 3.10, alongside a comparison to the earlier BRUCE prototype. Overall, BRUCE Refresh demonstrates significant advancements in mechanical design and presents a sleeker, more refined hardware appearance.

As detailed in Fig. 3.11, the total production cost for BRUCE Refresh is approximately 6,000 USD, comparable to the price of a single hip actuator from ARTEMIS. This cost-efficient design makes the platform more accessible to researchers, promoting broader adoption and innovation in humanoid robotics.

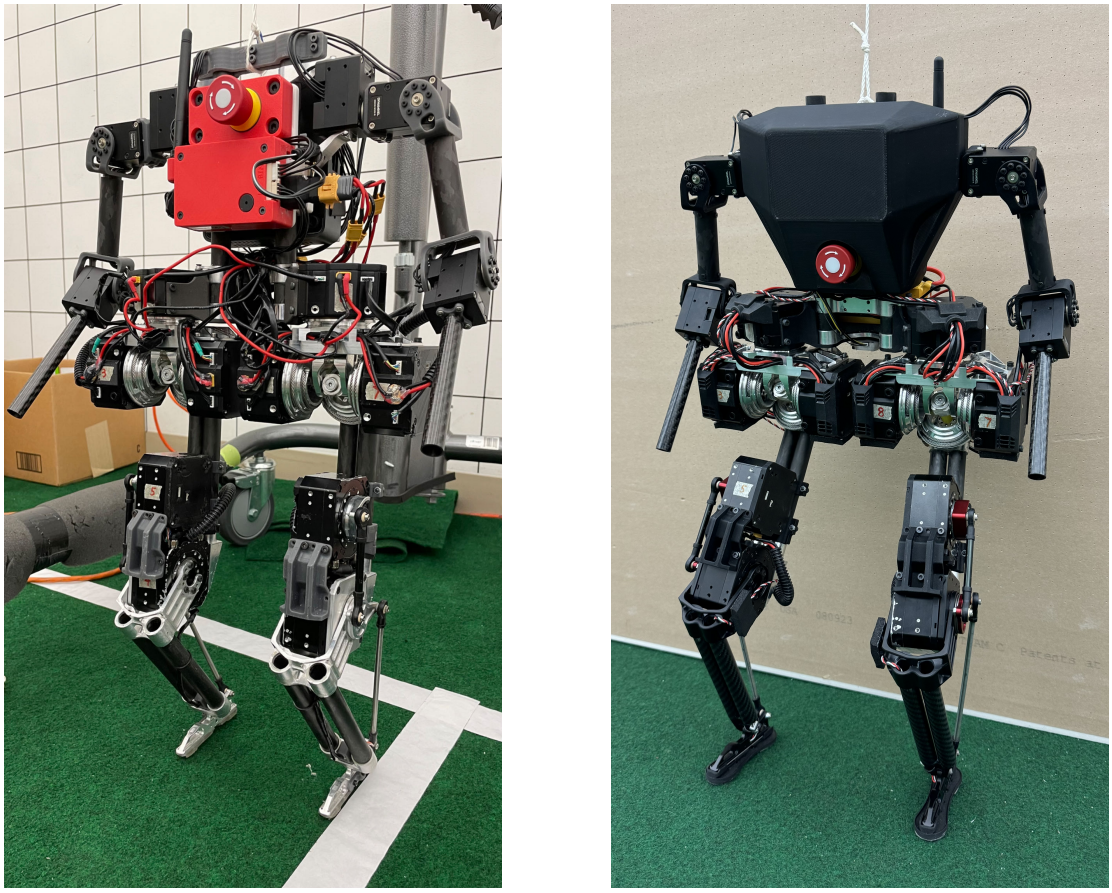

(a) BRUCE (b) BRUCE Refresh

Figure 3.9: Front view comparison of BRUCE Vs. BRUCE Refresh

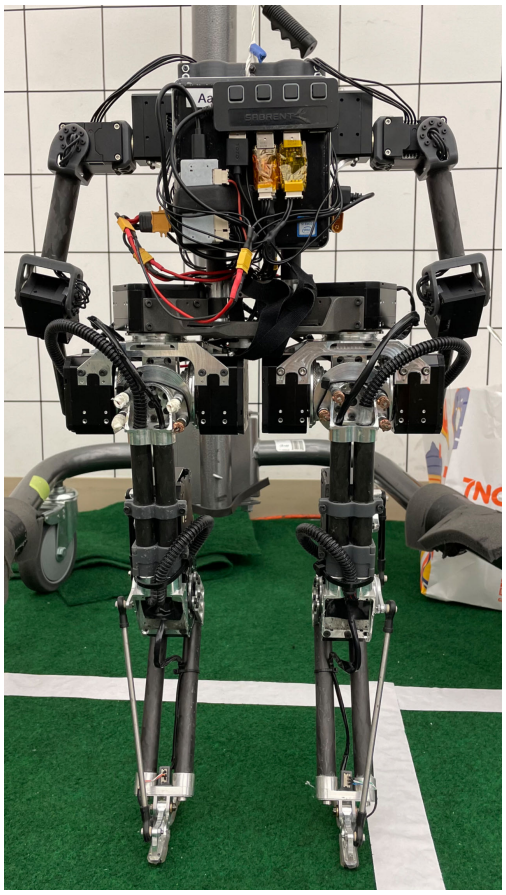

(a) BRUCE

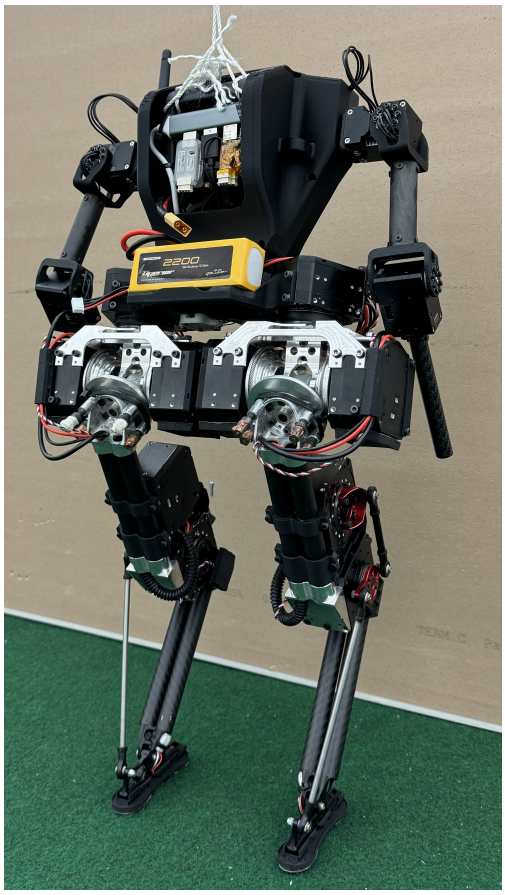

(b) BRUCE Refresh

Figure 3.10: Back view comparison of BRUCE Vs. BRUCE Refresh

Part	QTY	Vender	Unit Price	Total
Koala BEAR Actuator	10	Westwood Robotics	400	4000
USB2BEAR	2	Westwood Robotics	35	70
DYNAMIXEL XL430 Actuator	6	Robotis	49.9	299.4
Computer (Khadas Edge 2)	1	Khadas	249	249
IMU (ISM330DHCX 6-DOF)	1	Adafruit	19.95	19.95
Battery (Liperior 2200mAh 4S)	1	RCBattery	22.99	22.99
Wireless Estop	1	RoMeLa	120	120
3D printed parts	1	RoMeLa	50	50
Machined parts set	1	McMaster/ Westwood Robotics	700	700
Carbon fiber tubes	12	Rock West Composites	10	120
Bearings	1	McMaster/ Westwood Robotics	300	300
Fasteners	1	McMasters	50	50
			Grand Total (USD)	6001.34

Figure 3.11: BRUCE bill of materials

3.7 Design Verification

To assess the effectiveness of the reversed 4-bar linkage mechanism in reducing knee actuator load and improving energy efficiency, a series of benchmark tests were conducted, including standing, payload, walking, and jumping scenarios. Each test compared BRUCE's performance with the original parallel 4-bar linkage ankle and the modified reversed 4-bar linkage ankle configurations.

3.7.1 Standing Still

In the standing test, BRUCE remained stationary for 15 minutes with the whole-body controller active. Key metrics such as output torque and winding temperature of the knee and ankle actuators were recorded. The results were expected to show lower torque and temperature with the modified design, validating the benefits of the reversed 4-bar linkage mechanism.

As shown in Fig. 3.12, Fig. 3.13, and the summarized results in Table 3.1, the experimental data aligns well with the theoretical predictions. By implementing the reversed 4-bar linkage mechanism on the ankle joint, the output torque on the knee and ankle actuators decreased by over 30% and 50%, respectively. Additionally, the winding temperatures of the knee and ankle actuators dropped by 18.7 °C and 25.5 °C, significantly mitigating the actuator overheating issue.

Table 3.1: Results for Benchmark Test 1: Standing Still

Parameter	**Parallel Ankle**	**Reversed Ankle**	**Changes**
κ_4	-2.75 [Nm]	-1.79 [Nm]	$\downarrow$ 34.9%
κ_5	-0.73 [Nm]	0.32 [Nm]	$\downarrow$ 56.2%
κ_9	1.82 [Nm]	1.07 [Nm]	$\downarrow$ 41.2%
κ_{10}	0.75 [Nm]	-0.30 [Nm]	$\downarrow$ 60.0%
T_4	71.5 [°C]	52.8 [°C]	$\downarrow$ 18.7[°C]
T_9	67.5 [°C]	42.0 [°C]	$\downarrow$ 25.5[°C]

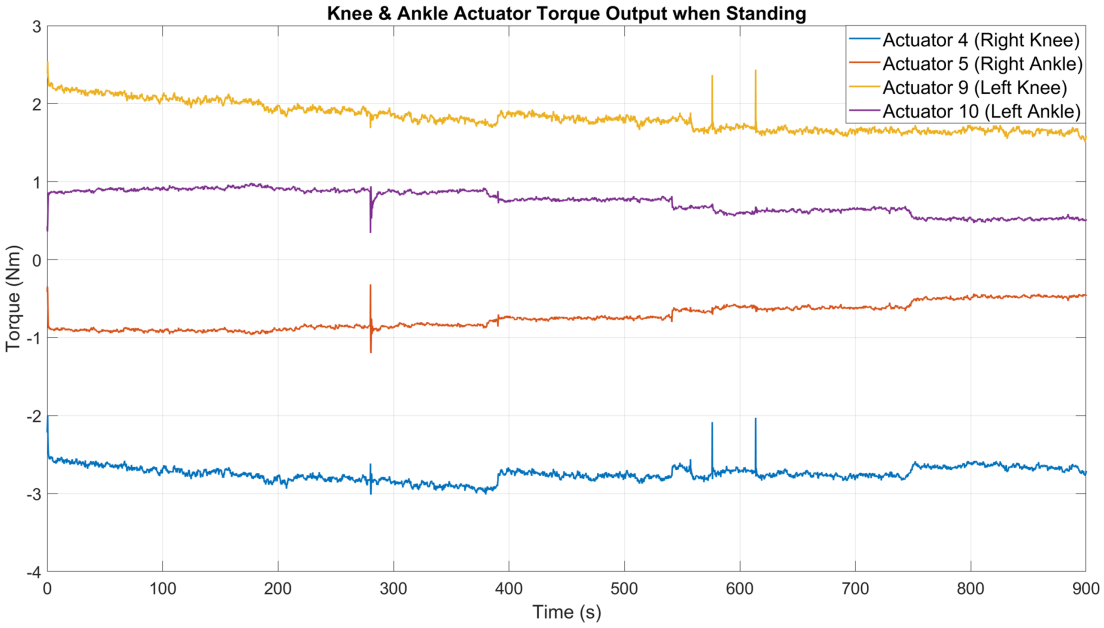

(a)

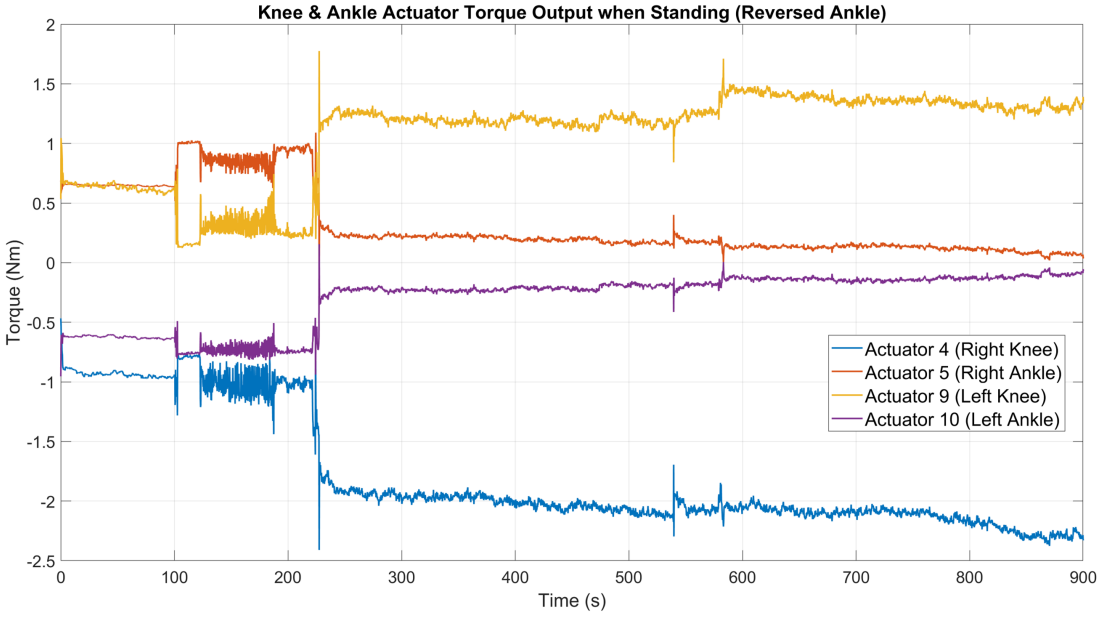

(b)

Figure 3.12: The output torque for the knee and ankle actuators during Benchmark Test 1: Standing Still.

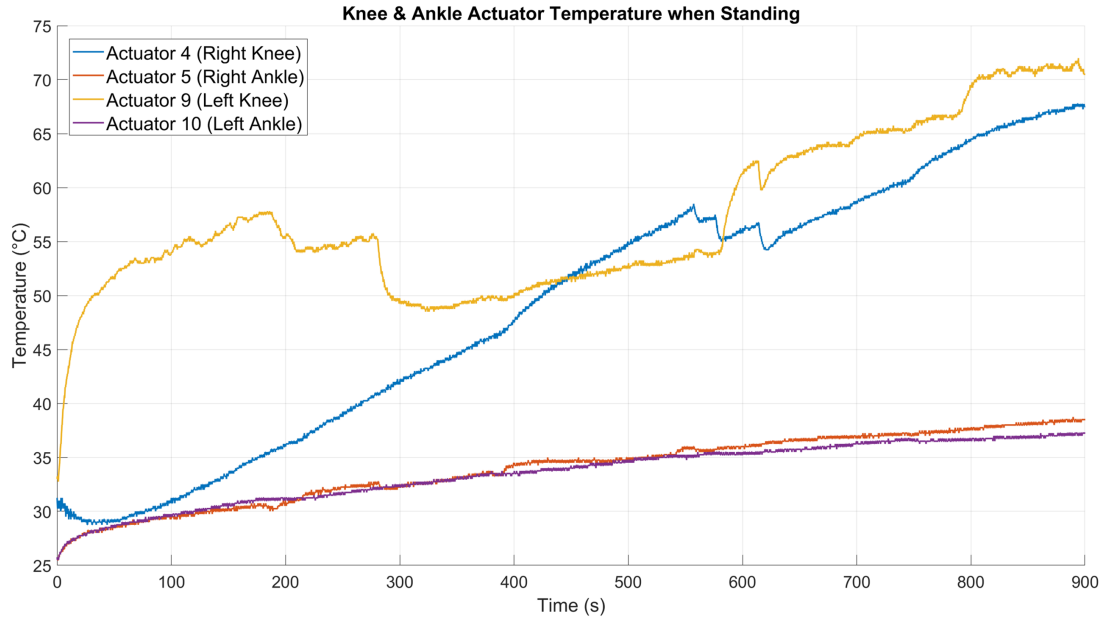

(a)

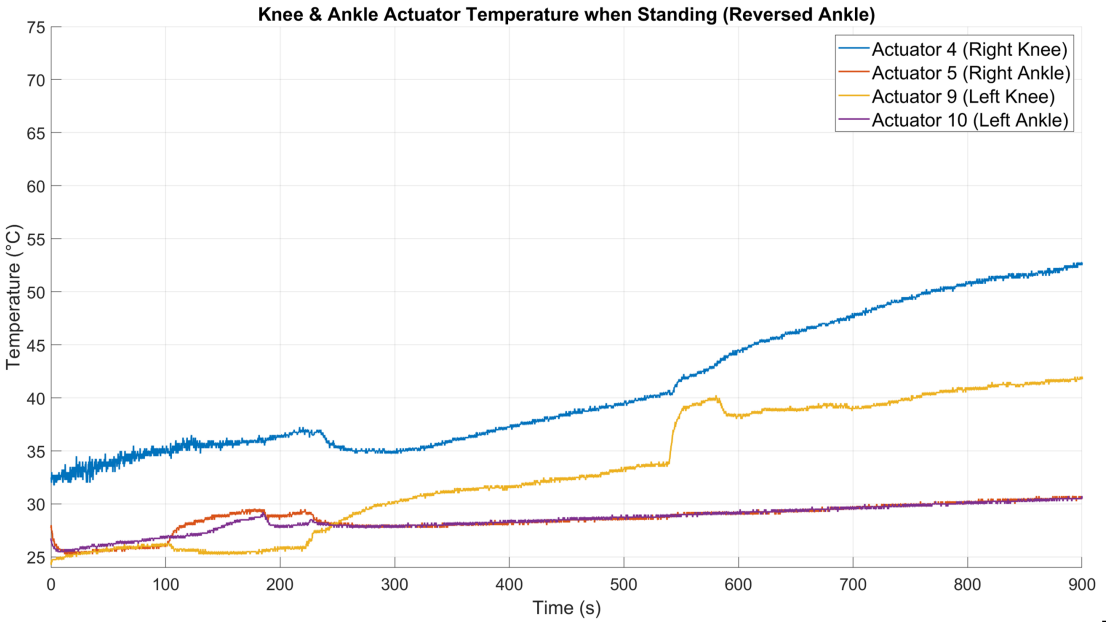

(b)

Figure 3.13: The winding temperature for the knee and ankle actuators during Benchmark Test 1: Standing Still.

3.7.2 Standing with Payload

The second benchmark test of standing with payload builds on the previous standing still test. BRUCE remains stationary with the whole-body controller active, while a 1 kg weight is added to its upper body, as shown in Fig. 3.14. The output torque of the knee and ankle actuators is recorded during the test. To prevent overheating, the weight is removed after approximately 30 seconds.

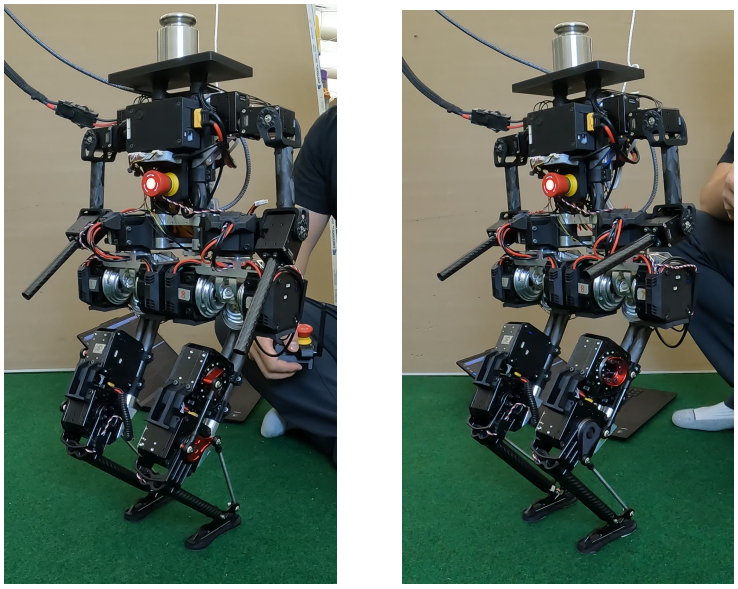

(a) Ankle with parallel 4-bar (b) Ankle with reversed 4-bar

Figure 3.14: The setup for Benchmark Test 2: Standing with Payload.

As shown in Fig. 3.15 and summarized in Table 3.2, the reversed 4-bar linkage mechanism significantly reduced torque on the knee and ankle actuators by 34.4% to 60.3%. This modification enables the actuators to work together more efficiently, allowing BRUCE to handle greater payloads.

Table 3.2: Results for Benchmark Test 2: Standing with Payload

Parameter	**Parallel Ankle**	**Reversed Ankle**	**Changes**
κ_4	-3.15 [Nm]	-1.66 [Nm]	$\downarrow$ 47.3%
κ_5	-0.90 [Nm]	0.59 [Nm]	$\downarrow$ 34.4%
κ_9	2.47 [Nm]	0.98 [Nm]	$\downarrow$ 60.3%
κ_{10}	0.86 [Nm]	-0.51 [Nm]	$\downarrow$ 40.7%

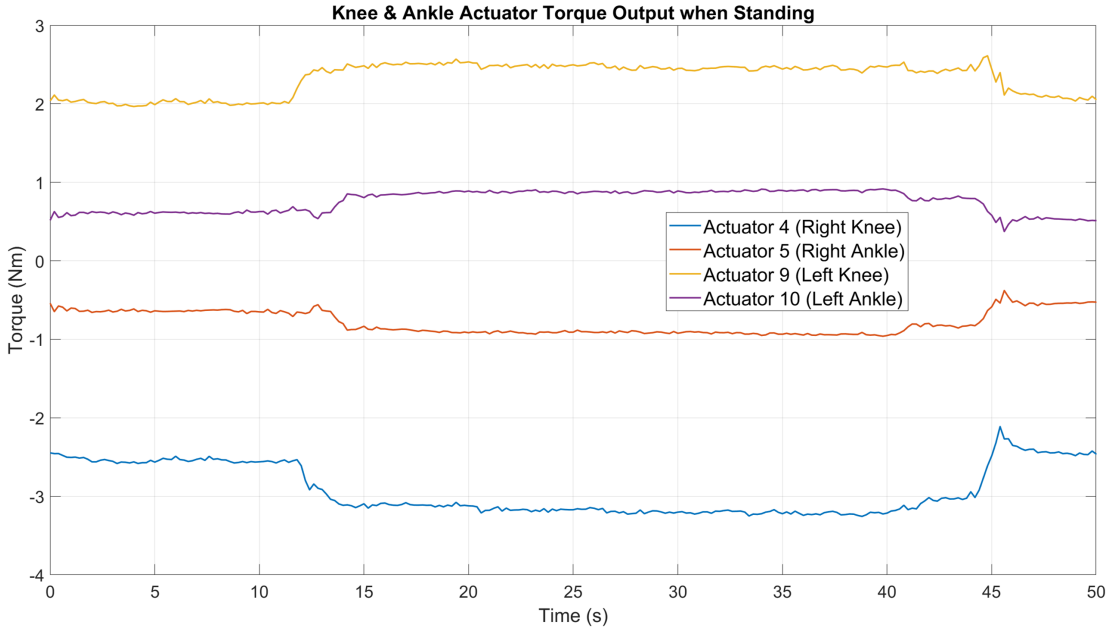

(a)

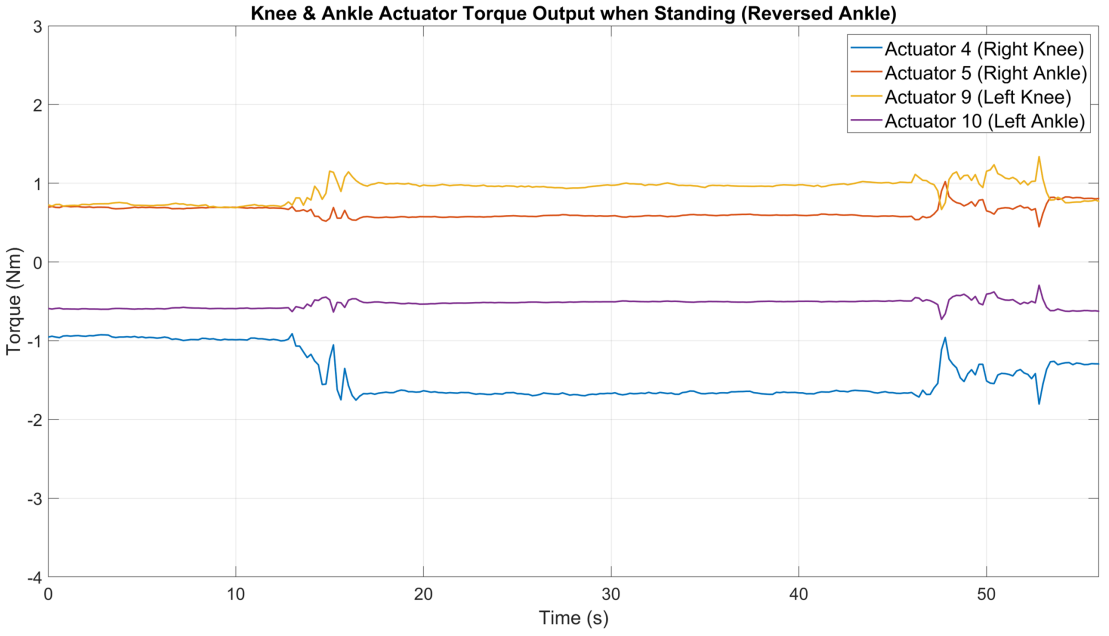

(b)

Figure 3.15: The output torque for the knee and ankle actuators during Benchmark Test 2: Standing with Payload.

3.7.3 Walking

To assess the performance of the modified reversed ankle joint in dynamic locomotion, a walking test was conducted on BRUCE using both the parallel 4-bar and reversed 4-bar ankle configurations. With both setups, BRUCE achieved stable walking for over 10 minutes, aided significantly by the tibia and foot modifications. The narrower tibia design created additional clearance for foot placement, reducing collisions, while the wider foot improved stepping stability.

As shown in Fig. 3.16(a) and Fig. 3.17(a), the parallel 4-bar ankle configuration resulted in knee and ankle joint torques aligning in the same direction for most of the gait cycle. This caused the knee actuator to counteract the ankle actuator, as predicted by Eq. (2.61) and Eq. (2.62). Implementing the reversed 4-bar linkage mechanism addressed this issue by altering the ankle actuator's rotation direction. As observed in Fig. 3.16(b) and Fig. 3.17(b), the knee actuator torque decreased significantly, and the torque profile became more distributed and sparser. This indicates that the modified mechanism not only reduced the load on the knee actuator but also enhanced energy efficiency by optimizing the torque output for both joints.

The summarized results in Table 3.3 highlight that the reversed ankle configuration reduces average knee actuator torque by 39.1%, average ankle actuator torque by 26.8%, and overall power consumption from 67.9 W to 54.0 W—a 20.5% saving in energy efficiency.

Table 3.3: Average actuator torque and power for Benchmark Test 3: Walking

Parameter	**Parallel Ankle**	**Reversed Ankle**	**Changes**
Knee Actuator	1.84 [Nm]	1.12 [Nm]	↓ 39.1%
Ankle Actuator	0.56 [Nm]	0.41 [Nm]	↓ 26.8%
Total Power	67.9 [W]	54.0 [W]	↓ 20.5%

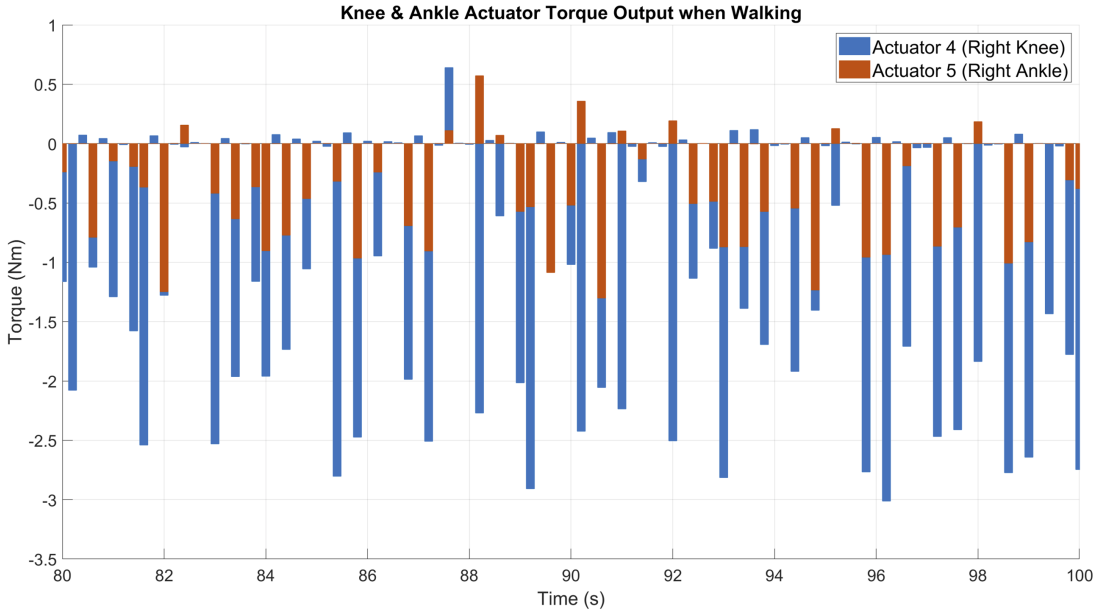

(a)

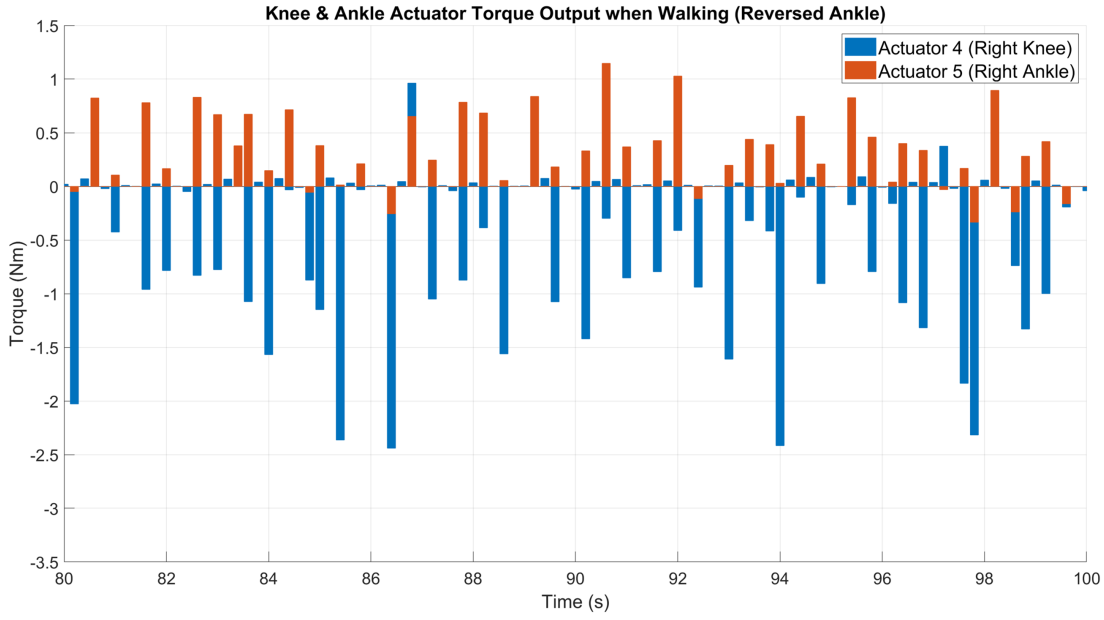

(b)

Figure 3.16: The output torque for the knee and ankle actuators on the right leg during Benchmark Test 3: Walking.

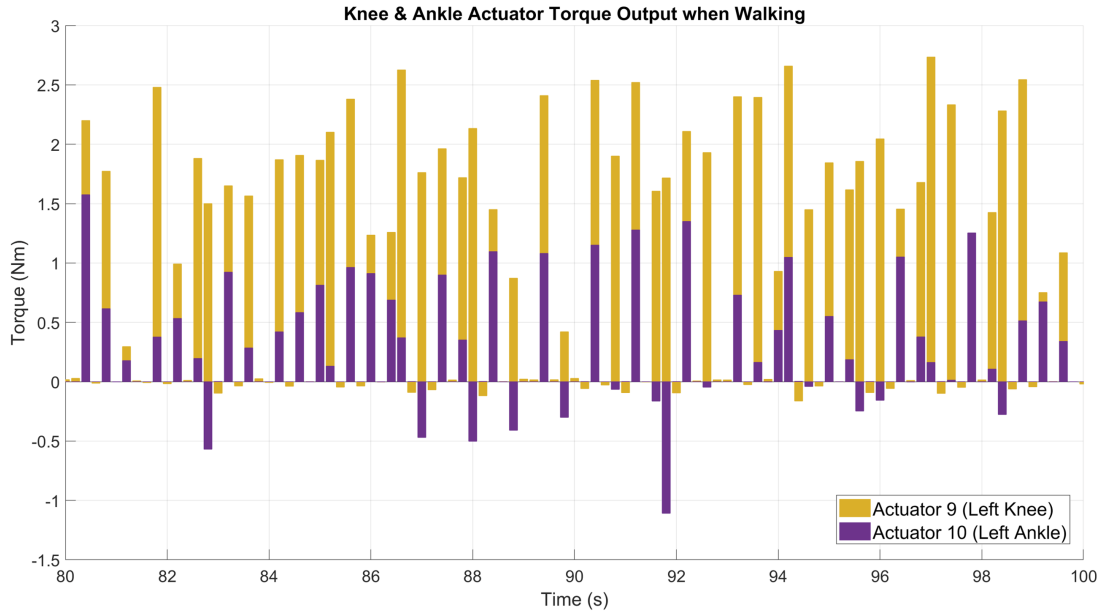

(a)

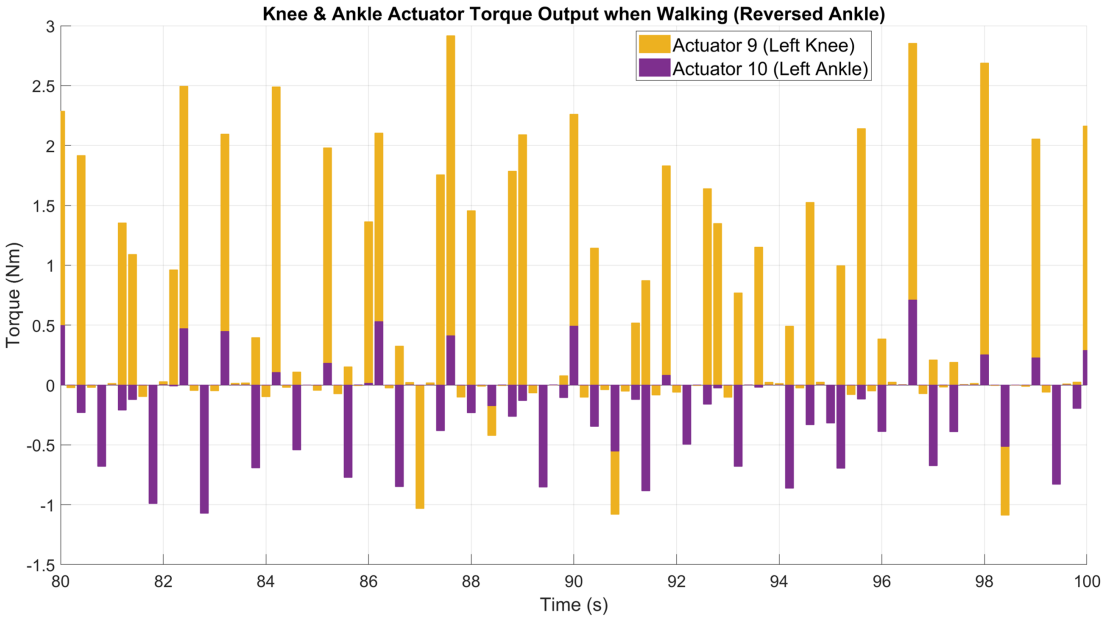

(b)

Figure 3.17: The output torque for the knee and ankle actuators on the left leg during Benchmark Test 3: Walking.

3.7.4 Jumping

The jumping test serves as a critical evaluation of BRUCE Refresh's capability to execute highly dynamic movements. This test aims to assess BRUCE's performance using both the parallel 4-bar and reversed 4-bar ankle configurations while implementing the kinodynamic jumping and heuristic landing planners developed by Jingwen Zhang [5]. During the test, BRUCE was commanded to perform a series of jumps under each configuration. However, the landing process for the reversed ankle configuration revealed some challenges due to the nonlinearity introduced by the modified reversed 4-bar linkage mechanism. This nonlinearity resulted in more jerks and disturbances in the torque plots, as observed in Fig. 3.18(b), compared to the smoother torque profile in Fig. 3.18(a) for the parallel configuration.

Despite the less-than-perfect landing performance with the reversed ankle configuration, the jumping test demonstrated a significant improvement in the peak lifting-off torque. Notably, the knee actuator's peak torque during the lift-off phase dropped dramatically from 5.08 Nm with the parallel ankle configuration to just 1.59 Nm with the reversed configuration, representing a substantial 68.7% reduction. This reduction highlights the efficiency gains achieved by the reversed 4-bar linkage mechanism, which redistributes torque more effectively during high-energy movements. Additionally, the reduction in peak torque for the knee actuator significantly mitigate overheating issues, thereby extending the actuator's lifespan. Furthermore, this modification unlocks the potential for BRUCE to perform more ambitious dynamic maneuvers, including higher jumps and even backflips, demonstrating the platform's enhanced capability for advanced dynamic locomotion tasks.

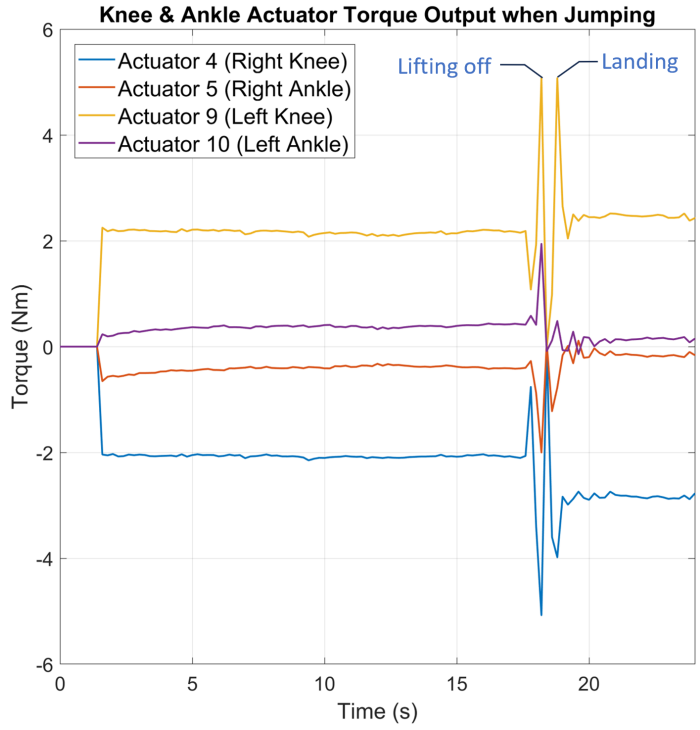

(a)

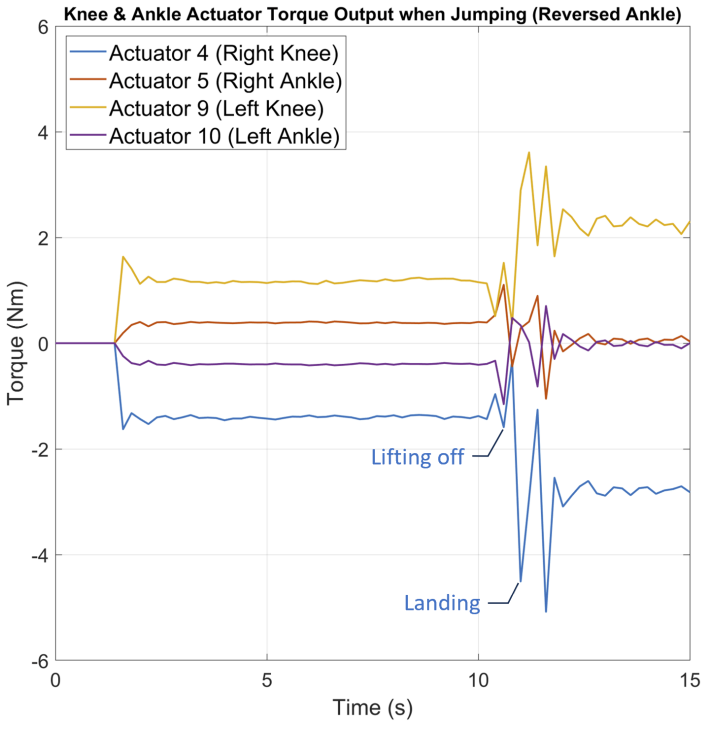

(b)

Figure 3.18: The output torque for the knee and ankle actuators during Benchmark Test 4: Jumping.

3.7.5 Conclusion

The series of verification tests conducted on BRUCE Refresh highlight the significant advantages of the modified reversed 4-bar linkage mechanism on the ankle joint, showcasing its effectiveness in addressing key performance challenges and enhancing dynamic locomotion capabilities.

One of the most significant improvements is the increase in the knee joint torque range, allowing the knee and ankle actuators to work collaboratively rather than opposing each other, resulting in more efficient torque redistribution. This collaboration leads to a substantial reduction in knee actuator torque, with decreases observed across all tests ranging from 34.9% to 68.7%. Additionally, the torque output from the ankle actuators drops significantly, with reductions between 11.2% and 60.0% across the tests. Furthermore, the winding temperatures of the actuators were notably reduced, improving thermal management and enhancing overall reliability during prolonged operations.

The design also improves energy efficiency, with power consumption reduced by over 20% in walking tests. This improvement translates directly into extended robot walking time, allowing BRUCE to perform continuous tasks for longer durations. Furthermore, the increased torque efficiency supports more dynamic behaviors, such as higher jumping potential. The jump test results confirm a significant reduction in peak torque at the knee joint, paving the way for more ambitious maneuvers, including higher jumps and possibly back flips.

In summary, the reversed 4-bar ankle mechanism introduces critical performance upgrades for BRUCE Refresh, making it a more robust and energy-efficient platform for humanoid robotics research. These enhancements solidify its suitability for dynamic locomotion applications and demonstrate its potential to tackle more complex movements in the future.

CHAPTER 4

YORI – Yummy Operations Robot Initiative

Figure 4.1: YORI CAD

4.1 Introduction

Recent advancements in robotic manipulators have focused on improving precision, dexterity, and strength, particularly for industrial tasks like assembling, welding, and heavy lifting. While highly effective in structured environments, these platforms often lack adaptability to the unknown settings and safe interaction capabilities with humans. The rise of collaborative robots (cobots) has shifted the focus toward manipulators that can operate safely alongside humans and adapt to dynamic and unstructured settings. This has driven the integration of sensors such as tactile, force/torque, and vision systems, enabling robots to detect obstacles, identify objects, and navigate safely. However, the reliance on expensive sensors and the lack of abilities for highly dynamic motions limit their feasibility for broader use in academia or individual researchers.

The growing demand for accessible and versatile robotic manipulators with high dynamic performance is driving research toward platforms powered by proprioceptive actuators. These actuators use current sensing to provide real-time feedback on torque and force, enabling precise and responsive movement control while enhancing safety during human-robot interactions. This makes them an ideal solution for dynamic and collaborative environments. Their ability to handle rapid and complex motions addresses the limitations of traditional robotic manipulators, which often rely on costly external sensors and may suffer from reliability issues. Additionally, the cost-effectiveness and accessibility of the proprioceptive-actuated manipulators could revolutionize daily life, assisting with household chores, caregiving, and even cooking.

To further explore dynamic manipulation and human-assistive robotics, we developed YORI (Yummy Operations Robot Initiative), an autonomous robotic cooking system that demonstrates the capabilities of proprioceptive actuators. YORI features a dual-arm manipulator optimized for culinary tasks and operates

within a modular kitchen setup equipped with tools designed for robotic use. This innovative system showcases a versatile approach to automating cooking processes and highlights the broader potential of robotics in everyday environments.

4.2 YORI Prototype

During the early stages of the project, we developed a prototype dual-arm manipulator using servo actuators for the verification of performing cooking tasks using robotic manipulators [6]. Each arm is independently designed with 5 degrees of freedom (DOFs), complemented by an additional single DOF at the central linkage connecting the two arms. This extra actuator expands both the individual reach of each arm and the shared workspace between them. Moreover, the additional joint enhances the arm's configuration for cooking tasks by introducing a redundant pitch joint, enabling the arms to generate precise linear planar trajectories—essential for many intricate culinary actions.

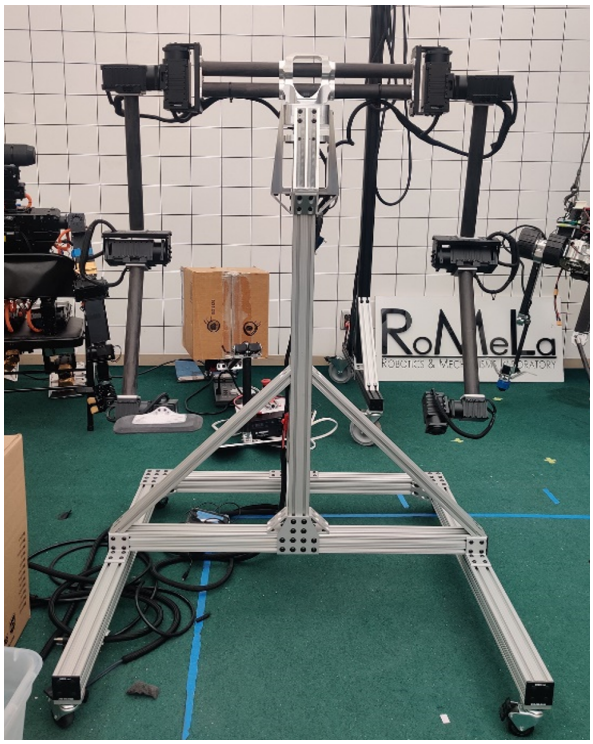

Figure 4.2: Prototype of YORI with traditional servo actuators [6]

However, due to the usage of rigid servo actuators and lack of force/torque sensors, the robot manipulator was unable to complete certain tasks where a precise torque estimation or rapid movement was required, such as cutting and tossing food. Furthermore, since all the components including actuators and structural parts are off-the-shelf products without any design optimizations, the payload at the end effector was limited and the overall workspace was not ideal.

4.3 Mechanical Design

With the numerous constructive experiences from the servo motor actuated manipulator prototype, we developed the next-generation proprioceptive dual-arm manipulator using high-performance quasi-direct drive actuators. These actuators allow for the manipulator's compatibility with many cooking tasks, in particular those requiring impacts and precise force control, while being compliant to changes in the constructed environment.

4.3.1 Mechanical Configuration

Joint Configuration

Unlike traditional robotic manipulators with 6 or 7 degrees of freedom (DoF) per arm, YORI features a streamlined design with a total of 11 DoF. This includes a single torso roll joint at the center and two 5-DoF arms on either side. Each arm is equipped with shoulder pitch and yaw joints, an elbow pitch joint, and a 2-DoF wrist that includes pitch and roll joints. The torso rotational joint allows the entire shoulder assembly to rotate, further expanding the robot's reachable workspace and optimizing the shared workspace between the arms. This design choice prioritizes lightweight construction and dynamic performance, enhancing payload capacity and energy efficiency while maintaining sufficient flexibility for generalized cooking operations.

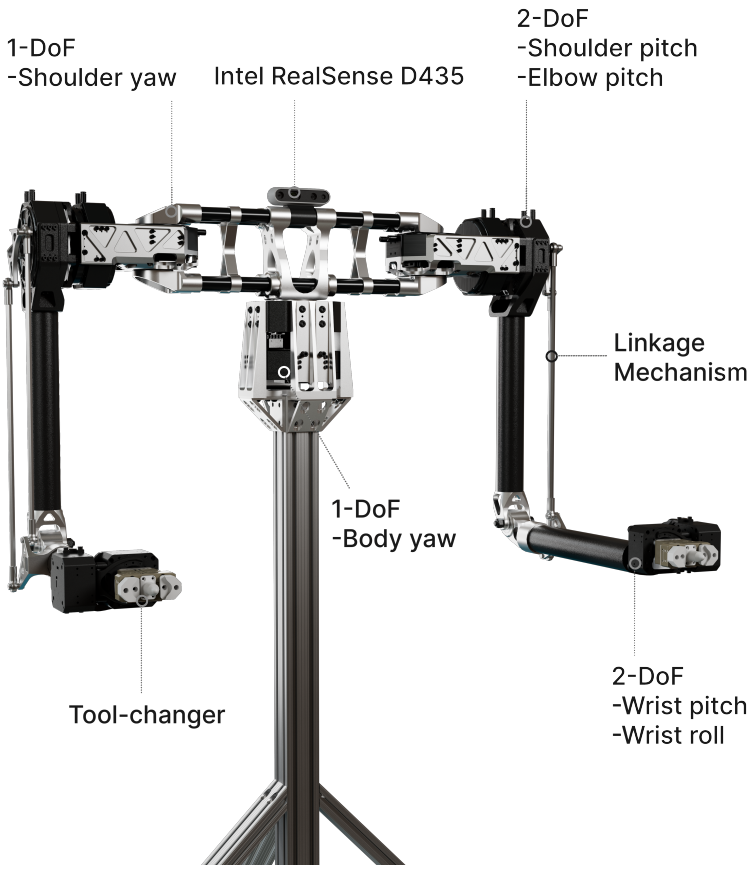

Figure 4.3: YORI Dual-arm manipulator platform with proprioceptive actuation [7]

Link Length

The dimensions of the arm links are inspired by the proportions of the human upper body, ensuring that the robot can mimic human-like movements and interactions effectively [37]. Specifically, the upper arm and forearm are designed with lengths of 400 mm and 375 mm, respectively, providing an optimal balance between reach and precision. The clavicle link, which connects the two arms, measures 420 mm in length, enabling the robot to perform a wide range of tasks. This configuration allows both arms to collaborate on a single task or operate independently in separate areas of the workspace, making it a versatile tool for dynamic and efficient cooking operations. Table 4.1 provides a comprehensive summary of the key mechanical parameters.

To further enhance the performance and durability of the arms, carbon fiber tubes are used for all the arm links. This material was chosen for its combination of lightweight properties, high stiffness, and excellent durability, all of which are critical for achieving the dynamic motions required in a fast-paced cooking environment. Additionally, the lightweight construction results in a single arm mass of 5.3 kg, which is significantly lighter compared to the 8.7 kg arm of BLUE [36] and the 18.4 kg arm of the UR5e [35]. This reduction minimizes the energy consumption of the actuators and enhances the system's overall efficiency.

Table 4.1: YORI Mechanical Parameters

Parameter	**Value [Unit]**	**Parameter**	**Value [Unit]**
Clavicle mass	1457 [g]	Clavicle length	420 [mm]
Shoulder mass	2154 [g]	Shoulder length	150 [mm]
Upper arm mass	1570 [g]	Upper arm length	400 [mm]
Forearm mass	854 [g]	Forearm length	375 [mm]
Wrist mass	733 [g]	Wrist length	85 [mm]
Total mass	12079 [g]	Wrist length	1270 [mm]

4.3.2 Actuation Selection

Selecting appropriately sized actuators and transmissions for each joint are critical steps in the hardware design process, and it begins with joint torque estimation. For YORI, a dual-arm manipulator designed primarily to operate within the sagittal plane, the pitch actuators at the shoulder, elbow, and wrist joints are subjected to the highest torque due to the payload. To estimate the loading conditions under the most demanding scenarios, a static moment balance analysis is conducted. This approach evaluates the worst-case scenario, where the manipulator is fully

extended horizontally, as described in [6]. Assuming a 3 kg payload attached to the end-effector and incorporating a safety factor of 1.5, the maximum calculated torque loads are 37.93 Nm for the shoulder, 20.29 Nm for the elbow, and 3.749 Nm for the wrist pitch joints. To meet these torque demands, three types of proprioceptive actuators from Westwood Robotics [38] are utilized, with their specifications detailed in Table Table 4.2.

Table 4.2: YORI proprioceptive actuator specifications

	Actuator 1	**Actuator 2**	**Actuator 3**
Mass [g]	650	925	250
Gear reduction	6	6	9
Continuous torque [Nm]	16.8	33	4.2
Peak torque [Nm]	33.5	67	10.5
Speed constant [RPM/V]	14.3	7.1	27.3
Application [joint]	Torso yaw Shoulder yaw	Shoulder pitch Elbow pitch	Wrist pitch Wrist roll

The actuator selections are verified in simulation by applying the physical properties of the actuators and the links throughout the joint trajectories of multiple cooking tasks. Table 4.3 shows the average and maximum torque exerted at each joint with a 5 kg payload, which shows that the selected proprioceptive actuators are suitable for the desired working scenarios.

4.3.3 Joint and Linkage Design

Like BRUCE, YORI's dual-arm manipulator is designed for dynamic tasks, emphasizing lightweight construction and low inertia. To achieve this, the actuators are strategically distributed to keep heavy components near the torso rather than positioning them directly at each joint, as is common in traditional robotic manipulators. The torso yaw, shoulder yaw, and shoulder pitch actuators remain

Table 4.3: Maximum and average joint torque with 5kg payload from cooking task simulations

Joint	**Torso yaw**	**Shoulder yaw**	**Shoulder pitch**	**Elbow pitch**	**Wrist pitch**	**Wrist roll**
Avg. τ (N·m)	1.492	0.823	13.302	15.634	3.499	0.912
Max. τ (N·m)	12.223	6.648	31.315	23.965	4.585	2.201
Min. angle	-180°	-130°	-180°	-150°	-133°	-180°
Max. angle	180°	130°	180°	95°	111°	180°

directly mounted to their respective joints, as these joints are already near the torso. However, the elbow pitch actuator is relocated closer to the shoulder to reduce the manipulator's distal mass. The wrist pitch and roll actuators, being relatively small and lightweight, are kept at their respective joints to maintain a straightforward design and minimize system complexity.

Relocating the elbow pitch actuator required a torque transmission mechanism to transfer force effectively from the actuator to the elbow joint. Although timing belts are a common choice due to their simplicity and ability to transmit continuous rotation, their low stiffness introduces compliance between belt teeth and pulleys, which lowers the rotor-belt resonant frequency and limits torque control bandwidth [49]. To address this, a highly stiff and reliable linkage mechanism was chosen for torque transmission.

For a regular parallelogram 4-bar linkage mechanism, it has advantages of simplicity and high efficiency but could suffer from the singularity when one link is fully extended and aligned with another link, leading to a loss of controllability. The linkages are also susceptible to buckling under excessive compressive forces. In YORI, the double 4-bar design overcomes these issues by employing two parallelogram linkages to transmit torque with a 1:1 ratio, as shown in Fig. 4.5. This configuration maximizes the elbow's range of motion while eliminating singularity

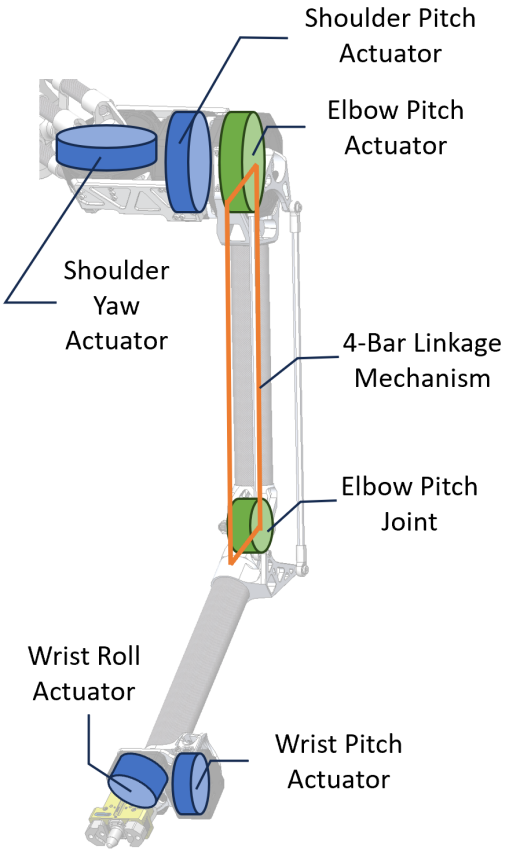

Figure 4.4: YORI manipulator actuation schemes

when the arm is fully extended. The elbow joint achieves a motion range from -150° to 95°, with backward bending capabilities that enhance YORI's ability to reach areas behind its body. Additionally, the dual-linkage design ensures no excessive compressive forces act on the linkages, effectively preventing buckling.

As demonstrated in Fig. 4.5, linkage 1 primarily handles torque during elbow flexion, while linkage 2 takes over during elbow extension, ensuring smooth and efficient motion transfer throughout the full range of elbow operations.

4.4 Design Optimization

Following the design guidelines from BRUCE and to further enhance the performance and efficiency of YORI, topology optimization was employed in the de-

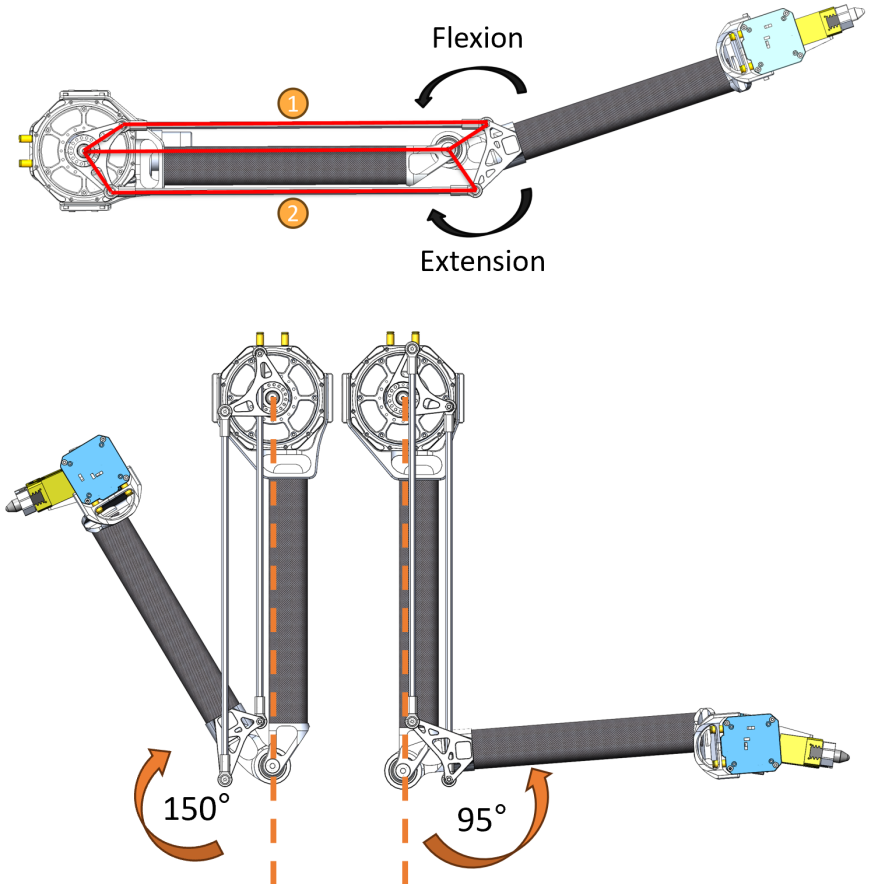

Figure 4.5: YORI elbow joint with 4-bar linkage mechanism

sign of critical structural components. Topology optimization is a computational design technique that identifies the optimal material distribution within a given design space to achieve specific performance objectives, such as minimizing weight while maintaining structural integrity. As demonstrated in Fig. 4.6, this approach was applied to all the structural parts like brackets and housings to reduce overall weight and inertia, which are critical factors for dynamic tasks like cooking. By leveraging advanced algorithms and SolidWorks simulation, material was strategically removed from low-stress regions while reinforcing areas experiencing higher loads, resulting in a lightweight yet robust design. The optimized components not only improve energy efficiency and dynamic response but also increase payload capacity, enabling YORI to handle a wider range of cooking tasks.

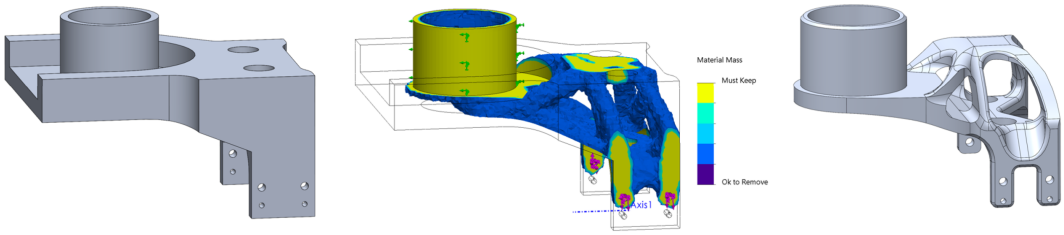

(a) Wrist pitch bracket

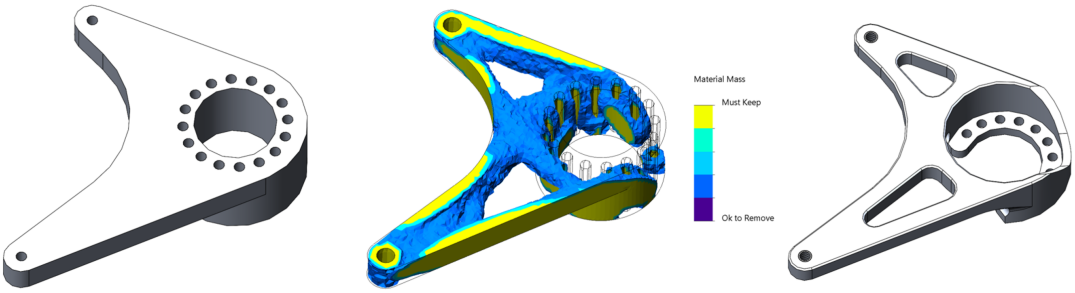

(b) 4-bar linkage driver

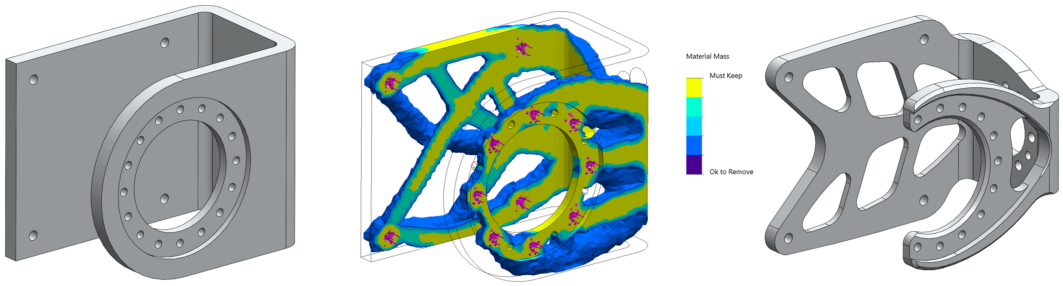

(c) Wrist roll bracket

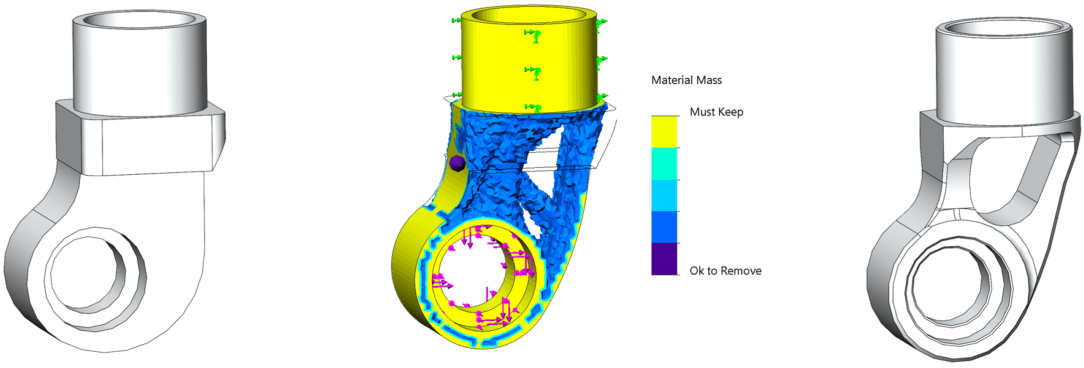

(d) Elbow bearing housing

Figure 4.6: Selected YORI structure parts with topology optimization

4.5 Tool Changing System

A general-purpose end-effector on a manipulator can handle multiple tasks but often limits the system's versatility. In contrast, a manipulator equipped with interchangeable specialized end-effectors can adapt to a broader range of applications [56]. To maximize versatility, YORI incorporates a pneumatic tool changer system, enabling it to seamlessly switch between various kitchen utensils such as a pan, container, knife, and meat tenderizer. Each tool is designed with a custom tool plate that the tool changer's pneumatic fingers grip and secure using compressed air, as illustrated in Fig. 4.7.

A guiding cone mechanism ensures precise alignment by compensating for offsets before the fingers engage with the tool plate. This system effectively corrects positional discrepancies, allowing up to 8 mm of translational misalignment and 10 degrees of angular misalignment during the locking process. Experiments demonstrated the reliability and accuracy of the tool changer, showcasing its ability to enable YORI to perform diverse cooking tasks with efficiency and adaptability.

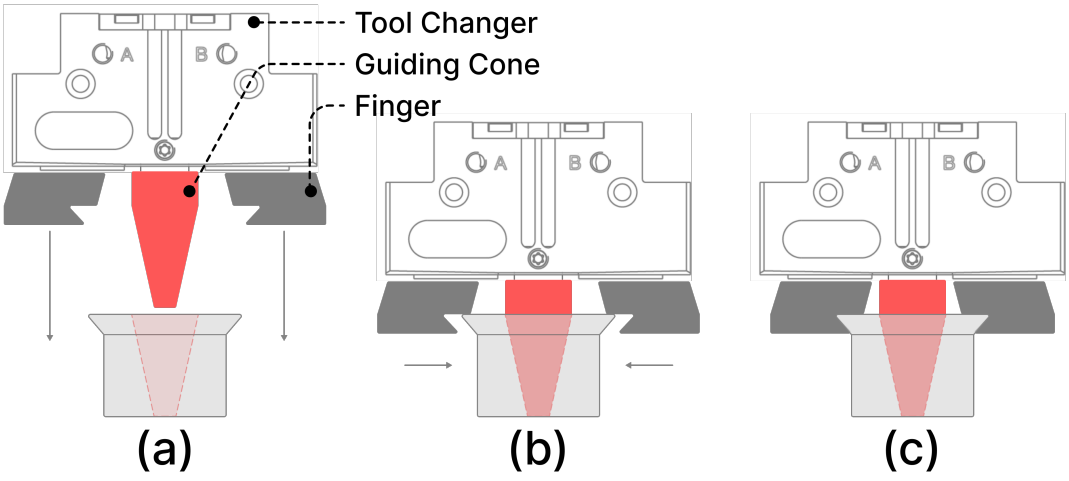

Figure 4.7: Tool Changer Mechanism Details [7]: (a) A guiding cone aligns the tool changer to the correct grasping position, (b) Compressed air actuates the tool changer's fingers for a secure grip, (c) The tool changer fully locks onto the tool plate for robust attachment.

4.6 Modular Kitchen

YORI's modular kitchen promotes an organized and efficient cooking environment by utilizing a structured cooking cell design rather than a cluttered setup. This modular kitchen incorporates. The controlled environment improves the system's reliability, while the modular design enhances scalability, allowing for future expansion and adaptability [7].

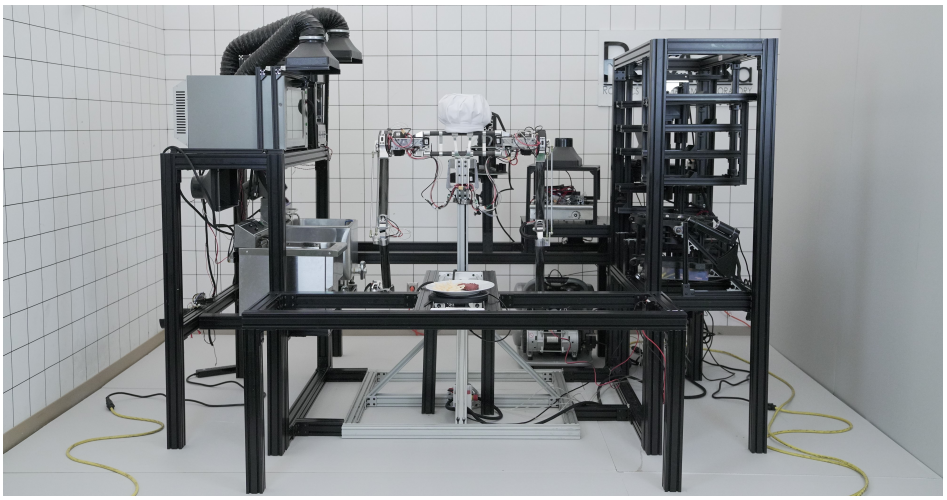

Figure 4.8: YORI Dual-arm manipulator with the modular kitchen cell [7].

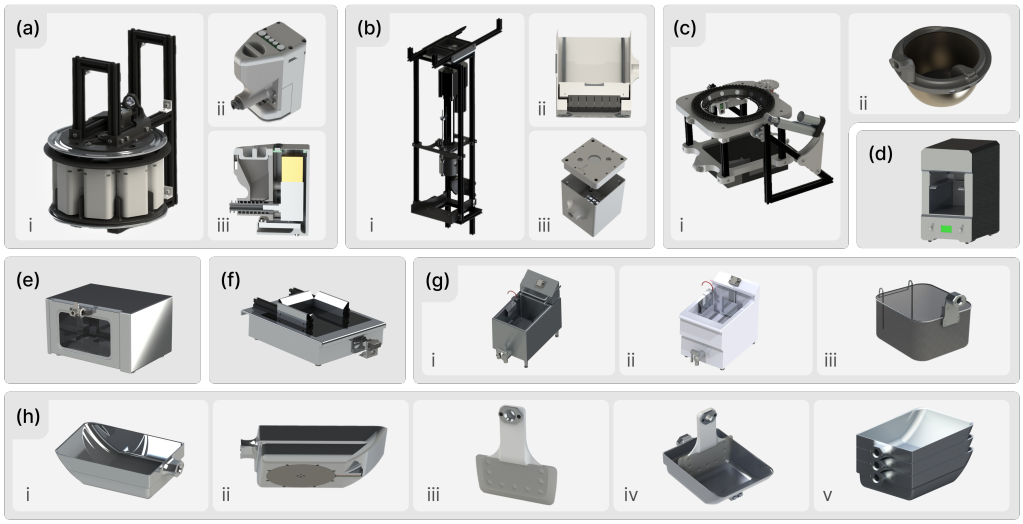

Figure 4.9: A comprehensive set of appliances and corresponding tools for YORI automated kitchen cell [7]: a) spice dispenser equipped, b) food processor, c) rotating mixer paired with a detachable pot, d) salamander broiler, e) convection oven, f) induction cooktop, g) deep fryer and water boiler, h) customized induction pan with squeegee sweeping tool.

CHAPTER 5

Guidelines for Highly Dynamic Robot Platforms Design

Through the experience of designing the BRUCE and YORI robotic platforms, I have developed a strong foundation in the principles of designing highly dynamic robotic systems. In this dissertation, I aim to share these insights by presenting comprehensive guidelines for the design of such platforms.

5.1 Design Requirements

The foundation of a successful high-dynamic robot platform design lies in clearly understanding the design requirements and priorities. These include specific performance goals such as workspace, payload capacity, energy efficiency, and cost-effectiveness. Understanding the application context, such as locomotion or manipulation tasks, helps guide the selection of design parameters, ensuring the robot can achieve its intended functions.

A fundamental principle for designing highly dynamic robotic platforms is maintaining a lightweight construction, particularly by reducing the distal mass in moving limbs. Minimizing limb inertia is critical for enabling dynamic behaviors such as rapid acceleration, precise control, and efficient energy utilization. Additionally, a lightweight design inherently contributes to energy efficiency, as a lighter system demands less power to achieve the same performance.

Other requirements, such as end-effector dexterity, speed, payload capacity, and cost-effectiveness, necessitate careful consideration of joint and linkage configurations. Strategic design choices play a significant role in optimizing the overall performance of the system, as summarized in Table 5.1.

Table 5.1: Design requirements vs. elements need to prioritize

	End-effector Dexterity	**Payload Capacity**	**Maximum Speed**	**Cost Effectiveness**
Workspace	+++	++	++	+
High Torque	++	+++	+	++
Lightweight	++	+	+++	+
Minimum DoF	+	++	+++	+++

5.2 Define Hardware Configuration

Defining the hardware configuration is a pivotal step in the design process, involving key decisions about the degrees of freedom (DoF), joint placement, and actuator distribution. These elements collectively shape the robot's performance, efficiency, and adaptability to specific tasks.

One of the critical considerations is selecting the optimal DoF to balance task efficiency and system complexity. While higher DoF provides greater flexibility, it also increases the challenge of control and adds to the system's mass. BRUCE's under-actuated leg design (Section 2.2.1) and YORI's 5-DoF arms (Section 4.3.1) strike a balance by optimizing DoF based on task requirements. By prioritizing essential movements and eliminating unnecessary complexity, these designs achieve dynamic performance without compromising efficiency or reliability.

Another key factor is balancing affordability with performance. Practical applications of dynamic robots require cost-effective solutions that do not compromise functionality. BRUCE hardware system design (Section 2.2.8) demonstrate this principle through the use of scalable designs and economical components, making the platform accessible while preserving the performance standards needed for high-dynamic manipulation tasks. These strategies ensure that the hardware

configuration supports both operational excellence and real-world feasibility.

5.3 Rapid Prototyping

Rapid prototyping accelerates design iterations, allowing early identification of flaws and areas for improvement. Once the design requirements are established and the overall hardware configuration is finalized, prototyping can begin using readily available materials and components, such as 3D-printed parts and traditional servos. This approach enables the creation of functional prototypes that can undergo real-world testing to validate key design assumptions against practical performance.

The initial prototypes (Section 2.2.4 and Section 4.2) do not need to achieve perfect system readiness or performance but should effectively test critical system requirements, such as workspace validation and basic torque range assessment. Insights gained from these tests provide valuable feedback, guiding refinements and enhancements that significantly improve the final platform design. Rapid prototyping ensures that the design evolves iteratively, aligning theoretical models with practical realities.

5.4 Actuation Selections

Selecting appropriate actuators is critical for achieving dynamic performance. Proprioceptive actuators are particularly well-suited for such applications due to their compact design, high torque transparency, and exceptional backdrivability. These features enable precise force and torque control, making proprioceptive actuators ideal for tasks demanding stable locomotion and rapid, responsive manipulation.

One key challenge associated with proprioceptive actuators is their tendency to overheat under excessive torque loads. To address this, torque estimation during

the design phase is essential to ensure actuators can handle peak loads without compromising reliability. This was exemplified in the torque analyses conducted for BRUCE's knee (Section 2.2.2) and YORI's arm joints (Section 4.3.2), where proactive design considerations mitigated overheating risks.

Moreover, proprioceptive actuators reduce dependency on costly external sensors for force and torque feedback, leading to significant cost savings. By integrating these actuators, dynamic platforms can achieve high performance while maintaining a streamlined and cost-effective design.

TOn the other hand, traditional high-gear-ratio servos also have their place in dynamic robotic systems. While they lack the backdrivability of proprioceptive actuators, their simplicity and cost-effectiveness can be advantageous. Using such servos is entirely acceptable if they offer specific benefits and do not compromise the overall dynamic performance of the system, such as the arm actuators on BRUCE's arms (Section 2.2.8). Balancing actuator selection based on task-specific requirements ensures an optimal combination of performance and functionality.

5.5 Mechanism Selections

Efficient mechanisms are key to the success of high-dynamic platforms. Mechanisms must be optimized for reliability and functionality while considering the range of motion, torque requirements, and overall system efficiency.

Instead of directly mounting actuators on joints—a straightforward but sometimes inefficient approach—mechanisms can be used to relocate actuators or transmit torque effectively. This allows for reduced joint inertia, improved dynamic motion, and maximized workspace. Three widely used mechanisms for torque transmission in dynamic robots include timing belt systems, linkage mechanisms, and cable-driven systems. The advantages and disadvantages of each transmission system are illustrated in Table 5.2.

5.5.1 Timing Belt Transmission

Timing belts are a common choice for torque transmission and can be configured either before or after the gearbox. When positioned before the gearbox, the belt transmits higher-speed and lower-torque motion. The torque will be amplified at the robot joint through a gearbox, which could bring extra mass and inertia to the system. When placed after the gearbox, the belt carries higher torque but slower motion, demanding robust materials and higher stiffness on the belt to increase the joint stiffness and torque bandwidth. Timing belts offer advantages such as smooth motion and continuous rotation but can introduce compliance if not properly tensioned or if unsuitable materials are used.

5.5.2 Linkage Mechanisms

Linkage systems, such as 4-bar linkages, are ideal for tasks requiring rigidity and speed. These systems can be tailored to specific ranges of motion and are highly efficient for torque transmission. However, traditional 4-bar linkages can face challenges such as singularities, where certain configurations lead to a loss of controllability, and buckling under high compression loads. Solutions like the double 4-bar linkage mechanism, as used in YORI (Section 4.3.3), eliminate singularities and enhance workspace utilization. Moreover, mechanical advantages of special linkage systems can be used to prioritize joint torque and speed, such as the reversed 4-bar linkage design used in BRUCE's ankle (Section 3.3.2). These designs are particularly effective for tasks requiring higher stiffness and control bandwidth over an extended range od motion.

5.5.3 Cable-Driven Systems

Cable-driven mechanisms, such as the cable-driven differential pulley system used in BRUCE's hip joint (Section 2.2.4), are excellent for reducing joint inertia and

flexible actuator positioning. However, these systems require careful selection of cables and precise pulley design to avoid issues like creep and frequent pre-tensioning. High-strength, low-stretch cables and pulleys with optimized grooves are critical to maintaining consistent tension and ensuring long-term reliability.

Table 5.2: Transmission mechanisms advantages and disadvantages

	Timing Belt Before Gearbox	**Timing Belt After Gearbox**	**Linkage**	**Cable-Driven**
PROS	Amplified stiffness Continuous rotation	Continuous rotation Simplicity	High stiffness Simplicity High bandwidth	Flexibility Continuous rotation Average stiffness
CONS	Complexity Pre-tension Higher inertia	Pre-tension Low stiffness Low bandwidth	Limited rotation Singularity Buckling	Complexity Pre-tension

5.6 Sub-system Designs

Each subsystem must be meticulously designed to align with the overall goals of the robotic platform. For BRUCE, reducing leg mass and emphasizing knee torque were pivotal for achieving high-dynamic locomotion. In contrast, YORI's modular kitchen setup (Section 4.6) and pneumatic tool changers (Section 4.5) were tailored to maximize functionality and adaptability for dynamic manipulation tasks. By optimizing subsystems, platforms benefit from enhanced performance, reduced energy consumption, and improved reliability.

Reducing mass and inertia for each part in all sub-systems is critical for achieving dynamic behaviors. Lightweight components, such as carbon fiber tubes, CNC machined aluminum part, and compact mechanisms, help decrease energy requirements, enable faster response times, and increase payload capacity. Sub-systems designed with this focus ensure agility and efficiency in highly dynamic environments.

Modularity and task-specific designs further enhance adaptability and scalability. Modular systems allow for easier maintenance, faster upgrades, and seamless integration of new components or tools. This approach also supports customization, enabling the platform to perform specialized tasks while remaining versatile for broader applications.

5.7 Topology Optimization

Topology optimization (Section 2.3.1) plays a crucial role in refining the design of robotic platforms to achieve an optimal balance between strength and weight. After the preliminary design of each subsystem, topology optimization is applied to ensure efficient material distribution, resulting in robust yet lightweight structures capable of withstanding high dynamic loads. This process enhances the strength-to-weight ratio, enabling the development of agile and high-performance platforms like BRUCE (Section 2.3.2) and YORI (Section 4.4).

However, achieving the ideal scenario—where both strength increases and weight decreases—is not always feasible. For platforms prioritizing dynamic performance, maintaining a lightweight design often takes precedence over maximizing structural strength. As a result, topology optimization typically yields parts with reduced but sufficient strength, ensuring the overall system remains lightweight without compromising functionality.

The accuracy of topology optimization depends heavily on the precise definition of loading conditions during the design process. Accurate modeling of these conditions is critical to producing results that are both practical and reliable. Additionally, interpreting and implementing topology optimization results require thoughtful engineering judgment. The raw output often appears as a meshed model, which must be translated into a manufacturable and functional part.

For both BRUCE and YORI, topology optimization was pivotal in reducing

weight while preserving the structural integrity of key components. This process directly contributed to their dynamic capabilities by enabling a design that could support high-speed movements and heavy payloads without excess material or unnecessary complexity.

5.8 Comprehensive Experimental Validation

Finally, comprehensive experimental validation is an indispensable step in evaluating the performance and reliability of highly dynamic robotic platforms. Rigorous testing under diverse conditions ensures that the design meets its intended functionality and identifies areas for improvement.

For BRUCE, extensive trials demonstrated its exceptional capabilities in high-dynamic locomotion (Section 2.5), validating the effectiveness of the design choices, including the cable-driven differential pulley system (Section 2.2.4) and the reversed 4-bar linkage mechanism on the ankle (Section 3.7). Similarly, YORI underwent thorough testing in general cooking tasks, which underscored the advantages of its proprioceptive actuation and modular kitchen design.

A well-structured series of verification tests is essential to evaluate the performance and functionality of each subsystem. These tests should cover a broad range of conditions and scenarios to ensure robustness. For instance, workspace verification, torque range testing, and stability analysis are fundamental steps in confirming design assumptions.

Experimental data derived from these tests are invaluable for refining both hardware and software elements of the platform. Feedback from the testing phase allows for iterative improvements, ensuring the final system achieves optimal performance and reliability for its intended applications.

CHAPTER 6

Conclusion

6.1 Summary

This dissertation has explored and advanced the design and implementation of highly dynamic robotic systems through two groundbreaking platforms: BRUCE, a miniature humanoid robot optimized for lower-body locomotion, and YORI, a dual-arm manipulation platform for cooking tasks. The research presented herein emphasizes innovative design strategies, actuator technologies, and design optimization techniques that collectively contribute to the development of accessible and efficient robotic platforms for dynamic tasks.

For BRUCE, the focus was on achieving dynamic lower-body locomotion in a compact and affordable design. By utilizing proprioceptive actuated joints, the robot demonstrates high dynamic capabilities, enabling agile and precise movements. The novel cable-driven differential pulley system for the hip joint introduces a lightweight yet robust mechanism, enhancing the robot's ability to execute complex maneuvers. Additionally, the innovative linkage mechanism minimizes leg inertia while prioritizing knee torque output, ensuring energy-efficient and high-performance locomotion. BRUCE represents a significant step forward in making advanced humanoid robotics accessible for broader applications.

YORI, on the other hand, pushes the boundaries of dynamic robotic manipulation with a minimal degree-of-freedom design tailored for kitchen tasks. Its 5-DoF dual-arm configuration balances simplicity, performance, and energy efficiency, reducing overall system complexity without compromising on task versatility. The introduction of a double 4-bar linkage mechanism eliminates motion singularities

and expands the workspace, enabling precise and seamless manipulation across a variety of cooking scenarios. YORI highlights the potential of specialized robotic platforms in addressing practical challenges in everyday environments.

A unifying theme in this research is the application of topology optimization as a design strategy to improve the strength-to-weight ratio of key structural components. This approach ensures that both BRUCE and YORI achieve high performance without sacrificing structural integrity or efficiency.

Finally, the dissertation outlines a comprehensive design guideline for highly dynamic robotic platforms, emphasizing the importance of lightweight structures, efficient actuation systems, and mechanisms tailored to specific dynamic tasks. These guidelines provide a foundation for future advancements in robotic systems, paving the way for versatile, robust, and cost-effective solutions in dynamic environments.

In conclusion, the research conducted for this dissertation demonstrates how thoughtful design and innovative engineering can expand the capabilities and applications of dynamic robotic systems. The advancements made through BRUCE and YORI underscore the potential for robotics to seamlessly integrate into complex and dynamic human environments, addressing practical needs with efficiency and reliability.

6.2 Future Works

The future research on BRUCE includes hardware optimizations and advanced control strategies. Firstly, efforts will focus on refining BRUCE's hardware to further enhance its dynamic performance. Specifically, optimizing the reversed ankle joint to minimize speed and torque nonlinearity is a critical step toward improving locomotion efficiency. Additional experimental studies are planned to validate BRUCE's high dynamic capabilities in diverse scenarios such as continuous walk-

ing and high jumping, ensuring its robustness across a wider range of applications. These improvements aim to make BRUCE a more versatile and reliable platform for advanced robotic applications.

On the software front, future work will prioritize learning-based control strategies to enable more adaptive and efficient locomotion. Deep reinforcement learning will be leveraged to achieve robust and natural movement patterns, while precise torque control will be implemented to enhance the robot's agility and stability during highly dynamic maneuvers. These advancements will not only improve BRUCE's performance but also set the stage for next-generation humanoid robots capable of navigating complex and unpredictable environments.

For YORI, hardware system refinement is needed alongside additional benchmark tests to verify its dynamic performance. Following the successful delivery of the first YORI prototype to the sponsor in 2023, efforts are now focused on rebuilding the manipulator platform with an improved design and functionality. Additionally, a scaled-down version of YORI is under development to explore more affordable and accessible hardware solutions for broader applications. These iterations aim to ensure YORI continues to evolve as a versatile and practical tool for dynamic manipulation tasks.

Learning-based control strategies will also be investigated to enhance YORI's adaptability to complex tasks and dynamic environments so that it realizes its full potential. The research will focus on dynamic box-catching and other high-velocity tasks, further validating the manipulator's performance with proprioceptive actuators. These studies will showcase the effectiveness of YORI's design in achieving both precision and speed in dynamic operations

APPENDIX A

LIMMS

Transporting a package from a storage facility to a customer's door typically involves highly specialized robots that divide tasks among different systems, like manipulator arms for sorting and wheeled vehicles for delivery. Recent efforts aim to unify these steps using legged or humanoid robots, but these bulky systems take up considerable space, reducing vehicle cargo capacity and limiting scalability and parallel task execution. To better solve this issue, we introduce LIMMS (Latching Intelligent Modular Mobility System), a compact solution addressing both the manipulation and delivery tasks of last-mile logistics while maintaining a minimal spatial footprint. LIMMS is a symmetrical, 6-degree-of-freedom (DoF) robotic appendage with wheels and latching mechanisms on both ends. Anchored at one end, a single LIMMS unit operates like a 6-DoF manipulator arm; multiple units can latch onto a package to function as a legged robot with the package itself as the body. During transit, LIMMS units fold compactly, taking up far less space than traditional systems and enabling numerous units to fit into one delivery vehicle—unlocking new possibilities for delivery optimization and hybrid planning [8, 57].

Project LIMMS ran from 2021 to 2023, during which I led the mechanical design and manufacturing efforts.

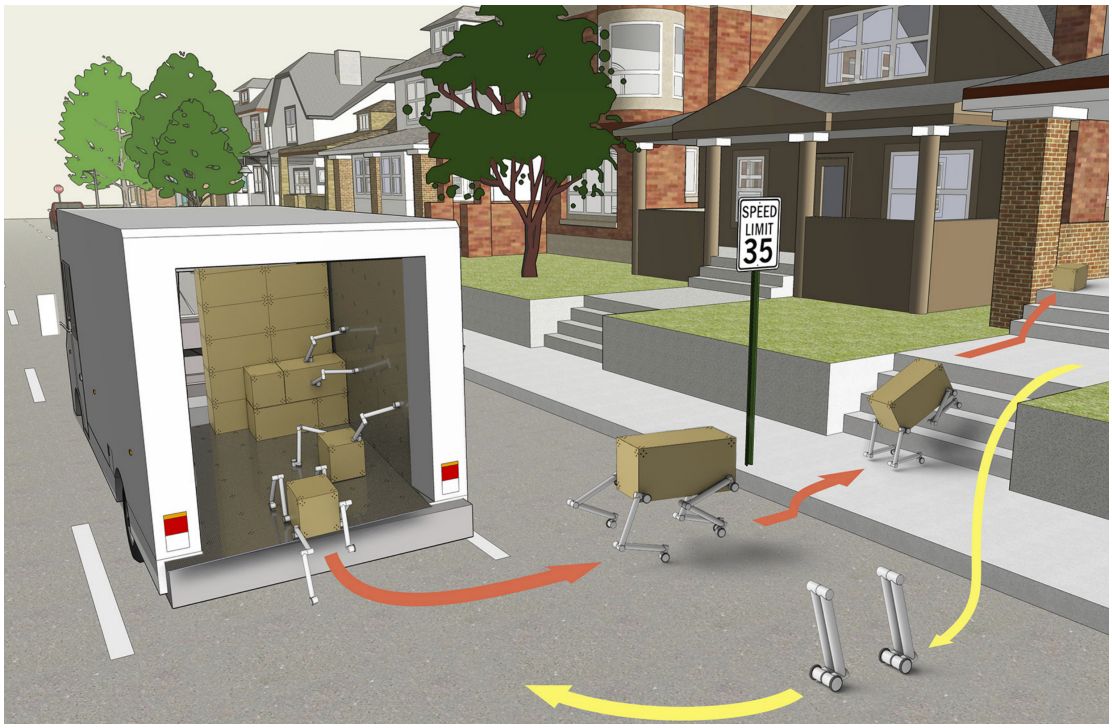

Figure A.1: LIMMS, or the Latching Intelligent Modular Mobility System, is designed for efficient last-mile delivery. While inside the delivery truck, LIMMS can pre-sort packages and queue them as needed, functioning like a manipulator by latching onto the truck walls to anchor itself. For package transport, four LIMMS units can attach to a box, using it as the central body to move the load like a quadruped robot. After delivery, each LIMMS unit switches to wheeled mode to return to the truck, ready for the next task. [8].

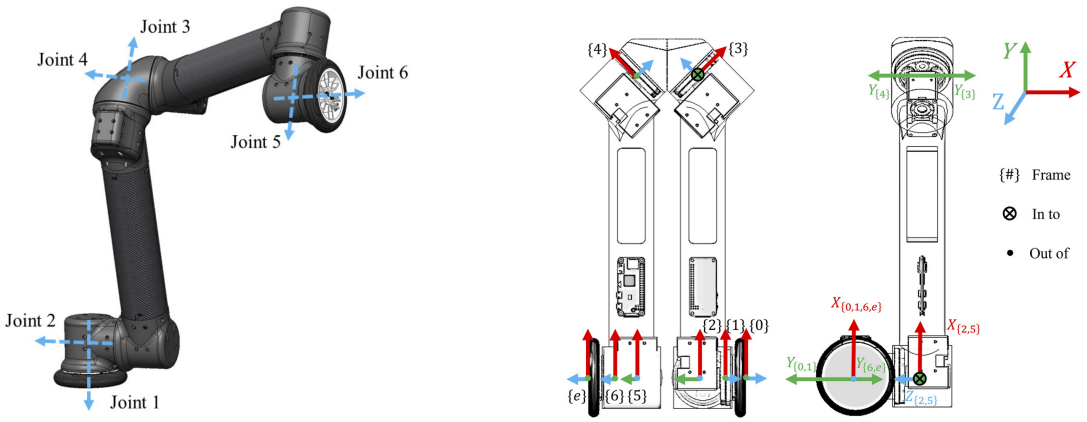

(a) (b)

Figure A.2: (a) LIMMS 6-DOF joint configuration. (b) *Left* depicts a front view of LIMMS with joint frames. *Right* shows a side view. Note that these are nontraditional DH frames. [8]

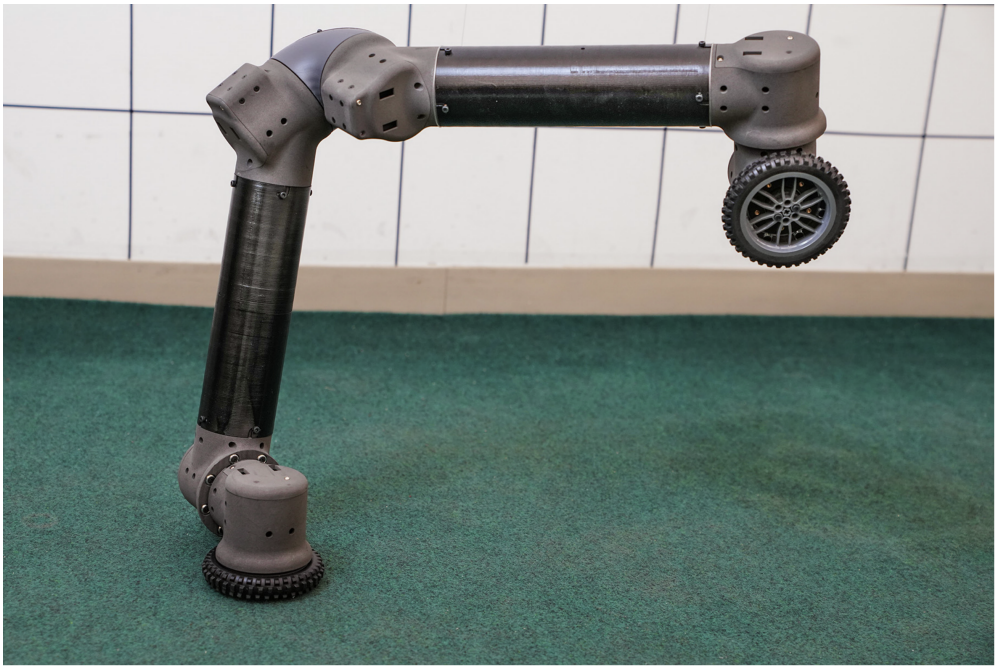

(a)

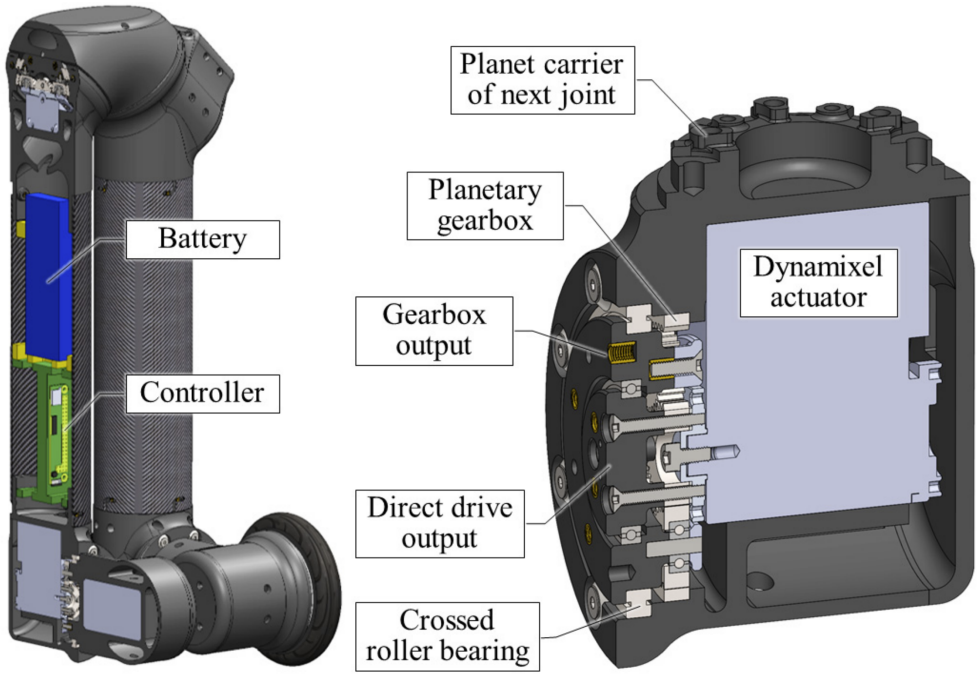

(b)

Figure A.3: (a) LIMMS hardware prototype. (b) Section view of LIMMS prototype using commercial off-the-shelf actuator with custom gearbox. [8]

APPENDIX B

ARTEMIS

ARTEMIS (Advanced Robotic Technology for Enhanced Mobility and Improved Stability) is a renowned full-size humanoid robot platform designed for dynamic movement. Standing about 1.4 meters tall and weighing over 35 kg, ARTEMIS features 20 degrees of freedom, including two 5-DoF legs optimized for agile locomotion, two 4-DoF arms capable of minimal gestures, and a 2-DoF head supporting a vision system. ARTEMIS incorporates several innovative design elements: custom-built proprioceptive actuators with liquid cooling maximize torque density, while the robot's kinematic chain and structural components are optimized for fast walking and running. Purpose-designed sensors and electronics enhance feedback reliability under high-impact loads, enabling robust performance.

In 2023, I served as the hardware lead for our RoboCup team, overseeing the manufacture of the second ARTEMIS robot and the maintenance of both ARTEMIS units for daily testing. We built the second ARTEMIS fully in-house in just a few months, covering everything from metal stock and tooling preparation to 5-axis CNC machining and wire EDM. Our team competed in RoboCup 2023 in Bordeaux, France, where we achieved 3rd place in the adult-size humanoid league.

In 2024, as the hardware team lead, I participated in RoboCup in Eindhoven, Netherlands. Our team won first place by scoring 45 goals across six matches and ultimately defeated the longstanding reigning champions in the adult-size humanoid division with a decisive victory of 6-1.

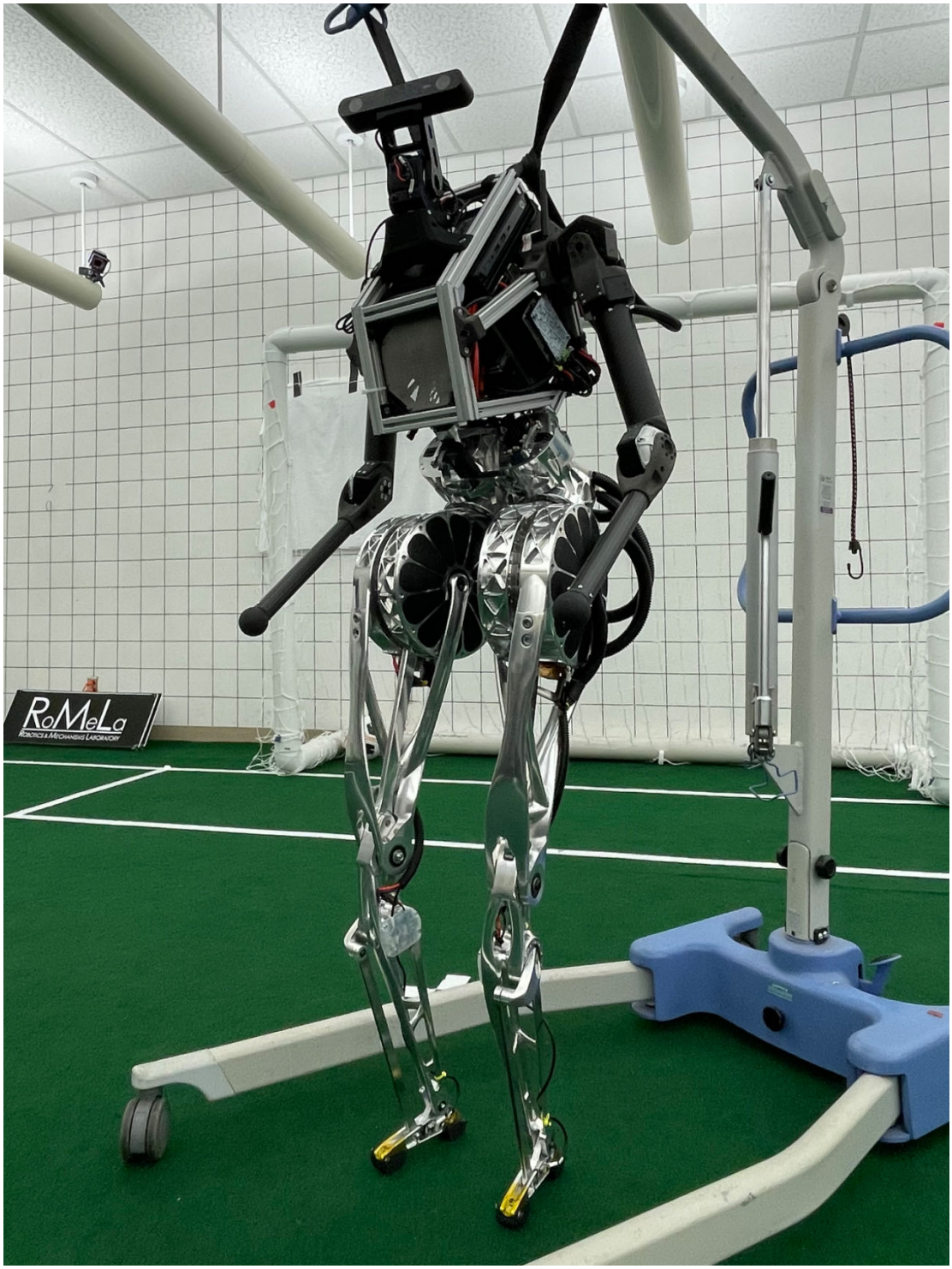

Figure B.1: ARTEMIS 2 prepared for Robocup 2023

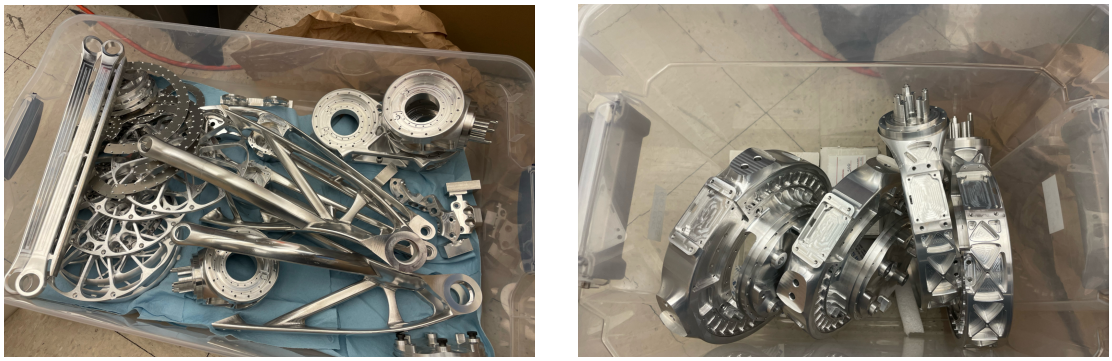

(a) (b)

Figure B.2: (a) ARTEMIS lower body CNC machined parts. (b) Hip pitch and Knee pitch actuator housings.

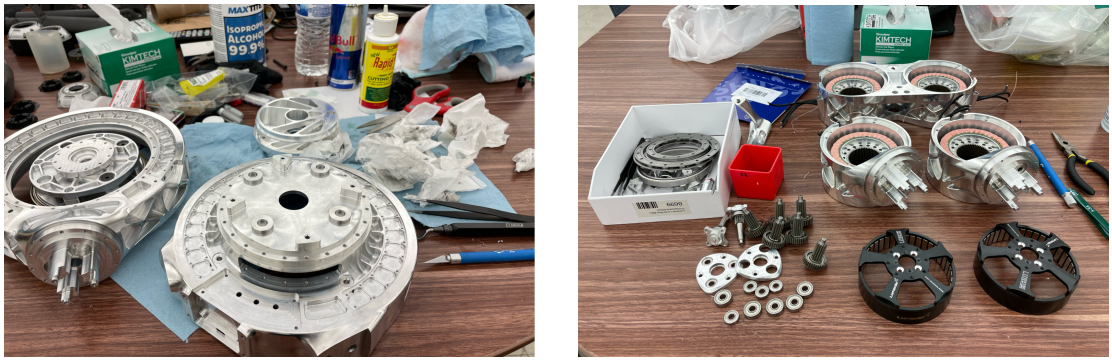

(a) (b)

Figure B.3: (a) Assembling the hip and knee pitch actuators. (b) Prepared hip roll and yaw actuator housings with stators.

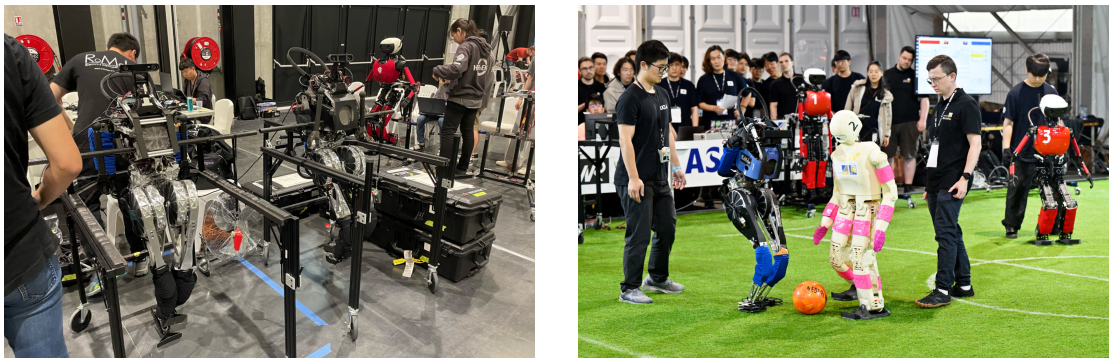

(a) (b)

Figure B.4: (a) ARTEMIS 1&2 ready for competition. (b) Team ARTEMIS play against Team Nimbro.

APPENDIX C

CHARLI & THOR-RD

CHARLI (Cognitive Humanoid Autonomous Robot with Learning Intelligence) is the United States' first full-size autonomous humanoid robot. CHARLI is capable of walking in all directions as well as turning, kicking, and performing gestures and simple upper body manipulation tasks.

THOR-RD (Tactical Hazardous Operations Robot – Rapid Deployment) is a disaster relief humanoid robot that is a modified version of THOR-OP2. It is fully actuated with 31 degrees of freedom controlled by modular position control actuators, IMUs, F/T sensors, and cameras. At 150 cm and 54 kg, THOR-RD is about the same size as a person and has the functionality to match.

In 2021, I contributed to the CHARLI restoration project, fabricating two new arms and ensuring all hardware components were in optimal condition. Collaborating closely with the software team, we successfully restored CHARLI's walking capabilities and additional demonstration functions.

In 2022, I contributed to the revival of the THOR-RD project as part of the preparations for RoboCup 2022. This involved reassembling all hardware components and enhancing the wiring management to ensure hardware reliability during the match. The restored THOR-RD ultimately took on the role of goalkeeper during the soccer matches.

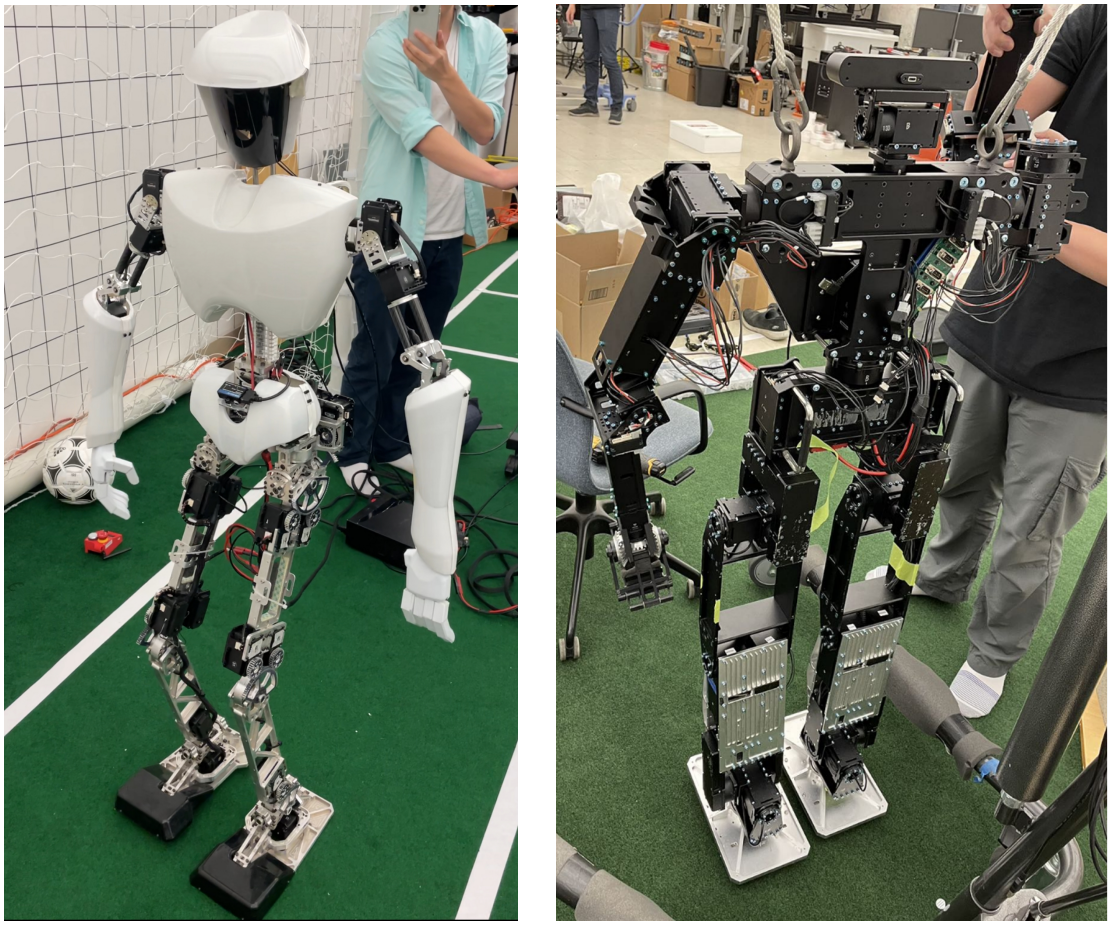

(a) CHARLI (b) THOR-RD

Figure C.1: CHARLI and THOR-RD after restoration

References

[1] S. Seok, A. Wang, D. Otten, and S. Kim, "Actuator design for high force proprioceptive control in fast legged locomotion", in *2012 IEEE/RSJ International Conference on Intelligent Robots and Systems*. IEEE, 2012, pp. 1970–1975.

[2] J. Shen, *Locomotion Analysis and Control of a Miniature Bipedal Robot*, University of California, Los Angeles, 2022.

[3] Y. Liu, J. Shen, J. Zhang, X. Zhang, T. Zhu, and D. Hong, "Design and control of a miniature bipedal robot with proprioceptive actuation for dynamic behaviors", in *2022 International Conference on Robotics and Automation (ICRA)*, 2022, pp. 8547–8553.

[4] J. Shen, J. Zhang, Y. Liu, and D. Hong, "Implementation of a robust dynamic walking controller on a miniature bipedal robot with proprioceptive actuation", in *2022 IEEE-RAS 21st International Conference on Humanoid Robots (Humanoids)*, 2022, pp. 39–46.

[5] J. Zhang, J. Shen, Y. Liu, and D. Hong, "Design of a jumping control framework with heuristic landing for bipedal robots", in *2023 IEEE/RSJ International Conference on Intelligent Robots and Systems (IROS)*, 2023, pp. 8502–8509.

[6] D. Noh, Y. Liu, F. Rafeedi, H. Nam, K. Gillespie, J.-s. Yi, T. Zhu, Q. Xu, and D. Hong, "Minimal degree of freedom dual-arm manipulation platform with coupling body joint for diverse cooking tasks", in *2020 17th International Conference on Ubiquitous Robots (UR)*, 2020, pp. 225–232.

[7] D. Noh, H. Nam, K. Gillespie, Y. Liu, and D. Hong, "Yori: Autonomous cooking system utilizing a modular robotic kitchen and a dual-arm proprioceptive manipulator", *arXiv preprint arXiv:2405.11094*, 2024.

[8] T. Zhu, G. I. Fernandez, C. Togashi, Y. Liu, and D. Hong, "Feasibility study of limms, a multi-agent modular robotic delivery system with various locomotion and manipulation modes", in *2022 19th International Conference on Ubiquitous Robots (UR)*, 2022, pp. 30–37.

[9] T. Zhu, *Design of a highly dynamic humanoid robot*, University of California, Los Angeles, 2023.

[10] T. Kanda, T. Miyashita, T. Osada, Y. Haikawa, and H. Ishiguro, "Analysis of humanoid appearances in human–robot interaction", *IEEE Transactions on Robotics*, vol. 24, no. 3, pp. 725–735, 2008.

[11] T. B. Sheridan, "Human–robot interaction: status and challenges", *Human factors*, vol. 58, no. 4, pp. 525–532, 2016.

[12] K. Yokoyama, H. Handa, T. Isozumi, Y. Fukase, K. Kaneko, F. Kanehiro, Y. Kawai, F. Tomita, and H. Hirukawa, "Cooperative works by a human and a humanoid robot", in *2003 IEEE International Conference on Robotics and Automation (Cat. No.03CH37422)*, 2003, vol. 3, pp. 2985–2991 vol.3.

[13] M. Chignoli, D. Kim, E. Stanger-Jones, and S. Kim, "The mit humanoid robot: Design, motion planning, and control for acrobatic behaviors", in *2020 IEEE-RAS 20th International Conference on Humanoid Robots (Humanoids)*, 2021, pp. 1–8.

[14] M. Hirose and K. Ogawa, "Honda humanoid robots development", *Philosophical Transactions of the Royal Society A: Mathematical, Physical and Engineering Sciences*, vol. 365, no. 1850, pp. 11–19, 2007.

[15] Y. Ogura, H. Aikawa, K. Shimomura, H. Kondo, A. Morishima, H. ok Lim, and A. Takanishi, "Development of a new humanoid robot wabian-2", in *Proceedings 2006 IEEE International Conference on Robotics and Automation, 2006. ICRA 2006.*, 2006, pp. 76–81.

[16] K. Kojima, T. Karasawa, T. Kozuki, E. Kuroiwa, S. Yukizaki, S. Iwaishi, T. Ishikawa, R. Koyama, S. Noda, F. Sugai, S. Nozawa, Y. Kakiuchi, K. Okada, and M. Inaba, "Development of life-sized high-power humanoid robot jaxon for real-world use", in *2015 IEEE-RAS 15th International Conference on Humanoid Robots (Humanoids)*, 2015, pp. 838–843.

[17] J. W. Sensinger and J. H. Lipsey, "Cycloid vs. harmonic drives for use in high ratio, single stage robotic transmissions", in *2012 IEEE International Conference on Robotics and Automation*. IEEE, 2012, pp. 4130–4135.

[18] G. Pratt and M. Williamson, "Series elastic actuators", in *Proceedings 1995 IEEE/RSJ International Conference on Intelligent Robots and Systems. Human Robot Interaction and Cooperative Robots*, 1995, vol. 1, pp. 399–406 vol.1.

[19] https://www.nabtescoprecision.com/en/, ".

[20] https://www.harmonicdrive.net/technology, ".

[21] C. Lee and S. Oh, "Development, analysis, and control of series elastic actuator-driven robot leg", *Frontiers in Neurorobotics*, vol. 13, 05 2019.

[22] T. Zhu, J. Hooks, and D. Hong, "Design, modeling, and analysis of a liquid cooled proprioceptive actuator for legged robots", in *2019 IEEE/ASME International Conference on Advanced Intelligent Mechatronics (AIM)*, 2019, pp. 36–43.

[23] P. M. Wensing et al., "Proprioceptive actuator design in the mit cheetah: Impact mitigation and high-bandwidth physical interaction for dynamic legged robots", *IEEE Transactions on Robotics*, vol. 33, no. 3, pp. 509–522, 2017.

[24] Y. Sakagami et al., "The intelligent asimo: system overview and integration", in *2002 IEEE/RSJ International Conference on Intelligent Robots and Systems (IROS)*, 2002, vol. 3, pp. 2478–2483 vol.3.

[25] A. Kuo, "Choosing your steps carefully", *IEEE Robotics Automation Magazine*, vol. 14, no. 2, pp. 18–29, 2007.

[26] M. Hutter et al., "Anymal - a highly mobile and dynamic quadrupedal robot", in *2016 IEEE/RSJ International Conference on Intelligent Robots and Systems (IROS)*, 2016, pp. 38–44.

[27] X. Xiong and A. D. Ames, "Bipedal hopping: Reduced-order model embedding via optimization-based control", in *2018 IEEE/RSJ International Conference on Intelligent Robots and Systems (IROS)*, 2018, pp. 3821–3828.

[28] B. Katz, J. D. Carlo, and S. Kim, "Mini cheetah: A platform for pushing the limits of dynamic quadruped control", in *2019 International Conference on Robotics and Automation (ICRA)*, 2019, pp. 6295–6301.

[29] Y. Ding et al., "Representation-free model predictive control for dynamic motions in quadrupeds", *IEEE Transactions on Robotics*, vol. 37, no. 4, pp. 1154–1171, 2021.

[30] https://www.bostondynamics.com/atlas, ".

[31] https://agilityrobotics.com/products, ".

[32] I. Ha et al., "Development of open humanoid platform darwin-op", in *SICE Annual Conference 2011*, 2011, pp. 2178–2181.

[33] A. Gasparetto, L. Scalera, et al., "A brief history of industrial robotics in the 20th century", *Advances in Historical Studies*, vol. 8, pp. 24–35, 2019.

[34] J. E. Colgate, W. Wannasuphoprasit, and M. A. Peshkin, "Cobots: Robots for collaboration with human operators", in *ASME international mechanical engineering congress and exposition*. American Society of Mechanical Engineers, 1996, vol. 15281, pp. 433–439.

[35] https://www.universal robots.com/products/, ".

[36] D. V. Gealy, S. McKinley, B. Yi, P. Wu, P. R. Downey, G. Balke, A. Zhao, M. Guo, R. Thomasson, A. Sinclair, et al., "Quasi-direct drive for low-cost compliant robotic manipulation", in *2019 International Conference on Robotics and Automation (ICRA)*. IEEE, 2019, pp. 437–443.

[37] A. Tilley and H. Associates, *The Measure of Man and Woman: Human Factors in Design*, Interior design.industrial design. Wiley, 2001.

[38] https://westwoodrobotics.io/bearseries/koala-bear/, ".

[39] https://www.robotis.us/dynamixel-xl430-w250-t/, ".

[40] Y.-J. Kim, "Anthropomorphic low-inertia high-stiffness manipulator for high-speed safe interaction", *IEEE Transactions on robotics*, vol. 33, no. 6, pp. 1358–1374, 2017.

[41] K. Kojima et al., "A robot design method for weight saving aimed at dynamic motions: Design of humanoid jaxon3-p and realization of jump motions", in *2019 IEEE-RAS 19th International Conference on Humanoid Robots (Humanoids)*, 2019, pp. 586–593.

[42] Z. Xie, G. Berseth, P. Clary, J. Hurst, and M. van de Panne, "Feedback control for cassie with deep reinforcement learning", in *2018 IEEE/RSJ International Conference on Intelligent Robots and Systems (IROS)*, 2018, pp. 1241–1246.

[43] A. Roig, S. K. Kothakota, N. Miguel, P. Fernbach, E. M. Hoffman, and L. Marchionni, "On the hardware design and control architecture of the humanoid robot kangaroo", in *6th workshop on legged robots during the international conference on robotics and automation (ICRA 2022)*, 2022.

[44] S. G. McGill, S.-J. Yi, H. Yi, M. S. Ahn, S. Cho, K. Liu, D. Sun, B. Lee, H. Jeong, J. Huh, et al., "Team thor's entry in the darpa robotics challenge finals 2015", *Journal of Field Robotics*, vol. 34, no. 4, pp. 775–801, 2017.

[45] X. Zhang, *Application of Proprioception Quasi-Direct Drive Actuators on Dynamic Robotic Systems*, University of California, Los Angeles, 2019.

[46] J. K. Salisbury et al., "Compact cable transmission with cable differential", U. S. Patent 5 046 375, 1991-09-10.

[47] F. Nori et al., "icub whole-body control through force regulation on rigid non-coplanar contacts", *Frontiers in Robotics and AI*, vol. 2, pp. 6, 2015.

[48] J. Heinzmann and A. Zelinsky, "The safe control of human-friendly robots", in *1999 IEEE/RSJ International Conference on Intelligent Robots and Systems (IROS)*, 1999, pp. 1020–1025.

[49] B. G. Katz, *A low cost modular actuator for dynamic robots*, PhD thesis, Massachusetts Institute of Technology, 2018.

[50] J. Zhu, W. Zhang, and L. Xia, "Topology optimization in aircraft and aerospace structures design", *Archives of Computational Methods in Engineering*, 04 2015.

[51] O. Sigmund, *Design of Material Structures Using Topology Optimization*, PhD thesis, Technical University of Denmark, 01 1994.

[52] L. MENG, W. Zhang, D. Quan, G. Shi, L. Tang, Y. Hou, P. Breitkopf, J. Zhu, and T. Gao, "From topology optimization design to additive manufacturing: Today's success and tomorrow's roadmap", *Archives of Computational Methods in Engineering*, vol. 27, 03 2019.

[53] B. Stellato, G. Banjac, P. Goulart, A. Bemporad, and S. Boyd, "Osqp: An operator splitting solver for quadratic programs", 09 2018, pp. 339–339.

[54] M. K. Shepherd and E. J. Rouse, "Design and validation of a torque-controllable knee exoskeleton for sit-to-stand assistance", *IEEE/ASME Transactions on Mechatronics*, vol. 22, no. 4, pp. 1695–1704, 2017.

[55] J. Urata, Y. Nakanishi, K. Okada, and M. Inaba, "Design of high torque and high speed leg module for high power humanoid", in *2010 IEEE/RSJ International Conference on Intelligent Robots and Systems*. IEEE, 2010, pp. 4497–4502.

[56] J. Li, C. Teeple, R. J. Wood, and D. J. Cappelleri, "Modular end-effector system for autonomous robotic maintenance & repair", in *2022 International Conference on Robotics and Automation (ICRA)*. IEEE, 2022, pp. 4510–4516.

[57] X. Lin, G. I. Fernandez, Y. Liu, T. Zhu, Y. Shirai, and D. Hong, "Multi-modal multi-agent optimization for limms, a modular robotics approach to delivery automation", in *2022 IEEE/RSJ International Conference on Intelligent Robots and Systems (IROS)*, 2022, pp. 12674–12681.